



TECHNISCHE
UNIVERSITÄT
WIEN
Vienna University of Technology

DIPLOMARBEIT

Novel Intercalation Materials for Non-Aqueous Metal-ion Batteries

**Ausgeführt am Institut für
Chemische Technologien und Analytik
der Technischen Universität Wien**

**unter der Anleitung von
Ao.Univ.Prof. Dipl.-Ing. Dr.techn. Günter Fafilek
und Dr. L. J. Hardwick**

**durch
Sabine Gruber, BSc
Veitingergasse 49, 1130 Wien**



TECHNISCHE
UNIVERSITÄT
WIEN
Vienna University of Technology

STEPHENSON INSTITUTE
FOR RENEWABLE ENERGY



UNIVERSITY OF
LIVERPOOL



THE UNIVERSITY
of LIVERPOOL

**The Department of Chemistry and
The Stephenson Institute for Renewable Energy**

**Novel Intercalation Materials for Non-Aqueous
Metal-ion Batteries**

2012 / 2013

Sabine Gruber, BSc

Student id no. 0726358

Supervisor: Dr. L. J. Hardwick

Co-Assessor: Ao.Univ.Prof. Dipl.-Ing. Dr.techn. Günter Faflek

Acknowledgements

The author would like to offer his gratitude to Dr. L. J. Hardwick for allowing her to undertake this great opportunity of writing her diploma thesis at the University of Liverpool and the Stephenson Institute for Renewable Energy in the field of battery research. The author would like to thank Dr. L. J. Hardwick for his invaluable support, guidance and assistance throughout the course of this project.

Furthermore the author would like to thank Iain Aldous, Stephen Hughes, Arturas Adomkevicius and Nick Drewett for their great support and the really great time she had. Last but not least the author would also like to thank Ao.Univ.Prof. Dipl.-Ing. Dr.techn. Günter Faflek for his kindness and support enabling her to undertake her diploma thesis at a foreign university.

Abstract

Lithium ion batteries are the widely used battery systems in the field of portable devices like mobile phones, laptops, electric vehicles, camcorders and a lot of other every day commodities. The amount of electronic portable devices is growing and therefore also the demand for lithium ion batteries is increasing. Although there exist enough lithium sources on the earth researchers are anxious to investigate new systems to provide batteries with larger capacities, higher energies and power densities to be able to keep up with the high power demand of a lot of products, which is dependent on both the construction and design as well as the chemistry within a battery system.

Recent papers suggest a novel battery system including aluminium instead of lithium as active element undergoing the electrochemical reactions. Benefits like a possible transfer of three electrons per ion and the lower reactivity of aluminium compared to lithium lead to the prospect of cheaper and safer batteries including a higher energy density.

In this work experiments were undertaken to investigate two new kinds of aluminium batteries:

- A non-aqueous aluminium battery consisted of self-made V_2O_5 nanowires, produced via a hydrothermal method, as working electrode and the ionic liquid electrolyte 1-ethyl-3-methylimidazolium chloride ([EMIm]Cl) including $AlCl_3$
- An aqueous aluminium battery with a TiO_2 working electrode and an electrolyte made of a solution of 1 M $AlCl_3$ in water

Furthermore were undertaken *in situ* Raman measurement with a special designed two electrodes *in situ* Raman cell providing a good signal to noise ratio to investigate the intercalation of aluminium as well as lithium into electrodes made of Graphite, TiO_2 , $Li_4Ti_5O_{12}$ and the commercial V_2O_5 powder as well as the synthesised V_2O_5 nanowires.

Table of Contents

1	Introduction.....	1
2	Theory	3
2.1	Batteries.....	3
2.1.1	Thermodynamics.....	6
2.1.2	Kinetics	8
2.2	Li-ion Batteries.....	11
2.2.1	History.....	13
2.2.2	Electrode Reaction Mechanisms.....	14
2.2.3	Electrode-Electrolyte Interplay.....	18
2.2.4	Electrolytes	21
2.2.5	Negative Electrode Materials.....	26
2.2.6	Positive Electrode Materials	34
2.2.7	Current Collectors.....	41
2.3	Aluminium Ion Battery	42
2.4	Batteries Measuring Methods.....	43
2.4.1	Electrochemical Methods.....	43
2.4.2	Other Techniques	46
3	Experimental	53
3.1	Battery Cell Types.....	53
3.1.1	Coin Cell	53
3.1.2	Swagelok Cell	54
3.1.3	<i>In situ</i> Raman Cell	55
3.2	Synthesis of V ₂ O ₅ Nanowires	57

3.3	Preparation of Electrodes	59
3.3.1	Electrodes for Coin Cells and Swagelok Cells	59
3.3.2	Electrodes for <i>in situ</i> Raman Cell	60
3.4	Preparation of Electrolytes	61
3.4.1	EC/DMC with LiClO ₄	61
3.4.2	EC/DMC with LiPF ₆	61
3.4.3	([EMIm]Cl) with AlCl ₃	61
3.4.4	Aqueous AlCl ₃	61
3.5	Equipment properties	62
3.5.1	Raman Instrumentation.....	62
3.5.2	Potentiostat Instrumentation	62
3.5.3	Solid State NMR Spectroscopy Instrumentation	62
3.5.4	Glove Box Instrumentation.....	63
4	Results and Discussion	64
4.1	V ₂ O ₅ Nanowire Synthesis and Characterisation	64
4.2	Aluminium Ion Battery	68
4.2.1	Ionic Liquid Electrolyte	68
4.2.2	Aqueous AlCl ₃ Electrolyte.....	81
4.3	Lithium Ion Battery	84
4.3.1	Electrochemical Characterisation	84
4.3.2	Raman Measurements.....	99
5	Conclusions.....	144
6	Further Work.....	145
7	References.....	146

1 Introduction

Today a world without batteries is unimaginable. They act as energy stores that power millions of cell phones, notebooks, camcorders and cameras that are in use. Intensive research and development of battery technology is leading them to find further applications within power tools, electric vehicles and emergency power backup. The amount of electricity generated worldwide has more than trebled since 1971, see Figure 1. [1, 2] As most electricity is generated from the burning of fossil fuels this is responsible for the environmental pollution by the emission of carbon dioxide (CO₂), which has increased enormously over the last few decades, see Figure 3. Increasing concentrations of atmospheric CO₂ is linked to rising global temperatures and with that the risk of extreme weather events that are causing natural catastrophes all over the world. [3-5] Fossil fuels are non-renewable and therefore in the long-term will be in short supply, which will cause price instability. [3] However, the increasing exploitation of tar sands to extract shale gas via induced hydraulic fracturing, commonly known as fracking, is likely to lead North America to be energy self-sufficient within a decade, which is likely to slow the rate of adoption of green technologies. [6]

As a result of these problems governments are trying to reduce their reliance on fossil fuels and to involve more renewable energy productions such as wind, waves and solar power. The consumption of electricity is not stable and so these energy resources will gain from the combination with energy storage technologies such as batteries by storage the excess energy in off peak times and to release it in on peak periods to be able to provide enough energy for the whole time. [5, 7]

Electrochemical energy can be gained on the one side through energy storage devices, like batteries and supercapacitors and on the other side through energy conversion devices like fuel cells. In batteries and fuel cells the power gets produced by the transformation of chemical energy into electrical energy with the aid of a redox reaction at the interfaces of electrodes and electrolyte where the ions get separated from the electrons. Batteries are closed systems, where the energy storage and conversion take place in the same compartment. The electrodes are responsible for the charge transfer and

are additionally directly part of the redox reaction; they are called “active masses”. Compared to batteries in fuel cells the active masses, which undergo the redox reaction, have to be delivered to the electrodes where the energy conversion occurs. In fuel cells the electrodes are just charge transfer media. Therefore fuel cells are called open systems, where the storage of energy is in another compartment than the conversion. Electrochemical capacitors operate without any redox reaction. The energy is stored by orientation of ions from the electrolyte between the electrodes via a so called double layer. Forming and releasing of this double layer leads to a parallel movement of electron in an external wire. [8]

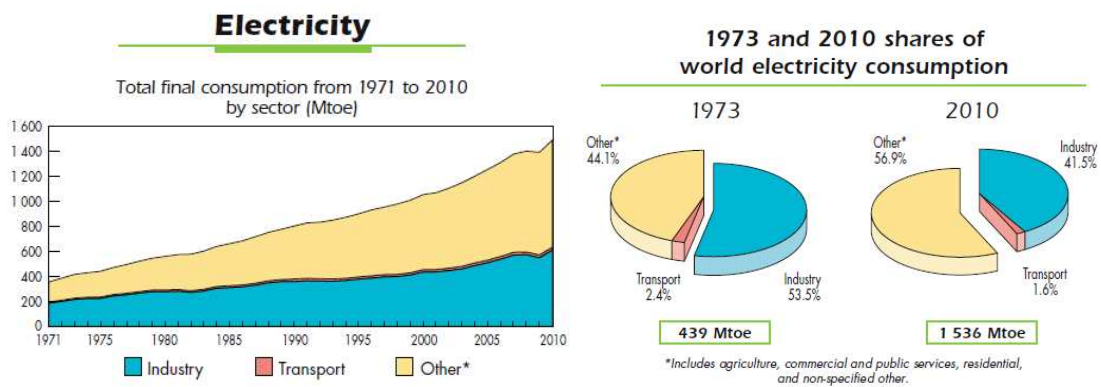


Figure 1: World total electricity consumption, 1971 to 2010 in Mtoe (million tonnes of oil equivalent) [2]

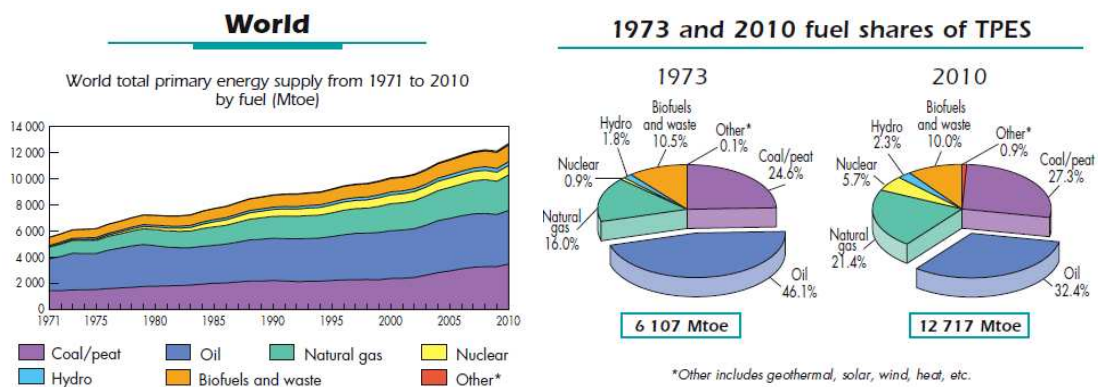


Figure 2: World total primary energy supply, 1971 to 2010 in Mtoe (million tonnes of oil equivalent) [2]

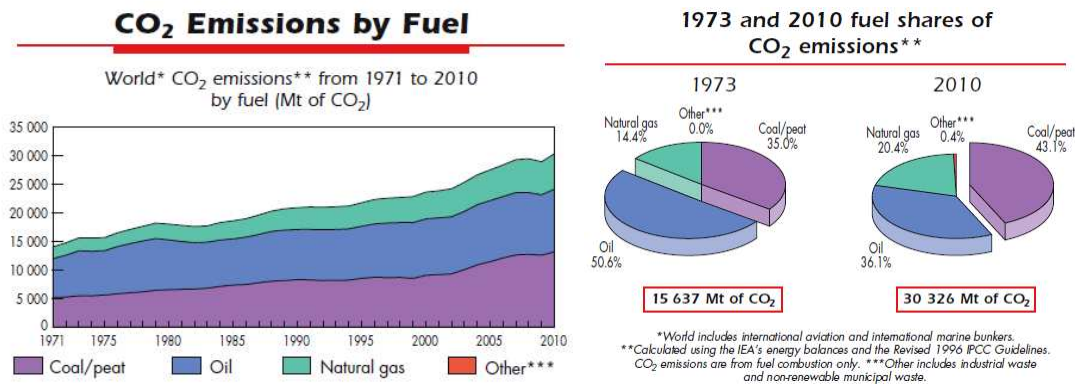


Figure 3: World total CO₂ emission, 1971 to 2010 in Mt (million tonnes) [2]

2 Theory

2.1 Batteries

A battery consists of several electrochemical cells, which are connected in series and/or in parallel to be capable of producing the required voltage and capacity. In each cell there are two electrodes, which are separated through an ionic conducting electrolyte and connected to each other via an external circuit. [9] The electrodes are called anode and cathode according to the chemical redox reaction which occurs during charging and discharging. The terms cathode and anode cannot be properly defined in a rechargeable cell since the anode is identified as the electrode which gives electrons to the external circuit, and the cathode is the electrode that receives electrons from the external circuit. Therefore depending on whether the cell is being charged or discharged the two terms are mixed. To avoid confusion the electrodes can be simply categorised as either positive or negative because the term refers to their respective electrode potentials. One of them has a positive electrochemical potential like lithium cobalt oxide, manganese dioxide or lead oxide and one has a negative electrochemical potential like lithium, zinc or lead. At the anode proceeds the oxidative chemical reaction hence electrons run into the external circuit. At the cathode electrons are consumed from the external circuit by a reductive chemical reaction. [8] The electrolyte contains a dissociated salt which makes the ion transfer from one electrode to the other possible. [9] In practice a separator, a

porous electrically insulating material containing the electrolyte, is used to prevent a direct contact between the two electrodes and so to avoid a short circuit. In a short circuit the whole energy is released within a few seconds by producing heat inside the battery. This can cause disastrous consequences like thermal runaway and potential explosion of the battery. The battery has to be well-engineered to minimize the risk of these events. [1, 8, 10]

A distinction is drawn between primary and secondary batteries. Primary batteries consist of one or more electrochemical cells containing a certain amount of electrochemical energy, which could be used until exhaustion. After use the primary battery is disposed of as it cannot be recharged. Unlike the primary battery a secondary battery also known as accumulator can be recharged after its discharge to store new energy, which could be used once again. [10]

The lithium-ion battery is the most familiar example of a secondary battery because it has the currently highest energy storage. [9, 11]

The performance of a battery is distinguished by the specific power (W/kg) and the power density (W/dm³), which describes the available power output of a system per mass or volume. Therefore a high specific power and power density is desirable to be able to keep up with the high power demand of a lot of products, which is dependent on both the construction/design as well as the chemistry. The specific energy (Wh/kg) is also known as gravimetric energy density and the energy density (Wh/dm³) is also called volumetric energy density. The theoretical specific energy is calculated from the cell voltage, the number of transferred electrons and the masses of the active materials in the electrode and describes the amount of electrical energy per unit of volume. Therefore the masses of all other compounds of a battery, like current collectors, separator and electrolyte, are neglected. This is among other things like electro kinetic a reason why the practical specific energy is four or five times lower than the theoretical one. [12]

The total available charge of a battery is described by the charge capacity Q [13], which can be calculated by Faraday's equation, see Equation 5. The theoretical specific charge capacity (Ah/kg) is related to the mass of reactants. [14]

The lifetime of a battery is determined as the total number of charge/discharge cycles before a significant decrease of the energy and power values occur. [1]

The charge/discharge range also known as *C-range* ($C/\Delta t$) determines the time range in which the battery is fully charged or discharged. C stands for the charge capacity in Ah . For example $C/5$ means that the battery is completely charged or discharged within 5 hours. [15]

In Figure 4 are some battery systems compared by their specific energy and energy density. As shown Li-ion batteries have the highest specific energy and energy density and therefore they are one of the most investigated battery systems in recent days. [9]

The present research of rechargeable batteries focus on new electrode materials which enable batteries to:

- larger capacity, higher energy and power density
- higher reactivity, reversibility and structural stability during charging/discharging cycles
- faster ionic diffusion and electronic transfer at high discharge/charge rate
- lower cost, higher safety and more environmental friendly [11]

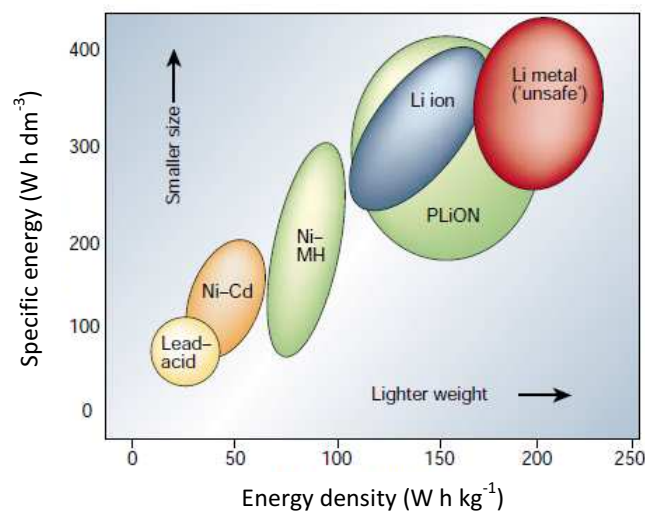


Figure 4: Comparison of the different battery technologies of specific energy (Wh/dm^3) and energy density (Wh/kg). [9]

2.1.1 Thermodynamics

The whole electrochemical energy, which is stored in an energy storage system, is the Gibbs free energy ΔG also known as free energy of reaction. [1] For a spontaneous reaction the Gibbs free energy is always negative. Equation 1 shows the basic thermodynamic equation for a reversible electrochemical transformation at standard state conditions, emblemized by the degree symbol. The enthalpy of reaction ΔH determines the released energy J during a reaction. Entropy ΔS describes the rate of organisation or disorganisation in a material. [8]

Equation 1: Gibbs-Helmholtz equation [8] [16]

$$\Delta G^\circ = \Delta H^\circ - T\Delta S^\circ$$

ΔG° ... Gibbs free energy [kJ/mol], ΔH° ... Enthalpy [kJ/mol], T ... Temperature [K], ΔS° ... Entropy [kJ/(mol·K)]

To describe electrical work the Gibbs free energy can also be written as seen in Equation 2. The number of transferred electrons n is related to one mole of reactants. F is the Faraday constant and E° is the voltage of the cell, which depends on the specific chemical reaction that occurs. nF describes therefore the amount of produced electricity and relates to the total available material for the reaction. [8]

Equation 2: Gibbs free energy to describe electrical work [6, 8]

$$\Delta G^\circ = -n \cdot F \cdot E^\circ$$

ΔG° ... Gibbs free energy [kJ/mol], n ... number of transferred electrons, F ... Faraday constant [A·s/mol], E° ... Voltage of the cell [V]

The Van't Hoff isotherm equation depicts the free energy of a chemical reaction between two masses, see Equation 3. A_P is the activity product of the products and A_R is the activity product of the reactants. R is the usual gas constant and T the absolute temperature. [8]

Equation 3: Van't Hoff Isotherm [6, 8]

$$\Delta G = \Delta G^{\circ} + RT \ln \left(\frac{A_P}{A_R} \right)$$

ΔG ... Gibbs free energy [kJ/mol], ΔG° ... Gibbs free energy at standard state [kJ/mol], R ... gas constant [kJ/(mol·K)], T ... absolute temperature [K], A_P ... activity product of the products, A_R ... activity product of the reactants

The combination of Equation 2 and Equation 3 relates to the Nernst equation for electrochemical reactions, see Equation 4. [8]

Equation 4: Nernst Equation [6, 8]

$$E = E^{\circ} + \left(\frac{RT}{nF} \right) \ln \left(\frac{A_P}{A_R} \right)$$

E ... Voltage of the cell [V], E° ... Voltage of the cell at standard state [V], R ... gas constant [J/(mol·K)], T ... absolute temperature [K], n ... number of transferred electrons, F ... Faraday constant [A·s/mol], A_P ... activity product of the products, A_R ... activity product of the reactants

The correlation between the amount of reaction products and the current flow is also known as the Faraday's law, see Equation 5, which relates just to the mass balance. In this equation g is the mass and MW the molecular weight of the transformed material, I the current flow, t is the time, n is the number of transferred electrons within the reaction and F is the Faraday constant. [8, 17]

Equation 5: Faraday's law [6, 8]

$$g = \frac{It(MW)}{nF}$$

g ... mass [g], I ... current flow [A], t ... time [s], MW ... molecular weight [g/mol], n ... transferred electrons, F ... Faraday constant [A·s/mol]

If the Equation 1 and Equation 2 are correlated and thermodynamically reversibility is provided Equation 6 will be generated. The thermodynamic quantities of a material can be calculated by the measuring of the dependence between the cell voltage and the temperature. The cell will heat on charge and cool on discharge if $\delta E / \delta T$ is positive and if it is negative it will be the other way round. The total heat release of a battery cell system during charge and discharge including the reversible thermodynamic heat release and the

irreversible joule heat is described in Equation 7. q is the heat, which is given off the system, E_{OCV} is the open circuit voltage of the cell and E_T is the practical cell terminal voltage. [8]

Equation 6: Cell voltage as a function of temperature [6, 8]

$$\Delta G = -nFE = \Delta H - T\Delta S = \Delta H - nFT \left(\frac{\delta E}{\delta T} \right)$$

ΔG ... Gibbs free energy [kJ/mol], n ... number of transferred electrons, F ... Faraday constant [A·s/mol], E ... Voltage of the cell [V],
 ΔH ... Enthalpy [kJ/mol], T ... Temperature [K], ΔS ... Entropy [kJ/mol·K]

Equation 7: Total heat release during charge discharge processes [8]

$$q = T\Delta S + I(E_{OCV} - E_T)$$

q ... heat given off by the system [W], T ... temperature [K], ΔS ... Entropy [J/K], I ... current flow [A], E_{OCV} ... open circuit voltage [V], E_T ... practical cell terminal voltage [V]

For low temperature batteries the heat release is not a big problem, but for high temperature batteries suitable heat dissipations must be considered to inhibit thermal runaways or other catastrophic situations. [8]

2.1.2 Kinetics

Due to kinetic limitations the voltage decreases during operation, which is also known as electrode polarisation or overvoltage. In general the kinetics of electrochemical reactions and of bulk chemical reactions are quite similar. The two important differences are that the potential drop influences the electrochemical double layer at the electrode surface, which directly affects the activated redox couple and that the reaction is not a three dimensional reaction, but a two dimensional one. There are three different kinds of polarization effects: the activation polarization, the ohmic polarisation and the concentration polarisation. The activation polarisation is caused by the electrochemical redox reaction at the interfaces between electrodes and electrolyte. Contact problems between different cell elements and the resistance within each cell element are responsible for the ohmic polarisation. [8] The concentration polarization occurs because of mass transport limitations in the electrolyte as well as in the electrodes during an operation. [1] The polarisation η can be described as written in Equation 8. [8]

Equation 8: Polarization [8]

$$\eta = E_{OCV} - E_T$$

η ... polarization [V], E_{OCV} ... open circuit voltage [V], E_T ...terminal cell voltage during current flows [V]

The activation polarisation can be characterised by the absolute reaction rate theory or the transition state theory in which the rate limiting step is the dissociation of an activated complex, which is part of the redox reaction at the electrode surfaces. The rate or the current flow of such a limited redox reaction of a battery system is specified by the Butler-Volmer equation, see Equation 9. In this equation the current densities i and i_0 are the current flow based on the electrode surface area. The exchange current density i_0 is a function of the reaction rate constant k_0 for the electrode reaction, the Faraday constant and the activity product of the reactants A , see Equation 10. The transfer coefficient α can be delineated as the fraction of the change of the overpotential, which manipulates the rate constant. A high exchange current density i_0 is favored for battery systems, because therefore the reaction is more reversible and there occur lower polarization effects. [8]

Equation 9: Butler-Volmer equation [6, 8]

$$i = i_0 \cdot e^{\left(\frac{\alpha F \eta}{RT}\right)} - e^{\left(\frac{(1-\alpha) F \eta}{RT}\right)}$$

η ... polarization [V], i ... current density [A/m²], i_0 ... exchange current density [A/m²], α ... transfer coefficient, F ... Faraday constant [C/mol], R ... gas constant [J/(K·mol)], T ...temperature [K]

Equation 10: Exchange current density [6, 8]

$$i_0 = k_0 F A$$

i_0 ... exchange current density [A/m²], k_0 ... reaction rate constant, F ... Faraday constant [C/mol], A ... activity product of the reactants

The activation polarization appears within the first milliseconds (10^{-2} - 10^{-4} s) and obeys the Tafel equation, see Equation 11, which could be gained for high polarisation by transformation of the Butler Volmer equation. [8]

Equation 11: Tafel equation [8]

$$\eta = a - b \log \left(\frac{i}{i_0} \right)$$

η ... polarization [V], a,b... constants, i... current density [A/m²], i_0 ... exchange current density [A/m²]

The ohmic polarisation is caused by the resistance of each cell element and their interfaces. It occurs instantaneously ($\leq 10^{-6}$ s) when the current flows and can be described by the linear Ohm's Law, see

Equation 12. [8]

Equation 12: Ohm's Law [8]

$$\eta = IR$$

η ... polarization [V], I... current [A], R... current resistance [Ω]

Due to limitations in the mass transport of active material to and from the electrode surface within the electrolyte as well as the transport of intercalated species inside of the electrodes the concentration polarisation causes a drop of the voltage. The diffusion process is very slow and therefore it appears after a few milliseconds ($\geq 10^{-2}$ s). In case of limited diffusion process the concentration polarization follows Equation 13. [8]

Equation 13: Concentration polarization with limited diffusion [8]

$$\eta = \left(\frac{RT}{n} \right) \ln \left(\frac{C}{C_0} \right)$$

η ... polarization [V], R... gas constant [J/(mol·K)], T... temperature [K], n... amount of substance [mol], C... concentration at the electrode surface, C_0 ... concentration in the bulk of the solution

In Figure 5 is shown a typical discharge curve of a battery with all three effects of the different kinds of polarization. [8]

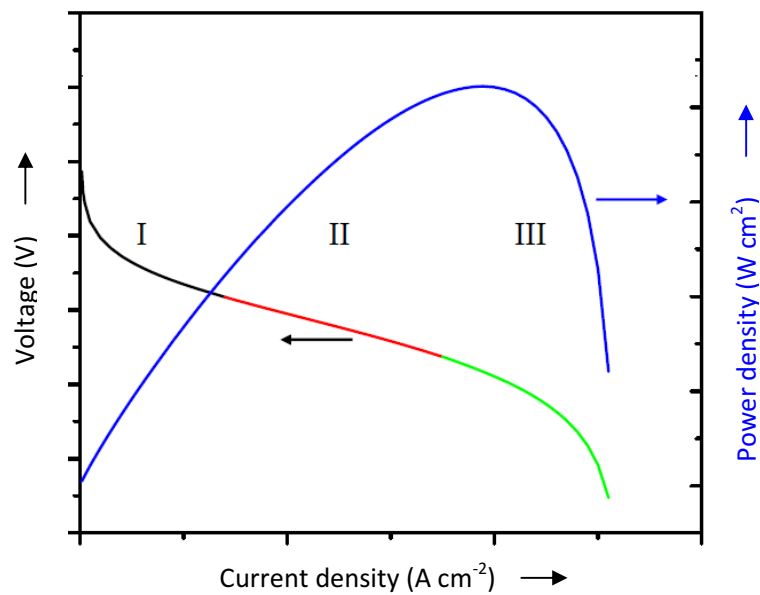


Figure 5: Typical discharge curve of a battery, showing the influences of the three polarization effects, I: activation polarisation, II: ohmic polarisation, III: concentration polarisation [18]

2.2 Li-ion Batteries

Li-ion batteries are comparing to all other existent secondary battery systems the most investigated. [9] They are light, compact, work with a voltage of about 4 V and have a high energy density of about 150 Wh/kg. Because of their great performance lithium ion batteries are established in many applications like mobile phones, laptops, electric vehicles, camcorders and a lot of other everyday commodities and the amount of electronic portable devices including lithium ion batteries is growing, see Figure 6. [3] [19] As one can see in Figure 7 lithium ion batteries are by far the most produced secondary batteries in the year 2011 in Japan next to nickel metal-hydride batteries, alkaline storage batteries and lead-acid batteries.

Furthermore lithium batteries are, because of their high energy density and their cycle life, promising candidates for the electric vehicle market. Most likely they will take part of the deliverance of the addiction to fossil fuels. [21] There is a big lithium carbonate reservoir in South America, a new discovered one in Afghanistan and furthermore lithium can also be obtained from sea water, though the cost of this will be prohibitive. All together there are about several hundred thousand of megatons of lithium metal available

and hence there will be enough lithium in the future even if a total change from fuel burning vehicles to hybrids or electric cars occurs. [19]

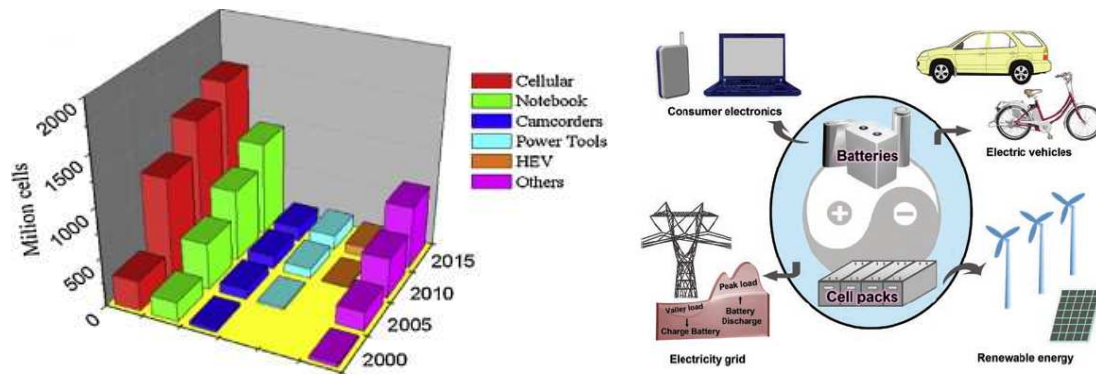


Figure 6: Left - Evolution of the lithium ion sale market with portable electric devices and full hybrid electric vehicles (HEV) [3] Right – Applications for rechargeable batteries [11]

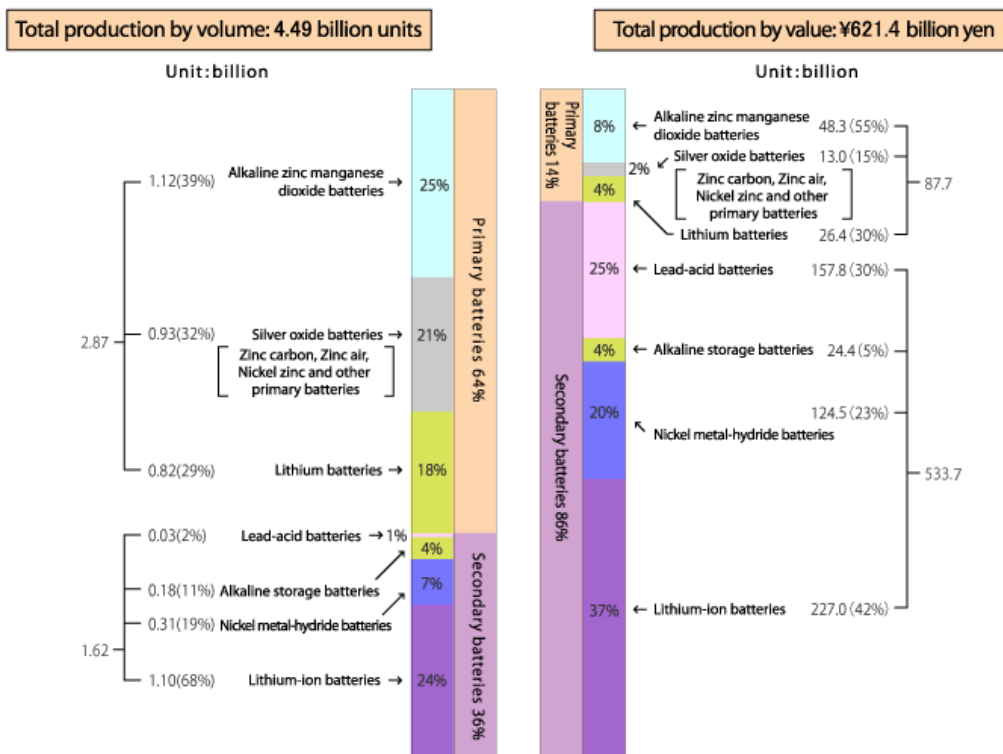


Figure 7: Total battery production statistics of Japan in 2011

2.2.1 History

Lithium is the most electronegative (-3.04 V versus standard hydrogen electrode) and also the lightest metal (molecular weight: $M = 6.95 \frac{g}{mol}$, specific gravity: $\rho = 0.53 \frac{g}{cm^3}$) on earth. Therefore the use of lithium metal with an electrochemical cell is highly attractive due to the potentially high electrochemical storage [9, 13].

The first primary non rechargeable battery including lithium as the negative electrode was designed in the 1970s, which were used in applications like watches, calculators or implantable medical devices due to its high capacity and variable discharge rate. After some time inorganic materials were found, like TiS_2 in 1972, which could be used as positive electrodes. These new intercalation materials enabled the lithium battery to recharge, but they were soon identified to be too dangerous, because of hazardous explosions due to dendritic growth of lithium within each cycle. [9] Furthermore undesirable side reaction of the lithium metal with the electrolyte appeared. [13]. Later on different oxides as electrode materials were found like Li_xMO_2 ($M = Co, Ni, Mn$) which were more oxidising than disulphides due to their bigger ionic character between the M-O bond compared to the M-S bond. These new materials are even now used in modern batteries. To be able to solve the safety problem due to explosions different modifications of the negative electrode as well as the electrolyte were investigated. [9]

In the early 1990s the Li-ion battery or also known as rocking chair battery was invented. The idea was to add a second intercalation electrode material as negative electrode to avoid the dendritic build-up of lithium and therefore to avoid the hazardous reactions. [22] In 1991 Sony Corporation commercialised the first rocking chair Li-ion battery with a carbonaceous negative electrode, which facilitates a highly reversible and low-voltage Li-intercalation process. [23] This rocking chair battery operates with a voltage of 3.6 V and has a gravimetric energy density of about 120-150 Wh/kg. [9] Replacing the metal lithium electrode by an lithium insertion material improved the lifetime as well as the safety of the battery, but unfortunately these improvements accompanied with a loss of the cell voltage, the specific charge and the rate capability. [13]

Another improvement of the lithium battery was the investigation of the Li solid polymer electrolyte (Li-SPE). [24, 25] There the liquid electrolyte was replaced by a solid polymer, but unfortunately these batteries were limited to large systems with

temperatures about 70 °C. [15, 26] The hybrid polymer electrolyte battery (Li-HPE) which used a three part electrolyte, including a polymer matrix swollen in a liquid solvent and a salt, also did not get commercialized because of residual dendritic growing. The first useable HPE battery was called plastic Li ion (PLiON) battery and was commercialized in 1999. This type of battery contains a gel-coated, micro porous polyolefin separator, which connects the two also gel loaded electrodes. The advantage of this battery is that it enables a very thin and flexible cell configuration unlike the usual coin-, cylindrical- or prismatic- type, see Figure 8. [27] This could be beneficial to the continuing trend of miniaturization of electronic devices. [9]

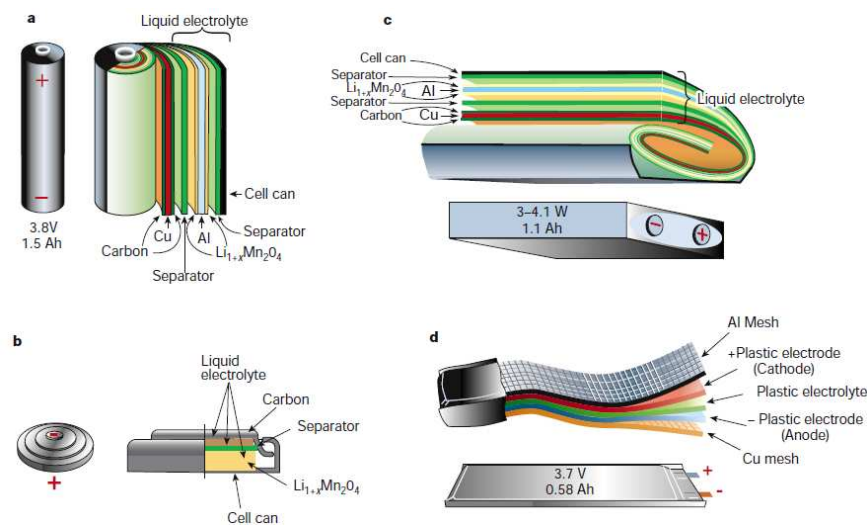


Figure 8: Different cell configuration of Li-ion battery; a) cylindrical b) coin c) prismatic d) thin and flat (PLiON) [9]

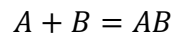
2.2.2 Electrode Reaction Mechanisms

There exist two major electrode reaction mechanisms namely the reconstitution reactions, where different phase transformations occur and therefore the microstructure of the material changes, and the insertion reactions, where no changes in the identity, the crystal structure and the amount of phases of the microstructure of the electrode material take place. [28]

2.2.2.1 Reconstitution Reactions

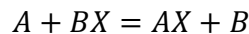
Two main types of reconstitution reactions are formation reactions and displacement reactions. In a formation reaction, see Equation 14, two starting components (A and B) react by forming a new phase AB , obviously changes the microstructure. [28]

Equation 14: Formation Reaction [28]



In a displacement reaction, see Equation 15, species A replaces species B in a binary system BX which leads to the more stable binary system AX . Species B forms thereby a new phase. [28]

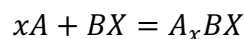
Equation 15: Displacement Reaction [28]



2.2.2.2 Insertion Reactions

Insertion reactions can be described by Equation 16, where an amount x of an atomic guest species A reacts with a host material BX to the chemical material A_xBX via an insertion reaction. During this reaction the crystal structure of the host material does not change, because the guest species inserts into previously unoccupied interstitial sites. Nevertheless the insertion causes changes in the volume of the host material which leads to mechanical stress and energy, which affects the equilibrium of amount of inserted guest species and hence the reversibility of a battery reaction. [28]

Equation 16: Insertion Reaction [28]



If the guest species intercalate in between the layers of a layered crystal structure of the host material, the reaction is also called intercalation reaction. [28]

To get a high specific energy (W/kg) and a high energy density (Wh/dm³) within a battery system there must be two important things considered. First of all there must be a high specific charge (Ah/kg) and a high charge density (Ah/dm³) to gain a lot of available charge carriers per mass or volume. Furthermore to receive a high cell voltage there should be a high standard redox potential for the positive electrode and a low standard redox potential for the negative electrode concerning to the occurring redox reaction. Another important thing is that there must be a high reversibility of the electrode reactions to get a high number of charge/discharge cycles without any specific charge losses and therefore to reach a long lifetime of the battery. If the cycling efficiency is 99% in each cycle the remaining specific charge density would be only about 37% after 100 cycles and only 1% after 500 cycles. This example shows that a really high cycling efficiency is essential. Insertion materials are the best choice for reversible electrode reactions, although the mass and volume of the host material reduce the specific charge and the disabled transport of lithium within the host material limits the rate capability. [13]

In Figure 9 are the different concepts of rechargeable lithium batteries based on lithium insertion reactions shown. Figure a) and b) consist both of a metallic lithium as negative electrode at which a) has got a dimensionally stable insertion host material as positive electrode whereas b) uses an electro active polymer like polyaniline or polypyrrole. During the charging/discharging process in such an electro active polymer the release of an anion X⁻ is occurring, which causes irregular salt concentrations. Therefore enough solution must be available to ensure that all salt is dissolved for the whole time. Unfortunately this reduces the specific energy of a battery and so is not desirable. Figure c) and d) consist both a positive dimensionally stable insertion host material at which c) contains a dimensionally unstable negative electrode like a lithium alloy and d) is made up of another dimensionally stable host material as negative electrode, which is also known as rocking chair lithium ion battery. The dimensional stability of the host material during the insertion and de-insertion of Li⁺ ions is very important for a high number of cycles. Large volume changes of the host material cause mechanical stresses and cracks within the electrode which lead to loss of electronic contact, see Figure 10. [13]

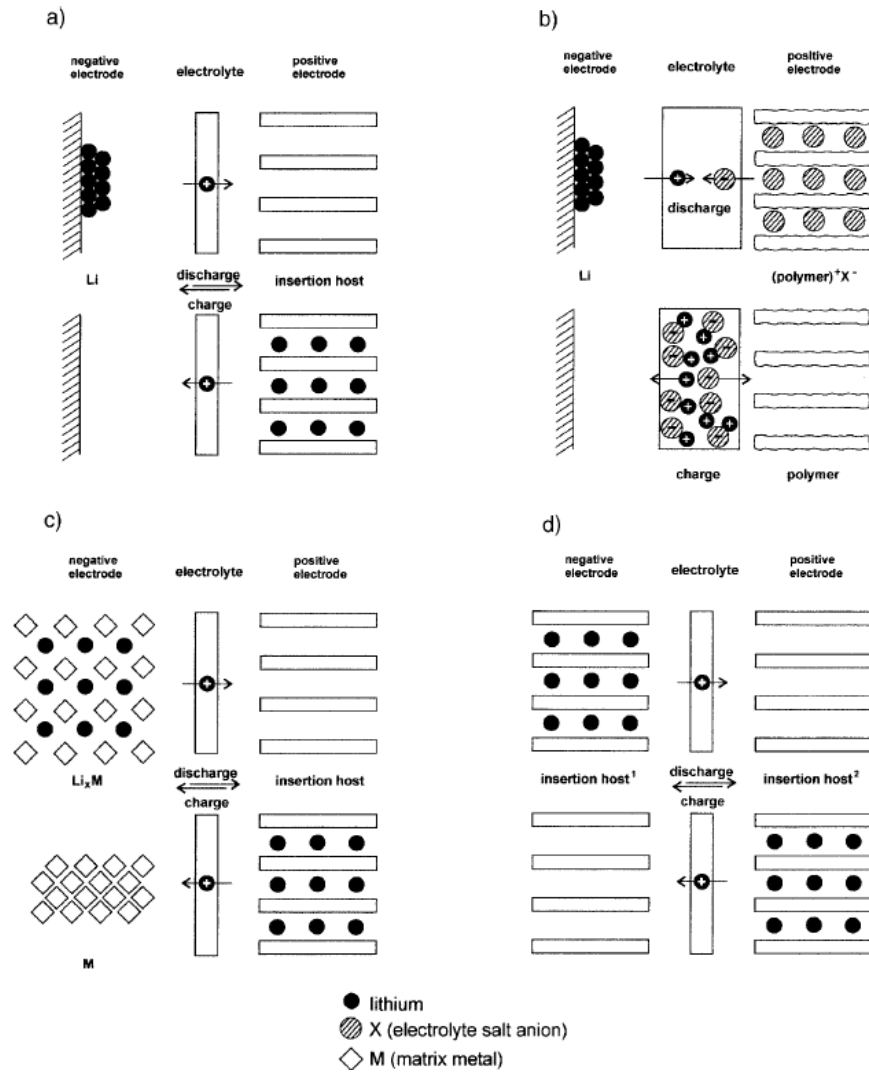


Figure 9: Different concepts of rechargeable lithium batteries based on insertion reactions; a) negative electrode metallic lithium, positive electrode insertion host b) negative electrode metallic lithium, positive electrode anion-exchanging electro active polymer c) negative electrode dimensionally unstable insertion host (Li alloy, Li_xM), positive electrode dimensional stable insertion host d) both electrodes dimensionally stable insertion hosts. [13]

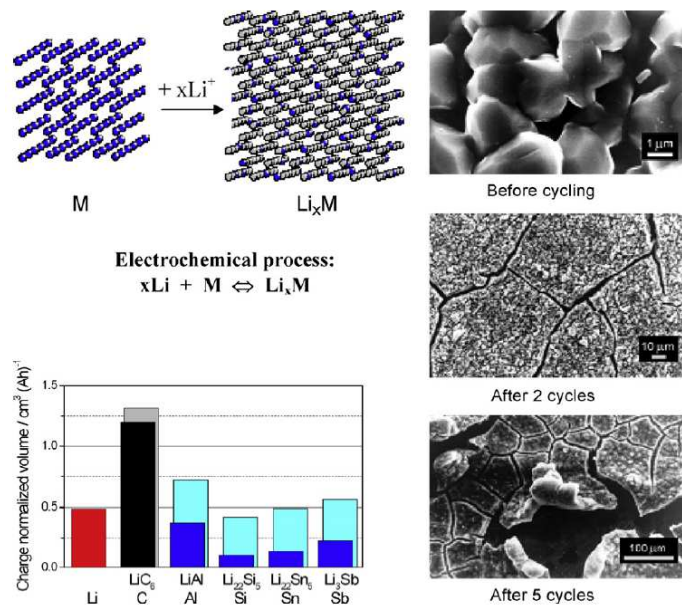


Figure 10: The effect of volume changes of electrode insertion materials during cycling [19]

2.2.3 Electrode-Electrolyte Interplay

The right choice of a proper electrolyte according to the two used electrodes is very important. Figure 11 shows a sketch of the relative electron energies in the electrodes and the electrolyte in a battery system including an aqueous electrolyte under thermodynamically stable condition. E_g is called the window of the electrolyte and is constricted by the HOMO (highest occupied molecular orbital) and LUMO (lowest unoccupied molecular orbital) of the electrolyte. The two electrodes are called Anode (oxidant) and Cathode (reductant) and their electrochemical potentials are μ_A and μ_C . If the anode has got a higher electrochemical potential than the LUMO, it will reduce the electrolyte until a passivation layer is formed, which prohibits the electron transfer between the anode and the electrolyte. A cathode with a lower electrochemical potential will oxidise the electrolyte until a protective passivation layer is built up. To avoid these undesirable side reactions it is necessary to choose two electrode materials, which have an electrochemical potential within the window of the present electrolyte, see Figure 11. The building of a passivation layer on the electrode surface, which is called SEI (solid electrolyte interphase) layer, enables the battery to a bigger open circuit voltage V_{oc} without any degradation of the electrolyte. [7]

Equation 17: Restriction of the open circuit voltage of a thermodynamically stable battery [7]

$$eV_{oc} = \mu_A - \mu_C \leq E_g$$

e... magnitude of electron charge, V_{oc} ... open circuit voltage, E_g ... electrochemical window of electrolyte, μ_A , μ_C ... electrochemical potential of anode and cathode

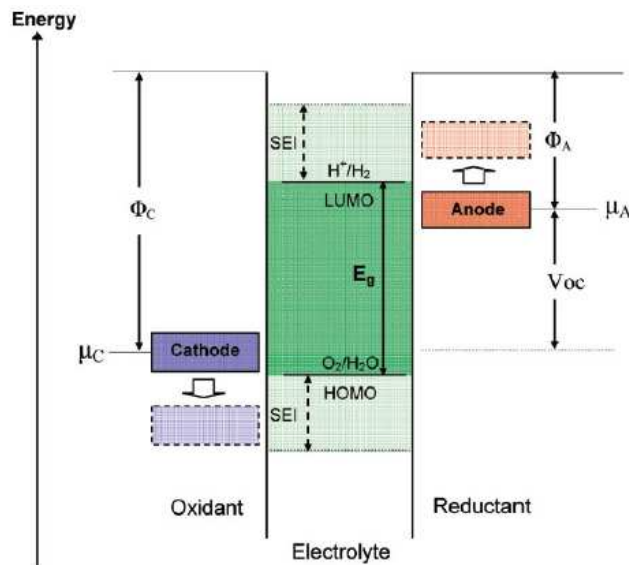


Figure 11: Sketch of an open-circuit energy diagram of an aqueous electrolyte. Φ_A and Φ_B are the work functions of the anode and cathode. E_g is the window of the electrolyte with thermodynamic stability. [7]

If the battery is discharging the anode releases electrons, which run via an external circuit to the cathode. In the meantime cations were emitted by the anode into the electrolyte and migrate to the cathode to maintain the charge neutrality in the two electrodes. If the battery is charging the processes occur the other way round. The release and the transportation of the cations in and through the electrolyte is a very slow process compared to the electron movement in the external circuit. However these two processes are linked together and therefore at high current densities the charge neutrality at the electrodes cannot be reached anymore due to the slow motion of the cations within the electrolyte and the electrode/electrolyte interface. This is the reason why the capacity of reversible charge transfer per unit weight Λ (Ah/g) between the two electrodes decreases with increasing current density. The capacity multiplied with the open circuit voltage describes the energy density of a battery. [7]

As already mentioned the open circuit voltage is limited to the window of the electrolyte. An aqueous electrolyte has an electrochemical window of only about 1.3 eV and therefore it is necessary to change the aqueous electrolyte against another one like an organic for example to be able to gain a higher open circuit voltage and hence also a higher energy density of the battery. Fortunately a lot of lithium salts are soluble in organic solvents and therefore it enables the operation of the lithium ion battery. The electrochemical potential of lithium metal is higher than the most LUMOs of common non-aqueous electrolytes. The reason why it is used anyway as an anode is the formation of the SEI layer at the interface between electrode and electrolyte. [7] The SEI layer consists of reduction products of the non-aqueous electrolyte, see Table 1, and allows Li^+ transportation, but prevents electron transfer. This explains the stability of the electrodes like lithium or graphite in lithium salt solutions in non-aqueous polar aprotic solvents. [21] The SEI layer formed upon metal lithium during charge/discharge cycle is not stable and so dendritic lithium can be plated onto the lithium metal where the SEI layer is broken. These dendrites are potentially a safety hazard due to their risk of growing through the electrolyte and contacting the positive electrode causing a short circuit to occur within the cell, which could lead to cell explosion through thermal runaway. To design a safe battery it is necessary to use electrodes with electrochemical potentials within the window of the electrolyte or to use an electrolyte which forms very quickly a stable SEI layer every time the layer is broken. [7]

Table 1: Reduction products of non-aqueous lithium salt solutions [21]

Solution species	Main reduction products (not all)	Potential range vs. Li/Li ⁺
O ₂	LiO ₂ ; Li ₂ O ₂	1.5–2 V
H ₂ O	LiOH	1.5–1.2 V
HF, PF ₅	LiF, Li _x PF _y	1.8 V and below
Ethers	ROLi	Below 0.5 V
Esters	ROCO ₂ Li (carboxylates)	Below 1.2 V
Alkyl carbonates	ROCO ₂ Li, ROLi	Below 1.5 V
EC	(CH ₂ OCO ₂ Li) ₂ , C ₂ H ₄	Below 1.5 V
PC	CH ₃ CH(OCO ₂ Li) CH ₂ OCO ₂ Li	Below 0.5 V
	CH ₃ CH = CH ₂	
DMC	CH ₃ OCO ₂ Li, CH ₃ OLi	Below 1.2 V
LiClO ₄	LiCl, LiClO _x	Below 1 V
LiPF ₆	LiF, Li _x PF _y	Below 1 V
LiN(SO ₂ CF ₃) ₂	LiF, LiCF ₃ , LiSO ₂ CF ₃ , Li ₂ NSO ₂ CF ₃	Below 1 V

2.2.4 Electrolytes

In this work, the term electrolyte refers to the solution of both the solvent and the salt. This is contrary to the nomenclature in physical chemistry, which defines the electrolyte as only the salt alone.

The electrolyte should have a large electrochemical window to allow an open circuit voltage bigger than 4 V. It should also have a high Li⁺-ion conductivity ($\sigma_{\text{Li}} > 10^{-3}$ S/cm) and a low electronic conductivity ($\sigma_{\text{e}} < 10^{-10}$ S/cm) over a temperature range of $-40 < T < 60$ °C, a high transference number $\sigma_{\text{Li}} / \sigma_{\text{total}}$ of about 1, where σ_{total} includes every ion conductivity, a chemical stability over all used temperatures and a chemical stability related to the two electrodes including a quick regenerating SEI layer as already described in 2.2.3. Additionally it is also necessary that the utilised materials are safe, desirably non –flammable and non-explosive in the case of short-circuit, cheap, non-toxic and hopefully environmental friendly to be able to commercialise the battery. [7]

The characteristics which a suitable lithium-ion battery electrolyte must fulfill are listed below [29, 30]:

- It should be able to dissolve salts to sufficient concentration. In other words it should have a high dielectric constant (ϵ).
- A good ionic conductivity (> 1 mS cm⁻¹) in order to minimise internal resistance

- It should be fluid (low viscosity η), so that facile transport can occur
- Stable in a wide electrochemical potential window from 0 to 5 V vs. Li/Li⁺
- Good thermal (up to 90°C) and chemical stability
- Compatibility with other cell components
- Low cost, low toxicity and low flammability

Six classes of electrolytes are used or under development within lithium-ion batteries:

2.2.4.1 Organic Liquid Electrolytes

About twenty years ago alkyl carbonates, like ethylene carbonate [14], dimethyl carbonate (DMC), ethyl methyl carbonate (EMC) and diethyl carbonate (DEC), and the lithium salt lithium hexafluorophosphate (LiPF₆) was found to be the optimum choice as an electrolyte in lithium ion batteries. Reasons for the good behaviour of EC-DMC/LiPF₆ as an electrolyte solution are the high ionic conductivity down to -15°C thanks to their relatively low viscosity compared to other electrolytes, the anodic stability of both solvents due to the carbonate group and a low number of C-H bonds, the good solubility of LiPF₆ which causes a high conductivity. Furthermore these solutions form good passivation layers on Aluminium, which is used as current collector of cathodes in lithium ion batteries, as well as on Graphite due to the ethylene carbonate. [7, 21] The protective SEI layer on graphite consists of a three dimensional network of ROCO₂⁻ and ROLi⁻ species linked together with Li⁺ ions and therefore it is highly conductive to Li⁺ ions. The disadvantages of the EC-DMC/LiPF₆ solution as an electrolyte are the low ionic conductivity below -15°C, the high viscosity of the solutions which cause a bad wetting of the electrodes and the fact that LiPF₆ decomposes in LiF and PF₅ at higher temperatures. PF₅ is a strong Lewis acid and reacts with traces of water to HF and PF₃O. HF again reacts destructive with the cathode material as well as with the SEI layer of the anodes. [21]

In Figure 12 are the chemical structures of the alkyl carbonates and the electrochemical windows of solutions with tetraalkyl ammonium and lithium salts shown. The

electrochemical windows are measured by a potentiostat with the aid of inert electrodes such as platinum or glassy carbon. If tetra alkyl salts are used in each solution the intrinsic electrochemical window without any passivation phenomena can be measured. By using a lithium salt instead of tetra alkyl salt the electrochemical behaviour of the electrolyte changes dramatically. [21]

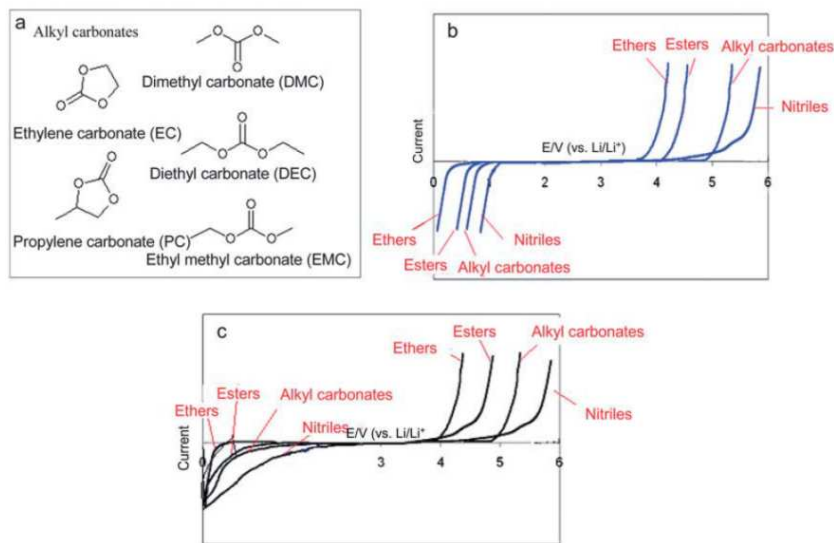


Figure 12: Different alkyl carbonates as selection of electrolyte solutions for lithium ion batteries a) chemical structure b) electrochemical windows with tetraalkyl ammonium (TAA) salt solutions c) electrochemical windows with lithium salt solutions; measured with inert electrodes like Pt or glassy carbon [21]

Another possible lithium salt, which could be used as Li^+ transport species in organic solvents, is LiClO_4 . In Figure 13 are shown FTIR (Fourier-Transform-Infrared-Spectroscopy) spectra, measured with a low polarized nickel mirror electrode, of the salts a) LiClO_4 and b) LiPF_6 in a mixture of EC-DMC (1:1). In the solution of LiClO_4 are no acid species compared to LiPF_6 and so there is formed a surface layer of the alkyl carbonates moieties ROCO_2Li and ROLi . The spectrum of LiPF_6 consists of the alkoxy species ROLi and Li_xPF_y species. The existing HF in the solution reacts with ROLi and ROCO_2Li to solid LiF and ROH or ROCO_2H . This is the reason why the spectrum, compared to the one with LiClO_4 , consists of less peaks. In such a solution the built surface layer is also made up of $(\text{CH}_2\text{OLi})_2$ species, which act too protectively. [21]

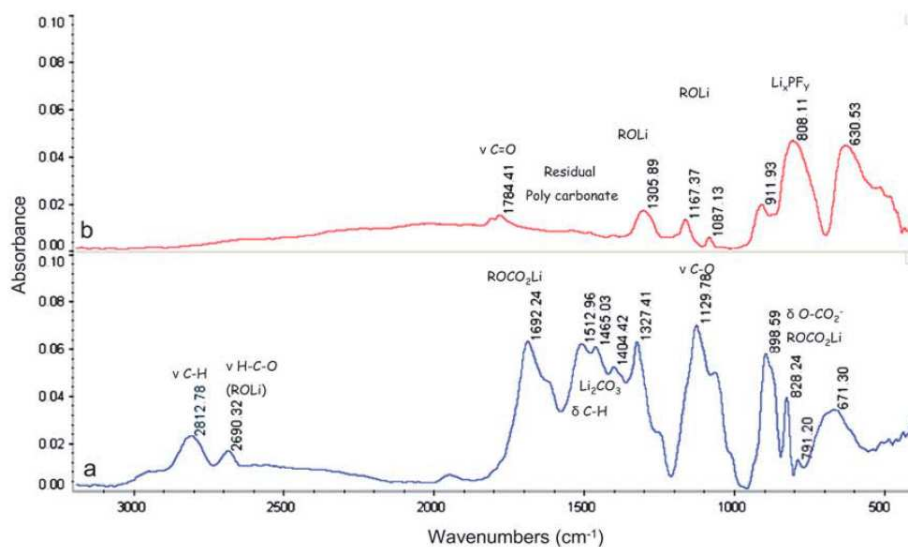


Figure 13: FTIR spectra measured with low polarized nickel electrodes a) 1 M LiClO₄ in EC-DMC (1:1) b) 1 M LiPF₆ in EC-DMC (1:1) [21]

2.2.4.2 Ionic Liquids

Ionic liquids are salts with a very low melting point due to the weak interaction between a large organic cation for example imidazolium or pyrrolidinium and a high charged delocalized anion like N,N-iso(trifluoromethane)sulfonimide (TFSI). They are liquid at room temperature, environmentally friendly, stable over a wide temperature range up to 300-400 °C and have high lithium salt solubility, a high oxidation potential of about 5.3 V vs. Li⁺/Li⁰, a low toxicity and a low vapour pressure. In addition they have a lower flammability when compared to organic solvents. The disadvantages of ionic liquids are their low stability at low reducing voltages like at the lithium metal or graphite anode surfaces and their relatively high viscosity, which causes a lower Li⁺ conductivity. To gain a better Li⁺ conductivity a mixture with liquid carbonate can be used, which of course increase the flammability of the solution. Furthermore the interfaces between ionic liquids and the solid electrode surfaces are not very well investigated so far, but to be able to use ionic liquids in a battery system it is very important to know all possible reactions at the electrode/electrolyte interfaces. Another disadvantage of ionic liquids is their present high cost. [3, 7, 19, 31]

2.2.4.3 *Inorganic Liquid Electrolytes*

A solution of LiAlCl_4 and SO_2 , which is not flammable, has a good Li^+ conductivity at room temperature about 70 mS/cm and a good electrochemical stability, but unfortunately the electrolyte suffers from poor cycling efficiencies and a high lithium corrosion. [32-34]

2.2.4.4 *Solid Polymer Electrolytes*

To get rid of the hazardous electrolyte behaviour like flammability and to get electrolytes with a wider electrochemical window up to 5.5 V, to be able to use highly oxidising positive electrode materials ($> 4 \text{ V vs. Li/Li}^+$), people investigated solid electrolytes like polyethylene oxides (PEOs) containing lithium salts like LiXF_6 ($X = \text{P, As, Sb}$). [9] An advantage of solid electrolytes is that they can be used simultaneously as a separator for the two electrodes and that they allow higher design flexibility. PEOs are cheap, non-toxic and have a good chemical stability, but unfortunately they have a very low Li^+ conductivity ($\sigma_{\text{Li}} < 10^{-5} \text{ S/cm}$) at room temperature due to their restricted chain rotations below the glass transition. A modification with plasticisers, ionic liquids and liquid crystals with a 3D nanometre sized pore structure are going to be better investigated to boost the lithium ion conductivity. [9, 11]

Another polymer electrolyte is made of polyvinylidene fluoride (PVdF), which has an ionic conductivity of about 0.1 S/m at room temperature, high electrochemical stability, good processability and good mechanical properties. Also composite membranes including nanofibres of organomodified clay were made up of PVdF, which have a high tensile strength and a great lithium ion conductivity over a big temperature range. [11]

2.2.4.5 *Inorganic Solid Electrolytes*

Inorganic solid electrolytes with a Li^+ conductivity of $\sigma_{\text{Li}} > 10^{-4}$ S/cm and a wide electrochemical window have been investigated, but due to their worse retention of the electrode/electrolyte interface during volume changes of the electrode materials they have only been used in thin film battery systems. [7]

2.2.4.6 *Hybrid Electrolytes*

A new area of investigation are hybrid electrolytes, which consist of two different kinds of electrolytes to gain each advantages and hopefully to suppress their disadvantages. For example a polymer gel electrolyte and ionic liquid polymer gel electrolyte are made up of an organic liquid or an ionic liquid within a polymer electrolyte. Also mixtures of polymer electrolytes with inorganic solid electrolyte are under investigation. [7, 11]

2.2.5 Negative Electrode Materials

Lithium is the most electro negative (-3.04 V vs. standard hydrogen electrode) and additionally lightest metal (equivalent weight $M=6.94$ g/mol, specific gravity $\rho=0.53$ g/cm⁻³), which enables high energy storage systems. [9] Unfortunately it suffers from low cycling efficiency (< 99 %) leading to a large excess of lithium metal which has to be added and therefore the practical specific capacity of lithium metal is much lower than predicted. Nevertheless the potentials of the lithium insertion materials are higher (vs. Li/Li^+) than the one of lithium metal and so the reachable cell voltage is lower compared to a cell containing lithium metal as negative electrode. In spite of everything lithium metal is presently considered to be too dangerous for usage in secondary batteries, due to dendrite formation leading to hazardous short circuit reactions. [13] Though major research efforts are working to create a stable and safe Li metal anode [35-38].

The common electrode reactions in secondary battery systems can be divided into three different working mechanisms: insertion, conversion and alloying, see Figure 14. [10, 21]

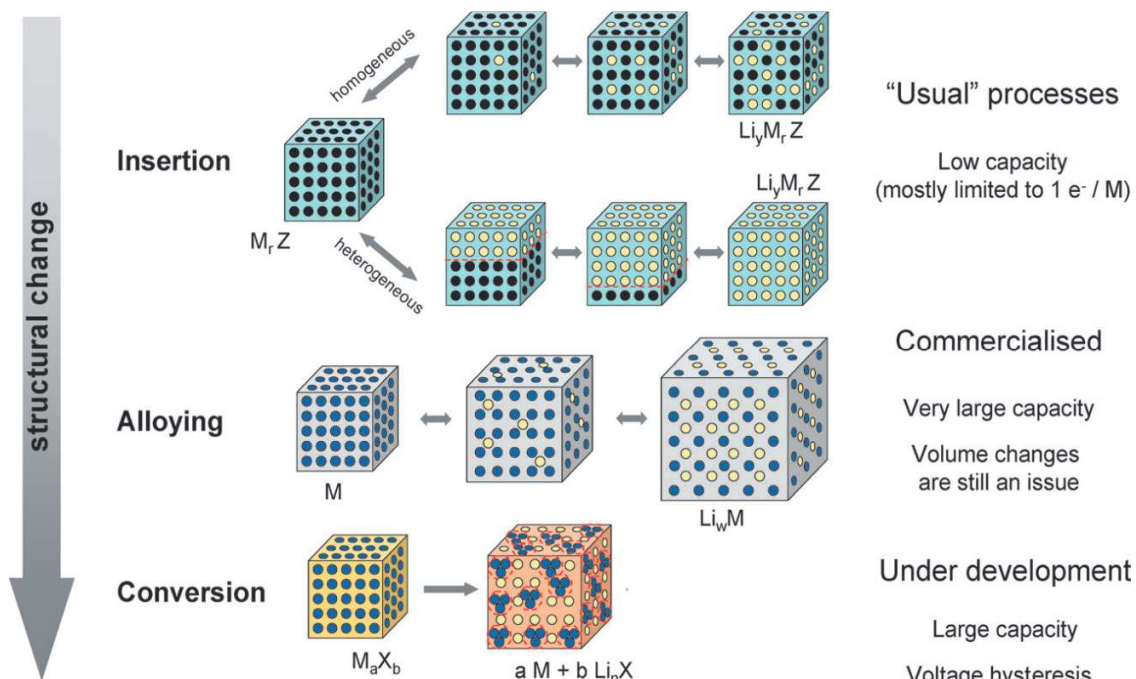


Figure 14: Working mechanisms of secondary battery electrodes: Insertion, alloying and conversion. Black: voids in the crystal structure; yellow: lithium; blue: metal [10]

2.2.5.1 Insertion reactions

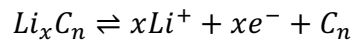
Graphitic carbon and $Li_4Ti_5O_{12}$ are the two most important intercalation materials in secondary lithium ion battery cells. [13]

- *Carbon*

Graphitic carbon is the most utilized negative electrode material in common secondary lithium batteries, caused to its higher specific charge, lower negative electrode potential compared to other common materials and its great dimensional stability during cycling.

The intercalation reaction of lithium into carbon is shown in Equation 18. It is a highly reversible reaction where lithium ions from the electrolyte penetrate into the carbon due to its electrochemical charge. [13]

Equation 18: Lithium intercalation into carbon in secondary lithium ion battery cell [13]



The electrochemical behaviour of carbon depends on its crystallinity, microstructure and micromorphology determined by the different numbers of available free lithium intercalation spots. Therefore a lot of different carbon materials were investigated, which could be classified into two main groups: the graphitic and the non-graphitic carbons. The graphitic carbons have got a layered structure including structural defects, caused by its low transformation energy from the hexagonal into the rhombohedral graphite, and hence also a lot of materials consisting only aggregates of graphite crystallites are called graphites. The non-graphitic carbons have a planar hexagonal network without any far reaching crystallographic order in the c-direction. It consists of cross linked graphitic like carbon phases embedded in an amorphous carbon material. Due to different ratios of the mechanically softer graphitic carbon and the mechanically harder amorphous carbon non graphitic carbons are divided into soft and hard carbons. [13]

Lithium inserts at ambient conditions into highly crystalline graphitic carbons to a maximum stoichiometry of one lithium atom per six carbon atoms ($x \leq 1$ in Li_xC_6) with a specific capacity of 372 mAh/g. [23] Compared to the basal planes the intercalation at the prismatic surfaces is possible without any structural defects. During the intercalation process the distance between the graphene layers increases moderately and the configuration shifts from an ABA structure to an AAA one, whereat lithium intercalates among two graphene layers avoiding the nearest neighbours, see Figure 15. [13]

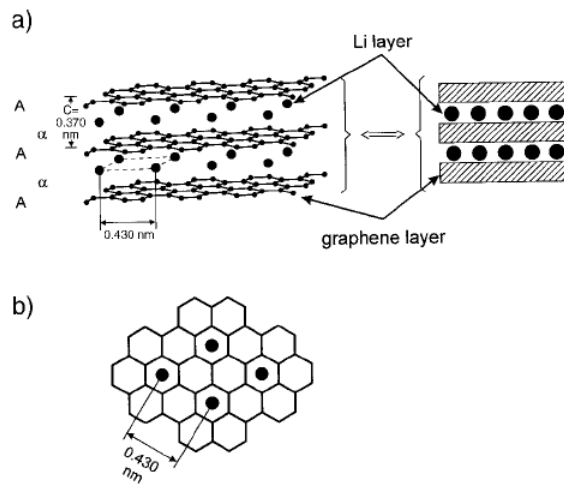


Figure 15: Sketch of lithium intercalation process a) among graphene layers b) distribution within a planar layer [13]

At low lithium guest atom concentrations within the graphite the intercalation is accompanied by a stepwise formation of periodic arrays of unoccupied layer gaps. This process is also known as stage formation characterised by the stage index s , which is equal to the number of graphene layers between two lithium guest layers. The reason for its appearance and therefore the energetically favoured distribution of lithium ions are on the one side the necessary energy to widen the gap between two graphene layers and on the other side the energy of the repulsive interaction between all lithium atoms. In Figure 16 left is shown a sketch of a galvanostatic reduction process of graphite at which the plateaus characterise the two phase regions. Figure 16 right shows a voltammetric curve of the intercalation process of lithium in carbon whereat this time the peaks indicate the two phase regions. Step II is divided into II and II L, because of different lithium packing densities. The experimental galvanostatic measurement of the staging phenomenon presents no sharp discontinuities, caused by variations of the packing density of Li_xC_6 and the occurrence of overpotentials, which results in plateau sloping and peak broadening depending on the used method. [13]

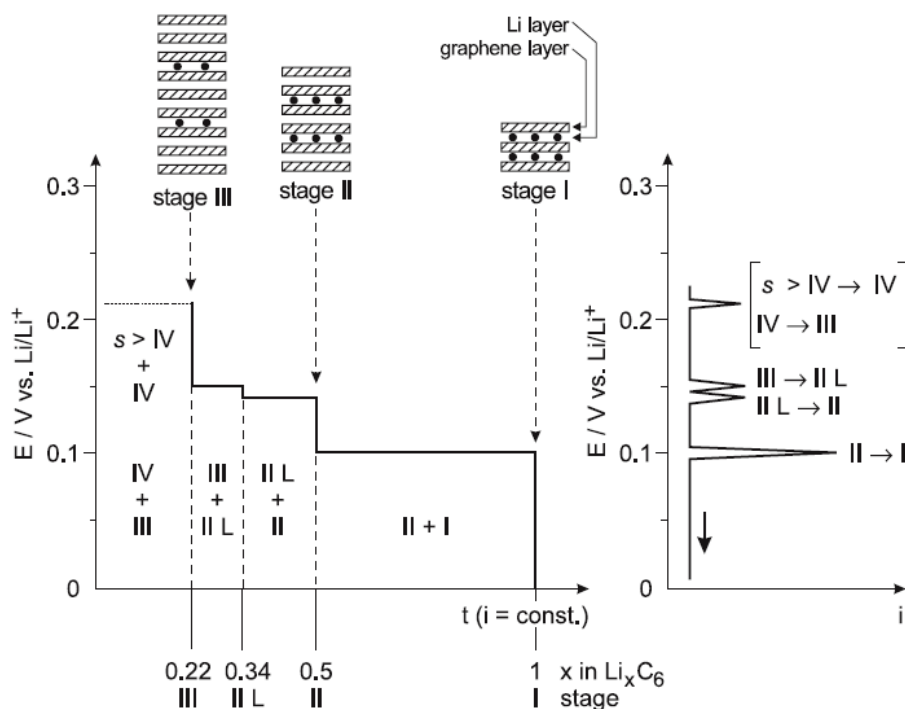


Figure 16: Stage formation during lithium intercalation process into graphite, left: schematic galvanostatic curve, right: schematic voltammetric curve [13]

The reversibility of the intercalation process of lithium into carbon is close to 100 %, but due to the formation of a SEI layer and corrosion-like reactions during the first cycle an irreversible charge loss occurs and hence the charge recovery after the first cycle is just 80-95 %. This irreversible charge loss is a function of the crystallinity and morphology of the carbonaceous material and the composition of the electrolyte. [13]

During the formation of the SEI layer on graphite there occurs also an intercalation of solvated lithium ions, which greatly expand the graphene layers which can lead to deterioration and exfoliation of the graphite, see Figure 17. The solvated graphite intercalation compounds are not thermodynamically stable and as a result of their reduction with co-intercalated solvent molecules the electrode gets self-discharged. This is of course a big problem. Fortunately the number of intercalated solvent molecules decreases because of the formation of the protective SEI layer, but additionally to the growth of the SEI layer also the internal resistance increases and therefore the power density of a cell gradually decreases with each cycle. Ethylene carbonate used as an

electrolyte forms very quick a great protective film on graphite, which hamper solvent co-intercalation. Due to its high viscosity mixtures with ethers or carbonates like 1,2-dimethoxyethane (DME) and dimethyl carbonate (DMC) were used. Inorganic additives, like CO_2 , N_2O , SO_2 and S_x^{2-} improves the formation of thinner and more compact SEI layers which too prevents the solvent co-intercalation. [39]

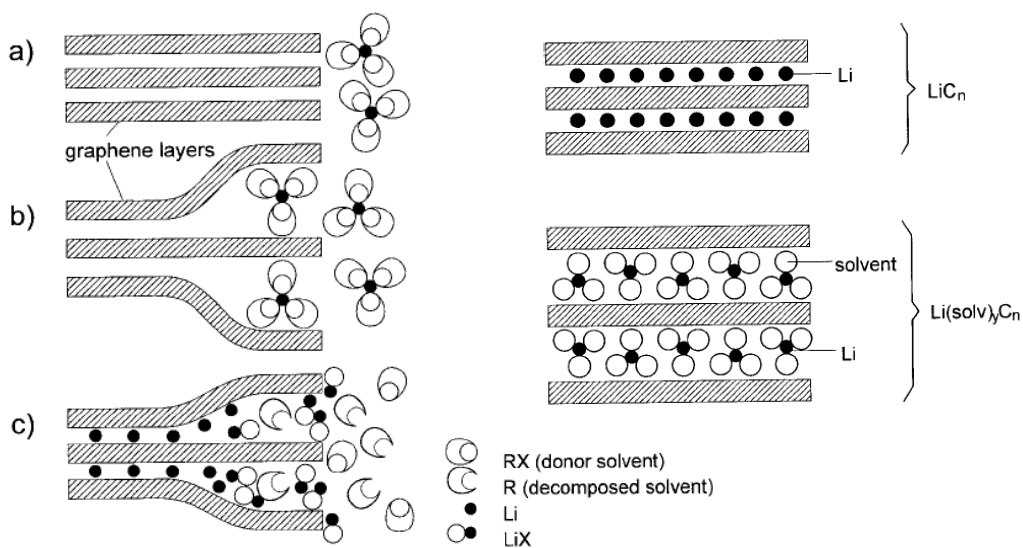


Figure 17: Solvent co-intercalation in graphite left: a) before the reaction b) formation of solvated lithium-graphite intercalation compounds $\text{Li}_x(\text{solvent})_y\text{C}_6$ c) SEI film formation due to decomposition of $\text{Li}_x(\text{solvent})_y\text{C}_6$ right: expansion [39]

Non graphitic carbons can be classified into high and low specific charge carbons, depending whether their lithium storage ability compared to graphitic carbons is higher or lower. On the one hand the existing crosslinks of the graphitic layers in non-graphitic carbons avoid the intercalation of solvent molecules, but on the other hand it also hinders the shift to an AAA structure, which is required for a good lithium intercalation. High specific charge carbons can insert lithium ions up to a stoichiometry of Li_5C_6 (Li_xC_6 with $x = 1.2 - 5$). Therefore these materials have a higher specific charge than graphitic carbons, even though their charge density should be quite the same. Different models were made up to explain the reason for their high lithium storage capability, but they all

differ from the others. Apart from that these materials unfortunately have got problems with extremely high irreversible specific charges, a poor cycle ability and a potential at the end of charge near to 0 V (vs. Li/Li⁺), which causes undesirable lithium deposition at high charge rates. [13]

- *Li₄Ti₅O₁₂*

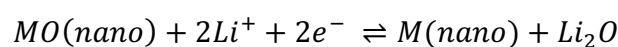
Lithium titanate Li₄Ti₅O₁₂ with the redox couple Ti³⁺/Ti⁴⁺ benefits from rapid charge and discharge properties, due to a high diffusion rate of lithium within this material. It inserts lithium ions up to a stoichiometry of Li₆₋₇Ti₅O₁₂ around 150-160 mAh/g and a voltage of about 1.55 V (vs. Li/Li⁺). [21] The benefits of this material, compared to graphite are its superior reversibility, its structural stability because of the minute volume changes during insertion/deinsertion and a very flat plateau at about 1.55 V. [40, 41] The excellent stability is the reason why this material fortunately does not need any passivation film. Due to its high redox voltage, there occur no redox reactions with the electrolyte if cycled above 1 V. This again causes great cycle ability. [21, 42]

A big drawback of Li₄Ti₅O₁₂ is its insulating character with a band gap energy of 2-3 eV, which limits its use in high currents applications. [43, 44] Therefore a lot of effort is made to improve its conductivity for example by investigating new synthesis methods [45-48], doping [49-54] or including a second phase with high conductivity [55, 56].

2.2.5.2 *Conversion reactions*

Nanoparticles of transition metal oxides like CoO, Co₃O₄, CuO, Fe₂O₃ and Fe₃O₄ and also transition metal phosphides and fluorides react with lithium ions as shown in Equation 19. They have a high reversibility and a capacity up to three times higher than graphite, but suffer from bad performance at elevated temperatures about 60°C and an extreme hysteresis curve during charge/discharge cycling showing the high energy barriers of these reactions. [11, 21]

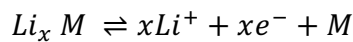
Equation 19: Conversion reactions in secondary lithium ion battery cell [21]



2.2.5.3 Alloying reactions

The formation of lithium with a lot of other metals M, such as Al, Si, Sn, Pb, In, Bi, Sb, Ag, Al, into lithium alloys is a reversible reaction at room temperature as shown in Equation 20. Battery cells including a lithium alloy as an electrode have got high charge densities with moderate current densities, caused by a good Li^+ mobility at room temperature. [13]

Equation 20: Alloying reactions in secondary lithium ion battery cell [13]



During lithiation of the metal steps and slopes occur in the charge/discharge diagrams, due to the formation/backformation of stoichiometric intermetallic compounds and phases Li_xM . Usually the matrix metal changes their structure dramatically within the lithiation, which is accompanied by mechanical stresses and volume changes. Therefore these materials crumble away after a few charge/discharge cycles. Over and above lithium alloys have a high ionic character and so they are usually very brittle, which additionally decreases the lifetime of the lithium alloy electrode. The metallurgical structures and morphologies like grain size, shape, texture and orientation of the lithium alloys are important factors for their dimensional stability during charge/discharge. Very thin electrodes with a very small particle size up to submicron and nanometre are more flexible and the volume change within a particle is small compared to thick electrodes with big particles. This causes fewer mechanical stresses and hence the electrode pulverization is abated and the cycle ability of a cell is improved. [13]

Another idea to suppress the electrode pulverisation is to embed the alloy metals into a ductile conductive matrix so that the volume expansions of the particles can be absorbed. Examples for this kind of electrodes are Sn-Li and Si-Li alloys embedded in a carbon matrix via a core shell mechanism with a specific capacity much higher than graphite and a great reversibility. [19] These two alloy materials have a volume expansion of about 300 % during lithiation and caused to a formation of a protective SEI layer at low potentials they suffer from irreversible charge consumption at each cycle due to the extreme volume changes. Additionally to the idea of the ductile matrix there are

investigations about monolithic Si nanowire carpets, which can be made by etching of silicon or by growing via a CVD process on the right metallic substrate like nickel foil. These nanowires and the core shell mechanism seem to be the best ways of accommodate the big volume changes of lithium alloys till now. [21]

2.2.6 Positive Electrode Materials

There are two main groups of positive electrode materials for rechargeable lithium ion batteries. On the one side materials, which originally include lithium and on the other side materials, which at the beginning do not include lithium and hence have to be combined with an anode containing lithium. These lithium including materials like LiCoO_2 and LiFePO_4 are normally stable in air and de-insert lithium with a potential of about 4 V (vs. Li/Li^+). The other non-lithium containing materials like V_2O_5 and M_3O_4 ($\text{M} = \text{Mn, Fe, Co}$) have to be loaded with lithium in the first cycle at a potential of about 3 V and are not stable in air and moisture in their lithiated state. Therefore these materials are also often called 3 V and 4 V materials. [13]

The most important cathode materials in these days are lithium metal oxides like LiCoO_2 and LiMn_2O_4 , polyanionic materials like LiFePO_4 and organic materials like $\text{Li}_4\text{C}_6\text{O}_6$. [11]

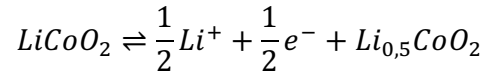
2.2.6.1 Layered metal oxides

Layered metal oxides are the most common positive electron materials for secondary lithium ion batteries. There exist two main groups: the layered structured LiMO_2 ($\text{M} = \text{Co, Mn, Ni}$ and their combinations or substitutions) and the spinel structured LiM_2O_4 . [11]

The most commercialised positive electrode material for secondary lithium ion batteries is the two dimensional host LiCoO_2 . The corresponding lithium insertion reaction is shown in Equation 21, where lithium atoms insert in the octahedral cavities between the layers of edge shared $[\text{CoO}_6]$ octahedra. Theoretically this electrode material possesses a capacity of 274 mAh/g, but due to the high reactivity of its delithiated phases with the electrolyte the capacity is half limited. This can be abated by doping the material with Al

or Cr or coating the material with oxides like ZrO_2 and Al_2O_3 or phosphates like $AlPO_4$ and $FePO_4$. Li/Li_xCoO_2 cells operate with an open circuit voltage of about 3.9 V to 4.7 V. Its advantage is a good cycle ability up to 4.3 V (vs. Li/Li^+) in different electrolytes, which is the reason for its great commercialisation, but in spite of that $LiCoO_2$ suffers from the limited sources of cobalt, thus the high price and additionally the high toxicity of cobalt. These drawbacks boost the motivation to find another cheaper and more environmental friendly cathode material. [11, 13]

Equation 21: Lithium intercalation reaction of $LiCoO_2$ [21]



One of the most interesting cathode materials are $LiNi_xM_{1-x}O_2$ with the more environmental friendly and more abundant metals $M = Mn, Ni, Fe$. These materials like $LiNi_{0.5}Mn_{0.5}O_2$ for example are considered to be safe and inexpensive with a high capacity and a high rate capability. A new core/shell structure was investigated, consisting of a $Li[Ni_{0.8}Co_{0.2}]O_2$ core, which prevents the oxide material of destructive structural transformations during cycling and a thermal instability due to the stable Ni^{2+} in the core, and a $Li[Ni_{0.55}Co_{0.15}Mn_{0.3}]O_2$ shell, which prevents the oxide of decomposition by the aggressive HF from the electrolyte due to the electrochemically inactive Mn at the outside. [11]

Very promising candidates for metal oxide cathode materials are $xLi_2MnO_3 \cdot (1-x)LiMO_2$ ($M=Ni, Mn, Co$). They consist of two materials with a layered structure and provide a higher reversible capacity of about 230 mAh/g compared to $Li_{1-x}CoO_2$ (~140 mAh/g), $Li_{1-x}Mn_2O_4$ (~110 mAh/g) and olivine $LiFePO_4$ (~150 mAh/g) electrodes. The actual electrochemical activation process occurring with $xLi_2MnO_3 \cdot (1-x)LiMO_2$ and the nature of the oxidised species are not yet completely understood. The de-intercalation process of lithium takes place during the initial charging process at a potential of about 4.4 V (vs. Li/Li^+). At higher potentials the Li_2MnO_3 gets activated, which is characterised by a long flat plateau at about 4.5 V, leading to a reversible capacity of about 200 mAh/g. During this activation process more lithium in addition to oxygen gets removed from Li_2MnO_3 ,

but the exact amount of released oxygen could not be measured till this day. Disadvantages of this positive electrode material are manganese dissolution at high electrode potentials, which may affect the lithiated graphite electrode and the protective solid electrolyte interface, the high oxidising potential, which gives rise to undesired reactions with the electrolyte and an occurring fade in the average cell voltage, caused by cycling the cathode several times, which is accompanied by a hysteresis in the charge/discharge profile. [57-60]

2.2.6.2 *Spinels*

A great battery cell for electric vehicles for example contains LiMn_2O_4 as a positive electrode material. The advantages of this material are its safety, due to the chemically stable $\text{Mn}^{3+}/\text{Mn}^{4+}$ couple and its rate capability, thanks to a fast 3D lithium ion mobility network. Unfortunately this material suffers from a gradual capacity loss caused on the one side by a Jahn-Teller distortion of the Mn^{3+} and on the other side by the dissolution of Mn in the electrolyte. Further developments include lithium doping in octahedral sub lattice to hamper the manganese dissolution and LiMn_2O_4 nanorods and nanowires to influence the lattice changes to avoid capacity losses. Nanocrystalline LiMn_2O_4 (≤ 15 nm) possesses a fast lithium insertion and a good cycle ability, due to a solid solution state lithiation. Another interesting development is mesoporous $\text{Li}_{1.12}\text{Mn}_{1.88}\text{O}_4$, which was reported to have a specific capacity 50 % higher than the bulk material. [11]

2.2.6.3 *Polyanionic materials*

Battery cells containing polyanionic-based compounds $\text{Li}_x\text{M}_y(\text{XO}_4)_z$ ($\text{M} = \text{metal}$, $\text{X} = \text{P}$, S , Si , Mo , W) are promising candidates for electric vehicles. Especially olivine LiMPO_4 materials have gained a lot of research interest in the last years. They all have a flat voltage profile thanks to a first order phase transition (e.g. $\text{FePO}_4/\text{LiFePO}_4$) during lithium intercalation and de-intercalation via single ion channels. The lithium transport is a function of the particle morphologies, size, defects and crystallinity and to avoid structural blocking of these single ion channels for Li^+ transfer by M^{2+} ions nano sized particles were investigated. [11, 21]

The olivine structured LiFePO_4 persuades by its high capacity (170 mAh/g), high stability, cycle ability and rate capability, due to its low surface reactivity, which also enables the usage of nanoparticles. Furthermore the ion phosphate is abundant and environmental friendly. The drawbacks of this material are the low intrinsic electronic conductivity ($\approx 10^{-9} \text{ S/cm}^{-1}$) and lithium diffusivity (10^{-10} - $10^{-16} \text{ cm}^2/\text{s}$). One way to boost the electronic and ionic conductivity of the material is via doping and coating with more conductive components like carbon or lithium phosphate. Another way is to use nanometre sized particles so that the path of ionic and electronic transport is abated to a minimum. [11, 21]

Other investigated olivine phases besides LiFePO_4 with similar theoretical capacities are LiMnPO_4 and LiCoPO_4 . They have higher redox potentials ($\text{Fe}^{3+}/\text{Fe}^{2+} \approx 3.5 \text{ V}$, $\text{Mn}^{3+}/\text{Mn}^{2+} \approx 4.1 \text{ V}$, $\text{Co}^{3+}/\text{Co}^{2+} \approx 4.7 \text{ V}$) and therefore also higher energy densities, but their big drawbacks are a capacity loss and a bad kinetic, caused by a low ionic and electronic conductivity and a bigger anisotropic lattice change during lithiation compared to LiFePO_4 . Further approaches related to the safe $\text{LiMn}_{0.8}\text{Fe}_{0.2}\text{PO}_4$ with a high capacity (160-165 mAh/g) and also high rate capability. [11, 21]

Polyanionic materials like fluorophosphates, fluorosulphates and silicates are also under investigation such like $\text{A}_2\text{FePO}_4\text{F}$ ($\text{A} = \text{Na}, \text{Li}$) and LiFeSO_4F , at which a change from $[\text{PO}_4]^{3-}$ to $[\text{PO}_4\text{F}]^{4-}$, $[\text{SO}_4\text{F}]^{3-}$ or $[\text{SiO}_4]^{4-}$ occurs. The benefit of $\text{A}_2\text{FePO}_4\text{F}$ is a 2D intercalation pathway for lithium ions compared to the 1D intercalation pathway of LiFePO_4 and little volume changes during cycling. A higher voltage and a better ionic and electronic conductivity can be gained from LiFeSO_4F . Unfortunately the energy density of this material is not very high and it has to be combined with ionic liquids, which are still very expensive. [11]

2.2.6.4 Organic materials

Interesting sustainable organic materials, such as conducting polymers and oxocarbons, are under discussion as positive electrode materials for lithium ion batteries. Polymers like polyaniline and perylene-tetracarboxylicacid-dianhydride sulphide show good lithium insertion reactions, but the most promising candidate is the tetralithiated salt of tetrahydroxybenzoquinone $\text{Li}_4\text{C}_6\text{O}_6$. It has a good cycle ability between $\text{Li}_2\text{C}_6\text{O}_6$ and $\text{Li}_6\text{C}_6\text{O}_6$ with a capacity of about 200 mAh/g. [11]

2.2.6.5 Vanadium oxides

The oxides of vanadium-, chromium-, niobium- and molybdenum are 3 V cathode materials with a great lithium insertion capacity, but most of them suffer from a bad cycling stability and therefore only the vanadium oxides V_2O_5 and V_6O_{13} established in battery applications. V_2O_5 consists of VO_5 square pyramids, which are connected via their edges and corners, and forms a two dimensional insertion host material, where the lithium ions are intercalated into perovskite-like cavities. V_6O_{13} has a comparable structure with VO_6 octahedral cavities for the lithium insertion. V_2O_5 electrodes are known as very sensitive to overdischarge, due to an irreversible phase transformation (ω - V_2O_5), which prevents the delithiation. The ω - V_2O_5 phase has a rock salt structure and is chemically or electrochemically gained by the insertion of an excess of lithium into V_2O_5 . Furthermore V_2O_5 electrodes suffer from a limited long-term cycling stability. V_6O_{13} can reversibly insert up to six lithium ions, but its drawbacks are a capacity loss during cycling, a high electronic resistivity of lithiated V_6O_{13} and a high volume change of about 15 %. [13]

V_2O_5 crystallizes in the Pmmn space group with an orthorhombic cell structure ($a=11.50$ Å, $c=4.40$ Å) and a D_{2h} point group symmetry. It consists of a layered structure, where the vanadium atom is surrounded by five oxygen atoms resulting in four different V-O bonds. The shortest and strongest apical $\text{V}=\text{O}_1$ bond has a length of $d_1=1.577$ Å, the bridge V- O_3 bond $d_2=1.779$ Å, the two “ladder step” V- O_2 (O_{21} and O_{22}) bonds have a length of $d_3=1.878$ Å and the interchain V- O_2 ($\text{O}_{2'1}$) bond $d_4=2.017$ Å, see Figure 18.

The vibrational modes of V_2O_5 , which can be calculated via the standard table of characters of irreducible representations of the D_{2h} group (see Figure 19), are listed in Equation 22. Regarding that only the *gerade* modes are Raman active (*ungerade* modes are IR active) it follows that in case of V_2O_5 21 Raman active modes are expected. [61]

Equation 22: Optically vibrational modes of V_2O_5

$$\Gamma(V_2O_5) = 7A_g + 7B_{2g} + 3B_{1g} + 4B_{3g} + 6B_{1u} + 6B_{3u} + 3A_u + 3B_{2u}$$

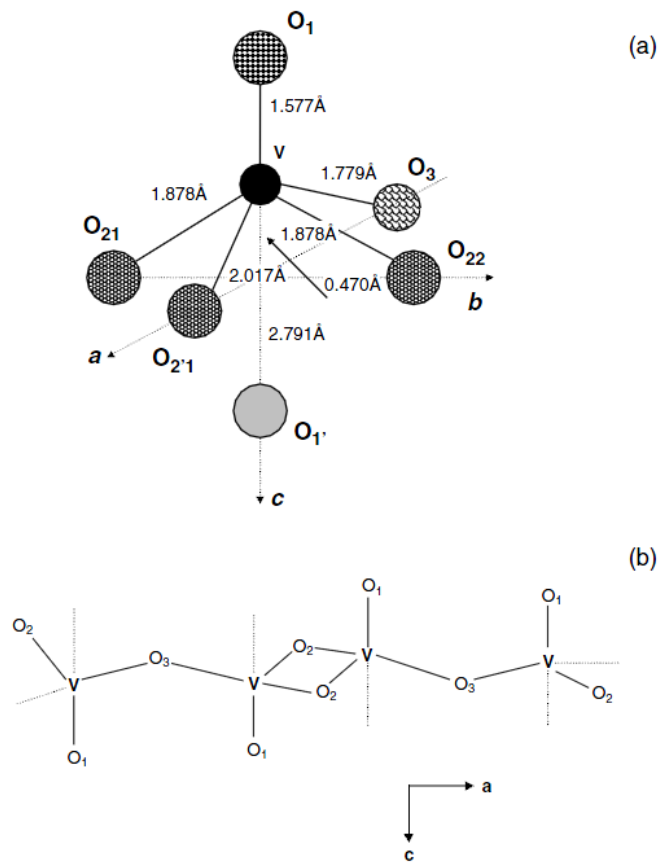


Figure 18: Crystal structure of V_2O_5 a) spatial b) plane projection [62]

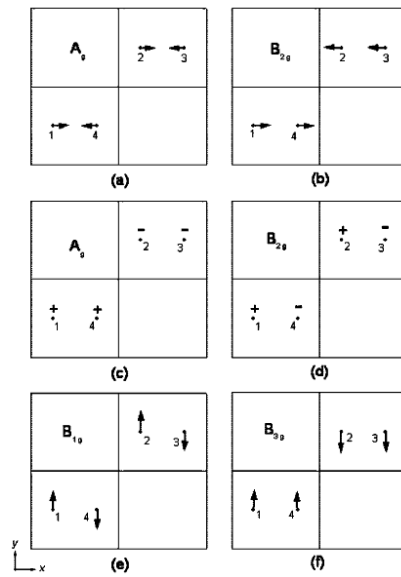


Figure 19: Symmetric atomic displacement combinations for the Pmmn space group. Numbers 1-4 represent four symmetry equivalent atomic positions for a given atom in the unit cell. [61]

In Figure 20 is shown a voltage versus capacity diagram of different positive and negative electrode materials for secondary lithium ion batteries. [9]

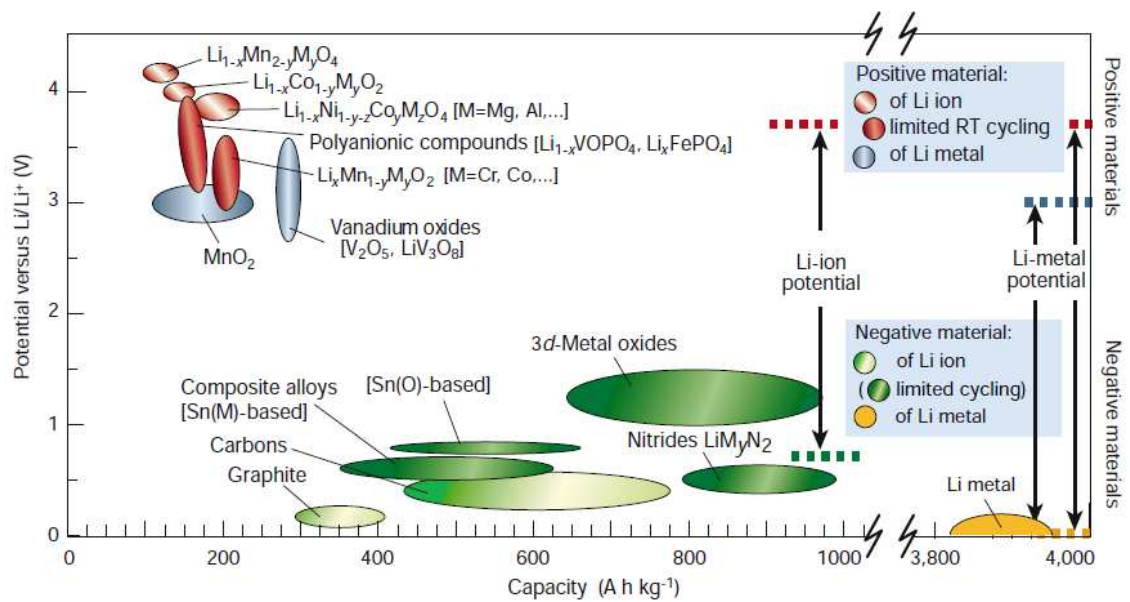


Figure 20: Voltage/capacity - comparison of different positive and negative electrode materials for lithium ion batteries [9]

2.2.7 Current Collectors

Current collectors are used to transport the cell current to and from the electrodes and furthermore they are used as substrates for the electrode materials. Thin films are preferred, because the mass and volume of the current collectors are included in the energy specifications of a battery. Additionally current collectors should have a good mechanical stability, because of stresses during the cell fabrication and cycling and a good chemical stability due to occurring corrosion processes caused by the aggressive materials and extreme electrochemical potentials. [1, 34]

A negative current collector should have a low lithium solubility to prevent intolerable lithium losses in the electrode and to remain its mechanical stability. Copper is usually used in this case, because it is relatively cheap, highly conductive and easily rolled into thin foils. [1] Nevertheless it has to be considered that below 1V cell voltage the copper at the negative electrode can get oxidised and hence copper ions can dissolved in the electrolyte. During the next recharge process these dissolved copper ions coat the negative electrode, which causes capacity loss caused by the hindrance of lithium plating. [34] Aluminium is highly reactive with lithium near to the lithium potential and therefore cannot be used as negative current collector in lithium ion batteries. [63] Nickel is also a good choice for negative electrode current collectors, because of its electrochemical stability within the working potential of 0.01 – 3.0 vs. Li, but unfortunately its very expensive. [64]

On the positive electrode side the current collector should have a great oxidation resistance. Unfortunately the potential of common positive electrodes are often higher than the dissolution potential of a lot of metals and also a lot of lithium salts dissolve metals by forming highly soluble salts. Aluminium is a good choice for a positive current collector due to its naturally forming passivation layer, it's high mechanical strength, excellent ductility, low density, good electrical and thermal conductivity and it's low cost. Aluminium cannot be used as the current collector for negative electrodes as a potential shift to negative values, where Li^+ reduction occurs, is possible. Copper gets oxidised above 3 V and therefore is undesirable as a current collector for positive electrode materials. [1, 64-66]

2.3 Aluminium Ion Battery

Compared to the one electron transfer of Li^+ ions in secondary lithium ion batteries, the aluminium ion Al^{3+} exhibits a possible transfer of up to three electrons per ion. Furthermore aluminium is the most abundant metal element in the earth crust with a lower reactivity than lithium. The outcome of this is that batteries including aluminium ions instead of lithium ions would be cheaper, safer and exhibits a higher energy density. Aluminium metal has a high theoretical capacity and specific energy and therefore people were interested in aluminium anodes like for the aluminium-air battery. [20, 67]

Al^{3+} ion has an ion radius of 53.5 pm and is therefore smaller than the Li^+ ion which has an ion radius of 76 pm. Recent investigations of N. Jayaprakash et al. [67] show that a reversible intercalation of aluminium ions into centimetre long V_2O_5 nanowires with an ionic liquid as electrolyte is possible. In contrast to the malfunctioning PC/THF electrolyte the cyclic voltammogram of the ionic liquid 1-ethyl-3-methylimidazolium chloride containing the salt AlCl_3 exhibits a cathodic peak at ~ 0.45 V and an anodic peak at ~ 0.95 V in the potential window of 2.5-0.02 V (vs. Al). These peaks turned out to be stable in their peak position as well as in their current value even after twenty scans. The research group therefore suggests that these peaks could be likely the intercalation and de-intercalation of Al^{3+} into the orthorhombic crystal structure of V_2O_5 . With this investigation they produced a battery cell with an open circuit voltage of 1.8 V and cycled it galvanostatically with 125 mA/g. The well defined insertion plateau at ~ 0.55 V occurred to be stable in its potential and the capacity decreased from 305 mAh/g to 273 mAh/g within the first twenty cycles. This is lower than the theoretical capacity of 442 mAh/g calculated for the three electron transfer from Al^{3+} to V_2O_5 . [67]

S. Lui et al. investigated a TiO_2 nanotube array with a tetragonal crystal structure produced by anodisation and a subsequent calcination step of a titanium foil. Together with an aqueous electrolyte of 1 M AlCl_3 this TiO_2 array shows a cathodic peak at -1.26 V and an anodic peak at -0.84 V (vs. SCE). Aqueous solutions of MgCl_2 and LiCl do not show this behaviour and therefore the group suggests that Aluminium can be reversibly inserted into the TiO_2 nanotubes thanks to its smaller ion radius. Further investigations show a flat discharge plateau at -0.98 V (vs. SCE), which varies strongly with different current densities, and a maximum discharge capacity of 75 mAh/g. [20]

2.4 Batteries Measuring Methods

2.4.1 Electrochemical Methods

In a typical electrochemical experiment are at least two electrodes involved namely the working electrode and the counter electrode. The electrode processes, which are measured during an experiment, occur only at the working electrode. Therefore the counter electrode is just needed to close the electrical circuit and in a two electrode system to act at the same time as a reference electrode. To avoid polarisation effects at the reference electrode, caused by a high current flow through the electrode, a third separated electrode can be used as reference electrode, which helps to stabilise the potential between the working and reference electrode and therefore to get more accurate data. The electrodes are usually immersed in an electrolyte and contacted to a potentiostat, which allows two different measurement methods namely the potentiostatic controlled measurements, where the potential of the cell is controlled, and the galvanostatic controlled measurements, where the current that passes through the cell is controlled. [68, 69]

2.4.1.1 *Cycling Voltammetry - Potentiostatic Controlled Measurements*

In a cyclic voltammetry measurement the potential gets linearly increased from a starting potential E_i to the end potential E_s and subsequently decreased back to E_f , which is schematically drawn in Figure 21. The potential is thereby controlled by a potentiostat at which the scan rate in V/s characterises the speed of the potential sweep. A slow scan rate is usually beneficial for detailed analysis of electrochemical reactions. [64]

It is a very common method, which is often used to investigate the potential at which oxidation or reduction processes occur, the oxidation state of a redox species, the number of electrons involved, the rate of electron transfer, possible chemical processes associated with the electron transfer and adsorption effects. [14]

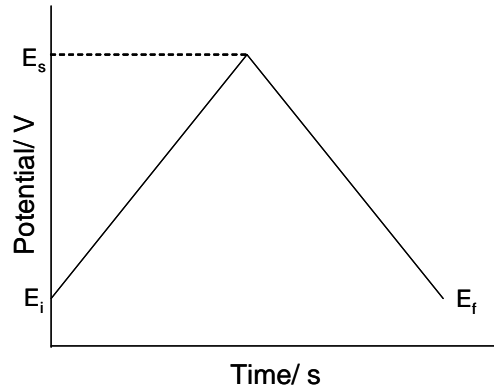


Figure 21: Potential wave of a cyclic voltammetry measurement

2.4.1.2 Galvanostatic Controlled Measurements

In a galvanostatic measurement the potentiostat applies a constant current, which runs through the cell between the working and counter electrode, until a certain defined potential is reached. A negative current for the working electrode causes reduction and a positive current oxidation. The biggest advantage of a galvanostatic measurement compared to cyclic voltammetry is, that the electrode process in a battery system can be investigated under real working conditions. The constant current method provides information about the capacity, reversibility, resistance and the rate of diffusion of a battery cell. [14, 64]

2.4.1.3 Impedance

Another often used method to characterise batteries is the impedance spectroscopy. The impedance of an electrode or battery is described by the addition of a real and an imaginary part, see Equation 23. The imaginary part X is given in Equation 24 and the angular frequency ω is shown in Equation 25. The imaginary unit j is $\sqrt{-1}$. [8]

Equation 23: Impedance [8]

$$Z = R + j\omega X$$

Z ... impedance, R ... real part resistance, j ... imaginary unit, ω ... angular frequency [rad/s], X ...imaginary part

Equation 24: Imaginary part X of Impedance [8]

$$X = \omega L - \frac{1}{\omega C}$$

X ...imaginary part, ω ... angular frequency [rad/s], L ... inductance, C ... capacitance

Equation 25: Angular frequency [8]

$$\omega = 2\pi f$$

ω ... angular frequency [rad/s], π ... Pi, f ... frequency [1/s]

In Figure 22 is given a typical battery circuit diagram with the corresponding impedance diagram. C_{DL} is the capacitance of the double layer at the interface between electrode and electrolyte. Z describes the impedance of the electrode reactions and W is a Warburg impedance which occurs at diffusion processes. The activation polarisations are given by the semi circles with each frequency which is associated to the relaxation processes. The diffusion polarization is characterised by a 45° line also known as Warburg impedance. The ohmic polarisation has not got any capacitive character and therefore it is independent of the frequency. The relaxation time τ is given by the frequency of the maximum of a semi-circle, see Equation 26. [8]

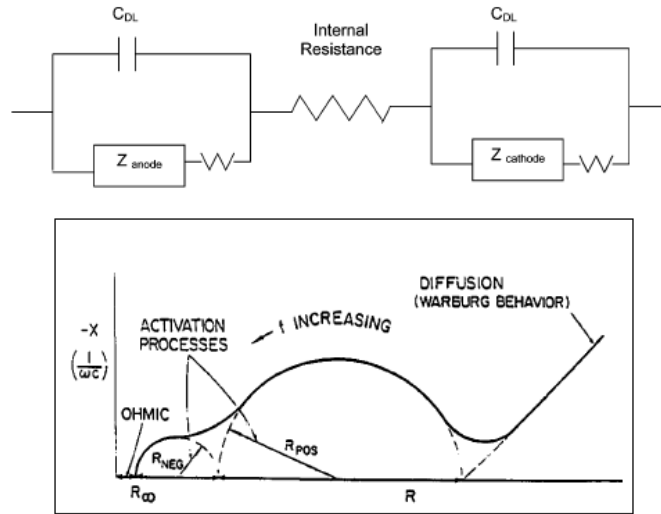


Figure 22: Typical battery circuit diagram (top) with corresponding Impedance diagram with all three kinds of polarization effects (bottom) [8]

Equation 26: Relaxation time in Impedance measurement [8]

$$\tau = \frac{1}{f_m} = RC$$

τ ... relaxation time [s], f_m ... frequency of maximum [1/s], R ...resistance related to the exchange current for the reaction [Ω], C ... polarization capacitance [C/V]

2.4.2 Other Techniques

During charge and discharge of a rechargeable lithium ion battery the host material usually undergoes a structural change, due to the intercalation or de-intercalation of lithium ions. Furthermore these processes are often accompanied with a loss of specific capacity, reversibility, rate capability and cycling behaviour. To improve the electrochemical behaviour of a rechargeable battery it seems to be necessary to understand better the connection between electrochemical and structural changes. X-ray, neutron and electron diffraction for example help to get long-range information about the structural changes during charge and discharge of an electrode material. In contrast to these techniques X-ray absorption, nuclear magnetic resonance (NMR), electron paramagnetic resonance (EPR) and X-ray photoelectron spectroscopy (XPS) provide short range data. A very useful non-destructive method is the Raman spectroscopy, which allows the detection of structural changes in the atomic range like local disorder, changes

in bond lengths, bond angles, coordination, Li dynamics and cation ordering. [70] With the aid of all these different techniques people try to investigate the properties and interactions of the electrode materials to improve the lifetime, performance and thermal stability of a battery. [8]

A key issue to get nearer information about the happening at the electrode surfaces is to measure *in situ*, which means to measure during charge or discharge of the battery. This kind of measurement is accompanied with a lot of problems, because often the electrolytes as well as the electrodes and the possible emerging surface films are very sensitive to moisture, oxygen or CO₂, which means, that their properties change by exposing them to atmosphere. Furthermore an exposure to vacuum causes a loss of volatile components, shrinkage of the film and chemical changes in the surface film, which also limits the *in situ*-measurements of X-ray photoelectron spectroscopy or Auger electron-spectroscopy. [71]

2.4.2.1 Raman spectroscopy

To improve an electrochemical cell it is very important to get a better fundamental understanding of the basic reactions that occur at the interface between electrode and electrolyte and hence to be able to investigate new solid-solid and solid-liquid interfaces. [72] Therefore it is necessary to use surface sensitive techniques like Raman spectroscopy to be able to follow the electrode surface behaviour during ion intercalation and de-intercalation. [73]

The Raman Effect is named after Sir C. V. Raman, who is one of its first discoverer in 1928. If a photon impinges at a molecule it can be either absorbed or scattered to a virtual state, which has less energy than an electronic state. The Rayleigh scattering is marked by the same energy (frequency) and therefore same wavelength of the scattered light compared to the incident photon. This kind of scattering is also called elastically scattering and occurs when no changes in the atomic coordinates of the molecule happen. The Raman scattering occurs by exciting a vibrational motion of the molecule, which leads to a change in the polarisability describing how easily the electron cloud around a molecule can be distorted. During this so called inelastically scattering, which happens only to 1 of 10⁷ photons, the photon loses or gains energy. Depending whether the

energy gets transferred from the photon to the interacting molecule or the other way round, the scattering is called Stokes scattering or Anti-Stokes scattering, see Figure 23a. The Anti-Stokes Raman scattering is dependent on excited ground states, which are usually lesser than the ground state population and therefore the signal is much weaker compared to the Stokes Raman scattering signal, see Figure 23b. The typical Raman Spectrum plots the frequency difference to the incident photons the so called *Raman shift* against the intensity. Because of the Raman shift these spectra are independent of the frequency of the original photons. [61, 70]

With the help of the group theory it is possible to figure out which vibration modes are Raman active and which are not. [74]

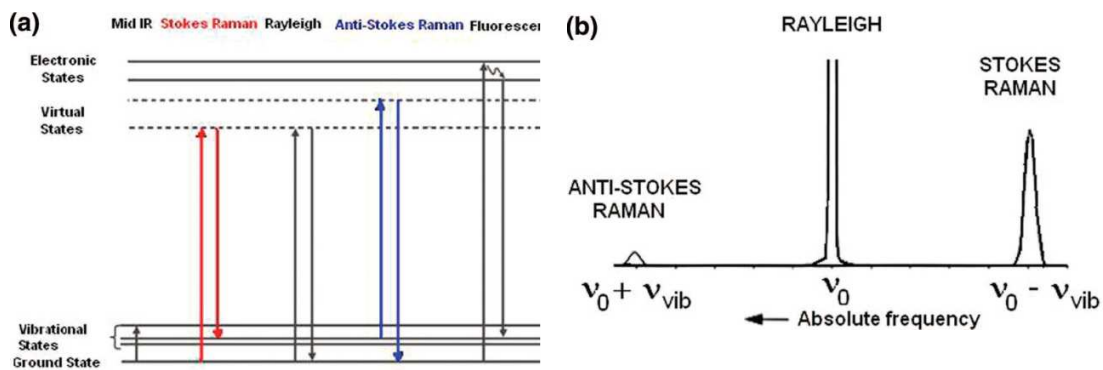


Figure 23: a) Energy level diagram of different processes and b) Raman and Rayleigh scattering of an excitation frequency ν_0 and a molecular vibration of the sample ν_{vib} . [61]

The schematic instrumentation of a Raman spectrometer is shown in Figure 24. A laser with its monochromatic light and high power is used as light source to ensure enough detectable Raman signal. With the help of a microscope objective the laser is focused on the sample. This same objective collects the backscattered Raman light and forwards the information via a Holographic Notchfilter to a charge coupled device (CCD) detector. Therefore high numerical aperture microscope objectives are needed to improve the spatial resolution ($\sim 1 \mu\text{m}^2$) and the optical collection power. The holographic Notchfilter consists basically of a glass plate coated with a polymer film. On the one hand side it

highly reflects the wavelength of the incident laser and on the other hand side it lets pass all other wavelengths. Therefore the backscattered Rayleigh light gets separated from the Raman signal, which leads to a higher sensitivity. The CCD detector is made of many little integrated circuit chips containing thousands of little picture elements (pixels), which are very sensitive to light. Hence it is possible to measure the whole spectrum in less than a second and with a very low laser power. A video camera together with a white light source allows having a look at the sample through the microscope. [61, 75]

During an *ex situ* measurement the working electrode gets exposed to air, moisture or vacuum of necessity due to the different measuring methods. This may cause changes in the properties and surface appearance of the analysed electrode. Therefore *in situ* measurements are beneficial to investigate electrode processes while the electrochemical reactions occur. Especially *in situ* Raman measurements provide important information about the molecular and microscopic level of the electrode surface including the solution interface where the electrochemical happenings appear. Other *in situ* measuring techniques include for example UV-visible (UV-vis) and infra-red (IR) spectroscopy. [17]

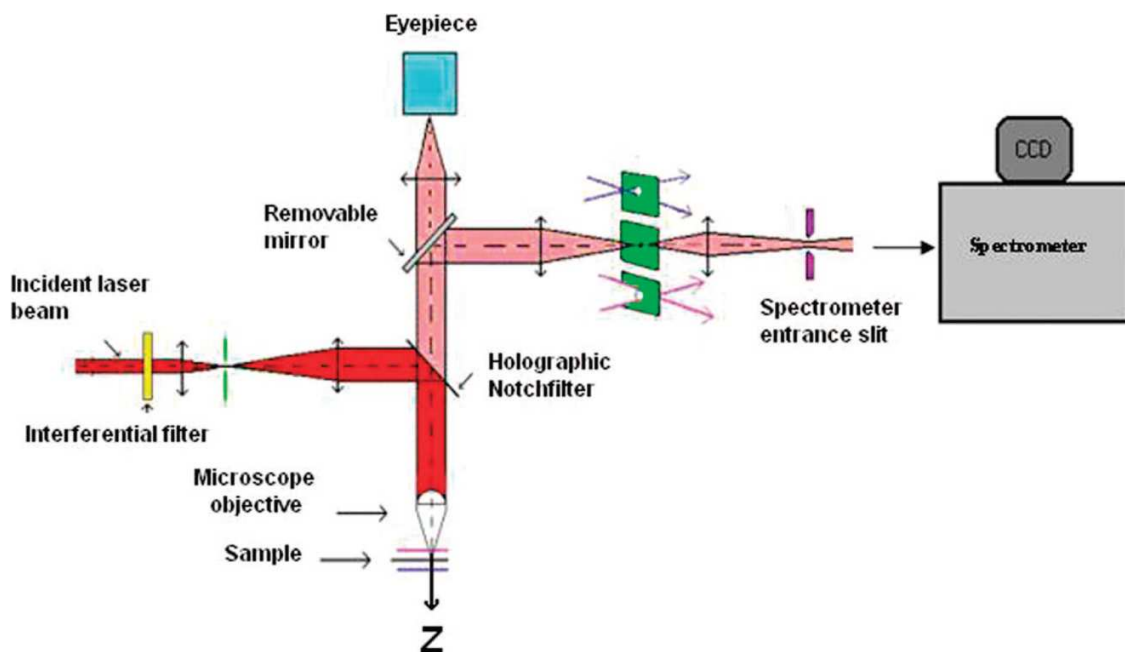


Figure 24: Schematic sketch of a confocal Raman microspectrometer system [61]

2.4.2.2 *Solid State Nuclear Magnetic Resonance (SSNMR)*

Nuclear magnetic resonance (NMR) measurements of liquid samples are popular since the mid 1960s. It is well known for studies of molecular structures, thanks to the characteristically so called *chemical shift* of the resonance frequency of an atom, which is highly dependent on the chemical environment. The problem with solid samples was their anisotropic nuclear interactions averaged by molecular motion, due to their dependence on molecular orientation. In liquids there exist a good mobility of the molecules and therefore are able to reorient very quickly. In solids this motions is hampered which causes broad humps instead of sharp spectral lines and the chemical information is therefore lost. [76]

Two major investigations helped to improve solid state NMR measurements: the oriented-sample solid state NMR spectroscopy, which leads to single-crystal-like spectra with a high resolution and the magic-angle-spinning (MAS) measurements, which averages the anisotropic interactions to first order by using so-called recoupling techniques. Since the 1989s solid state NMR techniques became more and more familiar and nowadays it is widely used in the field of material chemistry. [77, 78]

2.4.2.3 *Scanning Electron Microscope (SEM)*

When an electron beam is focused on a sample the electrons can be elastically or inelastically scattered. Depending on the energy of the detected electrons there is a distinction drawn between secondary electrons (SE), backscattered electrons (BE) and Auger electrons (AE). Secondary electrons have the lowest energy most likely about 2-5 eV in comparison to backscattered and Auger electrons, which possess an energy higher than 50 eV, see Figure 25. [79]

Secondary electrons arise from an exit depth of about only 0.5-10 nm and are mostly used for topographical and morphological imaging due to the dependence of the intensity of secondary electrons to the angle of incidence. In contrast to auger electrons are secondary electrons not characteristic to the composition of the surface layer. [80-82]

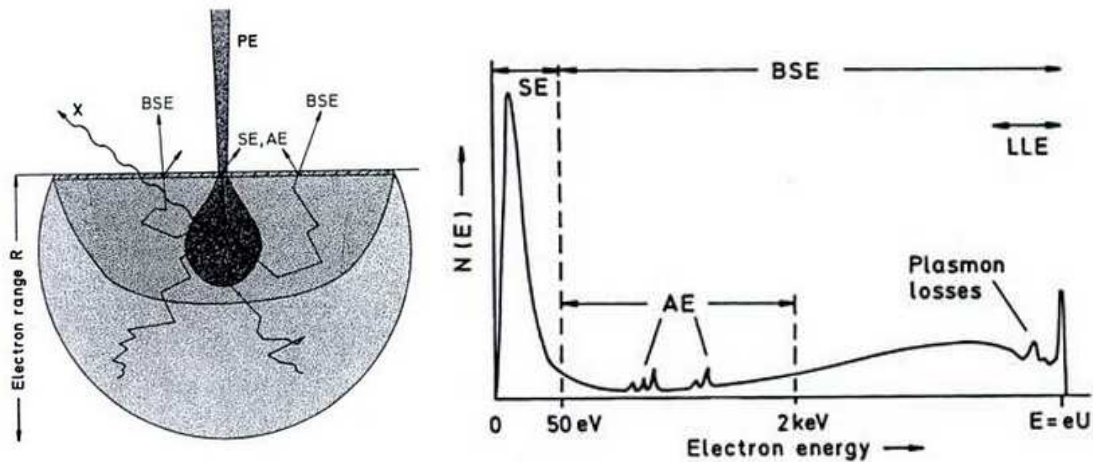


Figure 25: Left: Excitation area of secondary electrons (SE), back scattered electrons (BE), Auger electrons (AE) and X-ray quanta (x) after an exposure of the sample with primary electrons (PE). Right: Schematic energy spectrum of the different electrons. [79]

2.4.2.4 X-ray diffraction (XRD)

One big advantage of X-ray analysis is its non-destructive behaviour. X-rays can be used for example to study bulk structures of materials by X-ray diffraction (XRD), to identify different elements or material defects within a sample via the ability for X-ray transmission or absorption and for the qualitative and quantitative analysis of elements by X-ray fluorescence (XRF) measurements. [83]

The principal of the XRD measurement is the diffraction of X-rays by the lattice planes of a crystal in a characteristic angle, whereat the intensity of the scattered rays is a function of the positions of the atoms. By measuring different sets of planes it leads to a unique pattern which helps to identify the crystal structure of the sample. [84]

When high energy electrons impinge at a target material like copper it produces X-rays with a characteristic energy for the target material and secondary a continuous spectrum of X-rays, caused by the deceleration of the electrons. With the help of a monochromator the characteristic X-rays can get separated from the undesirable continuous spectrum, which is also known as *Bremsstrahlung*. Afterwards the characteristic X-rays get focused on the sample and if the wavelengths of the X-rays are in the order of the lattice spacing they get elastically diffracted. Elastically scattered X-rays can interfere destructive or constructive according to the Bragg's law, see Equation 27. The variable n stands for an

integer, λ is the wavelength of the incident wave, d is the spacing between the planes in the atomic lattice and θ is the angle between the incident rays and the scattering plane also seen in Figure 26. [83-85]

Equation 27: Bragg's law [85]

$$n\lambda = 2d \sin \theta$$

n ... integer, λ ... wavelength of incident wave, d ... spacing between the planes in the atomic lattice, θ ... angle between the incident rays and the scattering plane

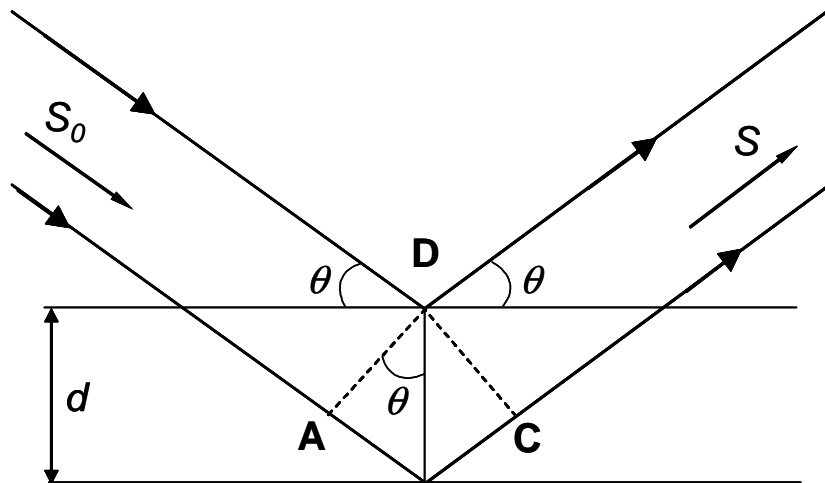


Figure 26: Reflection of X-rays against lattice planes according to Bragg, redrawn from [86]

3 Experimental

3.1 Battery Cell Types

3.1.1 Coin Cell

For three electrode measurements were used an ECC-Ref test cell from EL-Cell GmbH in Germany. The current collectors are made of stainless steel and polyether ether ketone (PEEK) an organic polymer thermoplastic, which has excellent mechanical and chemical resistance properties. In Figure 27 is shown an assembled and disassembled coin cell. The spring is gold plated to provide a perfect current transfer and the piston is made of corrosion resistant titanium. This cell has an inlay diameter of 18 mm and allows a sandwich geometry with a concentricity better than 0.1 mm. Thanks to the spring a homogeneous mechanical pressure lays on the electrodes. Other benefits are its small defined electrolyte volume down to 0.1 mL, due to minimized dead volume and its low He leakage rate $<10E^{-8}$ std cm^3/s owing to PE washers used for sealing off the cell. A sketch of an assembled coin cell is shown left in Figure 28. To insert the lithium reference electrode a special instrument has to be used, which is similar to a syringe. A photo of this instrument can be seen in Figure 28 on the right side. [87]



Figure 27: Assembled (left) and disassembled (right) coin cell

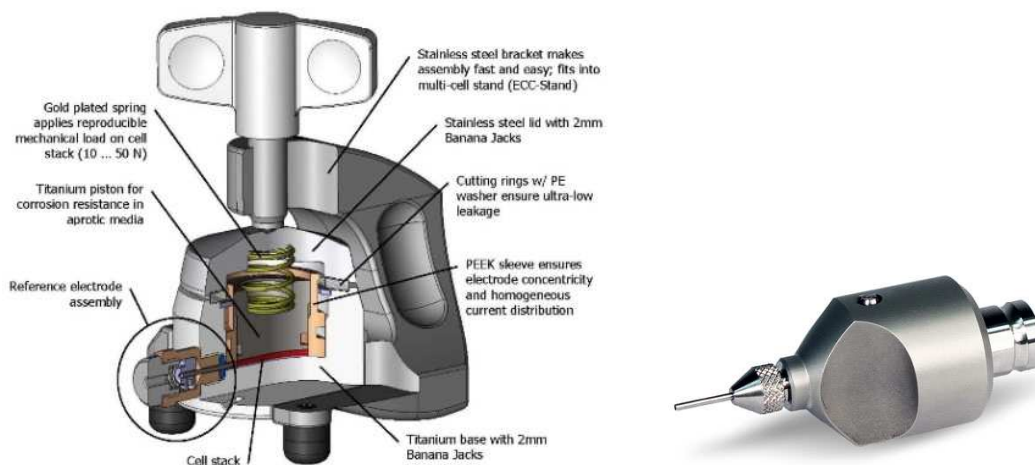


Figure 28: Sketch of an assembled coin cell (left) and instrument for lithium reference electrode insertion (right) [87]

3.1.2 Swagelok Cell

Swagelok cells are used for two electrode measurements, shown in Figure 29. In this case the electrodes are stacked inside the middle tube separated through a separator and pressed together via two spring loaded stainless steel current collectors. The counter electrode also acts as reference electrode.



Figure 29: Assembled (left, above), disassembled (left, below) and connected (right) Swagelok cell

3.1.3 *In situ* Raman Cell

In situ Raman cells must fulfil several essential aspects. It must provide a good electronic contact between the electrodes while preventing short circuits and it must be sealed up from air and moisture for a usual measurement period. Furthermore it must be possible to focus a laser on the electrode in a way that it must not pass through a thick layer of electrolyte usually causing a lot of undesired signal noise. Other beneficial aspects are an easy assembling and a high cell-flexibility for investigations of different systems.

Sketches of the two electrodes *in situ* Raman cell are shown in Figure 30. A and B outline the assembled *in situ* Raman cell while C shows the enlarged area, which is marked in A with a black circle, where the components are separated and drawn in an expanded scale. The body of the *in situ* Raman cell is made of an organic thermoplastic polymer polyether ether ketone (PEEK) with excellent mechanical and chemical resistance. For a good electrochemical contact the cell includes two electrical copper contacts for the working electrode and a spring loaded contact for the counter electrode including an adjustable screw. A titanium coin is used as a current collector for the counter electrode. To provide a small vertical movement freedom to be able to press the electrodes together and to seal up the cell an O-ring, made of ethylene propylene diene monomer (EPDM), is put around the current collector. On this current collector the counter electrode is placed, which is covered with a usual filter paper, acting as a separator. On this separator the free standing working electrode is placed, which gets covered with an aluminium or copper foil dish used as current collector for the working electrode. This current collector has a small hole in the middle (diameter ca. 1mm) through which the laser can be later focused on the electrode surface. Finally a thin optical glass window (0.15 mm thick) is placed on the current collector which seals up the cell with the help of another O-ring placed around the whole stack of electrodes. After closing the cell by screwing the cell cover on top the electrodes can be pressed together by screwing the adjustable screw of the counter electrode a little bit more into the cell. This has to be made very carefully to avoid breaking the glass window at the other side of the cell.

In Figure 31 an image of the assembled (left) and disassembled *in situ* Raman cell (right) is shown. Figure 32 shows the step by step assembling process of the cell. With this kind of assembling of the *in situ* Raman cell it is possible to focus the laser at the backside of

the working electrode. Therefore the laser has to pass through the optical glass window and a thin layer of electrolyte, covering the electrode.

The whole cell was cleaned with distilled water and acetone and dried in an oven at ca. 80°C under air atmosphere. Afterwards it was directly transferred into an argon filled glove box, where it is assembled and sealed up for the measurement. After assembling the open circuit potential was measured to check against short circuit.

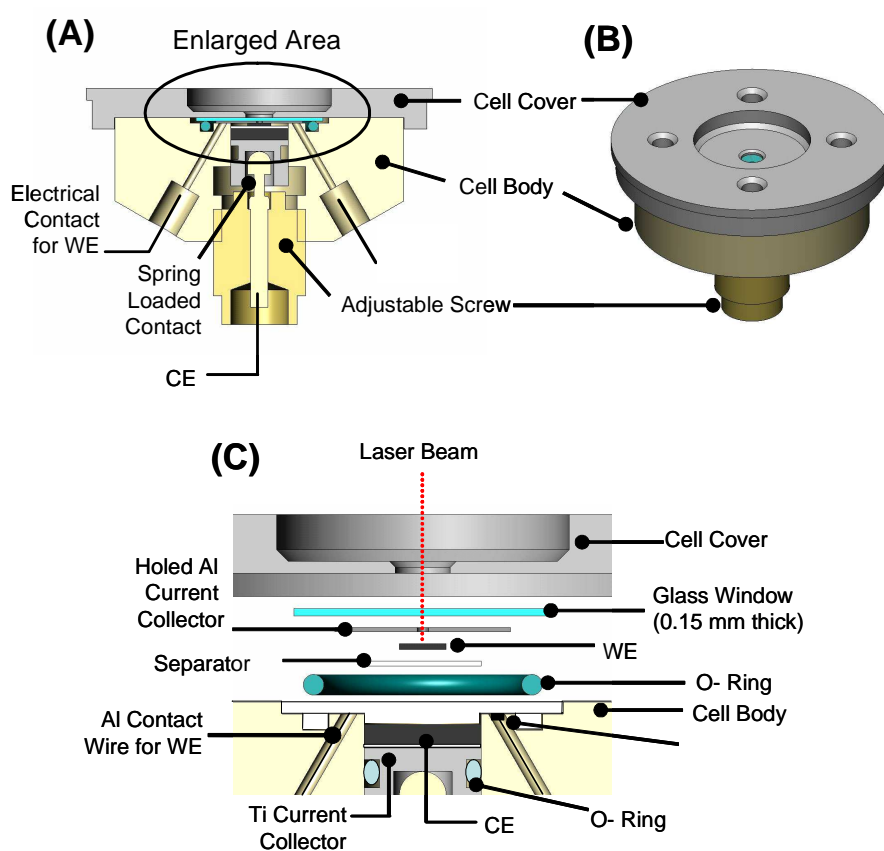


Figure 30: Two electrode *in situ* Raman cell in (A) the fully assembled stage, (B) three-dimensional perspective and (C) an enlarged area showing the separate components (expanded, not to scale) [88].

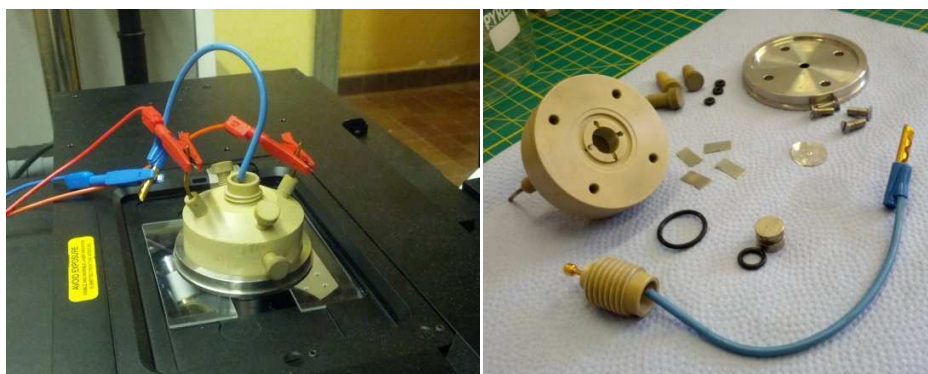


Figure 31: Assembled (left) and disassembled (right) *in situ* Raman cell



Figure 32: Assembling of the *in situ* Raman cell from left to right

3.2 Synthesis of V_2O_5 Nanowires

0.365 g of the commercial powder V_2O_5 (Sigma-Aldrich, < 99.99 % trace metal basis,) were vigorously mixed with 30 mL Milli-Q water on a stirrer plate with the help of a magnetic stir bar. Then 5 mL 30 % H_2O_2 (ACS reagent contains inhibitor, Sigma Aldrich) was added and the solution was vigorously stirred for 20 minutes. The red/orange clear solution was transferred into a stainless steel digestion bomb (Model 4744 General Purpose Acid Digestion Vessel, 45 mL, Parr Instrument Company) with a polytetrafluoroethylene (PTFE) 45 mL inlay and put into an oven of about 205°C for 4 days. This resulted in an orange/yellow precipitate suspended in a yellow clear solution. The product was then washed several times with water and ethanol. Afterwards it was dried in a vacuum oven at 80°C overnight for about 16 hours. During this dehydration the colour changed from yellow/orange to yellow/green. The last step of this synthesis was a calcination process in air at 400°C for 1 h and 20 min. In the meantime the colour

changed back from yellow/green to yellow/orange, see Figure 33. The occurred weight loss was thereby 3.54 %. From the synthesis 0.338 g of V_2O_5 nanowires was produced, which was a yield of 92.7 %.

All together this V_2O_5 nanowire production was repeated four times with slightly different amounts of initial weights, see Table 2. For the second, third and fourth time the quantity was reduced by one-fifth, to ensure not to damage the digestion bomb, because the total amount of solution inside should be less than 30 mL for a 45 mL inlay.

To be able to prepare an electrode on a current collector the active material was broken up with a pestle and mortar to get a powder.



Figure 33: V_2O_5 nanowires (3rd synthesis)

Table 2: Synthesis of V_2O_5 nanowires – initial weights

Synthesis	V_2O_5 [g]	Milli-Q H_2O [mL]	H_2O_2 [mL]	Total amount of solution [mL]	Nanowires [g]	Yield [%]
1.	0.365	30	5	35	0.338	92.7
2.	0.291	24	4	28	0.263	90.4
3.	0.312	24	4	28	0.288	92.2
4.	0.308	24	4	28	0.298	97.0

3.3 Preparation of Electrodes

3.3.1 Electrodes for Coin Cells and Swagelok Cells

Different active materials, such as LiMn_2O_4 (Sigma-Aldrich, Lithium manganese(III, IV)oxide, electrochemical grade), TiO_2 (Titanium dioxide HOMBITAN, S141 835614010), V_2O_5 (Sigma-Aldrich, < 99.99 % trace metal basis) and $\text{Li}_4\text{Ti}_5\text{O}_{12}$ (HOMBITEC LTO5), black carbon (Super C65 – TIMCAL, C.ENERGY™) as a conductive additive and the binder Polyvinylidene Fluoride (PVdF – Sigma-Aldrich, 182702-250G, Average $M_w \sim 534.000$ by GPC, powder) were weighed into a small glass bottle in various ratios such as 60/20/20 or 70/15/15 of mass%. Afterwards the organic solvent N-Methyl-2-Pyrrolidone (NMP – Sigma-Aldrich, anhydrous, 99.5%) was added until a viscous slurry occurred via stirring. Additionally an ultrasonic cleaner was used three times for about 5 minutes to break all agglomerates and to get a smooth slurry.

The obtained slurry was coated onto the designated current collector (copper, aluminium or stainless steel) with a preferred thickness (20-50 μm) by a doctor blade and then dried in an oven under atmosphere at 80°C , see left in Figure 34.

Finally the required size of the electrode was stamped out with a hammer and a metal sand rammer, see Figure 29 right. To remove water adsorption on the surface the electrodes was finally dried overnight in a vacuum oven at 120°C in the glove box.



Figure 34: Casted TiO_2 electrode on copper and metal slider (left) and metal sand rammer (right) [89]

3.3.2 Electrodes for *in situ* Raman Cell

3.3.2.1 *Free Standing Electrodes*

For *in situ* Raman cell measurements a free standing electrode is required. This can be put in the middle of the separator and covered with the current collector. To get such a free standing electrode an electrode slurry (made of an active material, carbon black, binder and solvent) with a high binder concentration gets casted on a flat glass plate. After drying for a couple of hours in an oven at ca. 80°C the electrode was then peeled off the glass with the aid of a plastic scraper. This method leads to a free standing electrode film, which can be cut into small electrode pieces. The actual active material in those electrodes can be determined by weighing and subsequently relating the value to the concentration of active material in the used slurry.

3.3.2.2 *Electrodes coated on a Filter Paper*

Another method to get a usable *in situ* Raman electrode is to put a few drops of electrode slurry directly on a filter paper in the size of a separator. Afterwards the filter paper gets completely dried in a vacuum oven and subsequently weighted. The actual mass of active material can again be calculated by relating the mass to the concentration of active material in the used slurry. Benefits of this preparation method are the possibility of using less binder, which means more active material and therefore less noise signal, and the easy and time saving fabrication.

In case of the V₂O₅ nanowires the active material gets directly weighted on a separator and afterwards covered with drops of a slurry, consisting of solvent, carbon black and a bit of binder. After drying in a vacuum oven for a couple of hours these covered filter papers can be used as a standard electrode.

3.4 Preparation of Electrolytes

3.4.1 EC/DMC with LiClO₄

2.128 g of LiClO₄ (Sigma-Aldrich, battery grade, dry, 99.99% trace metal basis) was dissolved in 10 mL dimethyl carbonate (DMC, Sigma-Aldrich, anhydrous, ≥99%). Ethylene carbonate (EC, Sigma-Aldrich, anhydrous, 99%) was heated to 50°C until it was solvent and afterwards 10 mL of it were added to the other solution and mixed until a clear transparent solution occurred. In the end an electrolyte of EC and DMC with a volume ratio of 1:1 with 1 M LiClO₄ was produced.

3.4.2 EC/DMC with LiPF₆

1.5196 g of LiPF₆ (Sigma-Aldrich, battery grade, dry, ≥99.99% trace metal basis) was dissolved in 5 mL dimethyl carbonate (DMC). Afterwards 5 mL of warm liquid ethylene carbonate (EC) were added and mixed until an unclear, slightly orange solution occurred. This resulted in an electrolyte of EC and DMC consisting of a volume ratio of 1:1 with 1 M of the salt LiPF₆ in solution.

3.4.3 ([EMIm]Cl) with AlCl₃

10.016 g of the solid AlCl₃ (Sigma-Aldrich, anhydrous 99.99%) were added to 9.996 g of the solid 1-ethyl-3-methylimidazolium chloride ([EMIm]Cl) (Sigma Aldrich, ≥ 98%, ≤ 300 ppm H₂O). During a strong exothermic reaction an orange clear ionic liquid was produced, which has a low viscosity at room temperature.

3.4.4 Aqueous AlCl₃

1.339 g of AlCl₃ was slowly added to 10 mL of Milli-Q water while the vial was hold by a labour cramp over an ice bath. It was, as expected, a very strong exothermic reaction, but finally a solution of 1 M AlCl₃ in water was produced.

3.5 Equipment properties

3.5.1 Raman Instrumentation

All Raman spectra were collected with a confocal inVia Raman microscope from Renishaw. The spectra were measured at room temperature ($\sim 22^\circ\text{C}$) using a Renishaw RL633 HeNe laser with a wavelength of 633 nm, a nominal laser power of 12.5 – 17 mW CW. A wide angle 50x objective (from Olympus) was used to focus the laser onto the electrode surface without touching the glass window. As band calibration was used a silicon surface with a very precise signal peak at a Raman shift of 520 cm^{-1} .

A movable X-Y-Z computer controlled stage, a closed circuit television camera (CCTV) and a mercury-vapour white light lamp allowed focusing the laser on the electrode surface and moving it over the surface in order to find a perfect measuring spot with the strongest Raman signal. With the help of the video camera it was also possible to take pictures of the electrode surface while looking with bright field at the surface.

As detector was used a charge coupled device (CCD) camera, for more information see also Chapter 2.4.2.1.

3.5.2 Potentiostat Instrumentation

For battery testing measurements was used a five channel Ultimate Electrochemical Workstation (VSP – Modular 5 Channels Potentiostat/Galvanostat/EIS) from BioLogic. Additionally an Electrochemical Impedance Spectroscopy (EIS) analyser (10 μHz to 1 MHz) was included. For *in situ* Raman measurements a BioLogic SP-150 was used.

Both potentiostats ran with an EC-Lab[®] software package.

3.5.3 Solid State NMR Spectroscopy Instrumentation

The solid state NMR experiments (^{27}Al ($I = 5/2$) and ^{51}V ($I = 7/2$)) were carried out on a 9.4 T Bruker DSX 400 MHz spectrometer equipped with a Bruker 4 mm HXY probe (in double resonance mode) tuned to $\nu_0(^{27}\text{Al}) = 104.3\text{ MHz}$ for ^{27}Al or $\nu_0(^{51}\text{V}) = 105.2\text{ MHz}$ for ^{51}V . ^{27}Al NMR spectra were recorded with a rotor synchronized Hahn echo pulse sequence with one rotor period of evolution/refocusing to avoid probe ring down, while

^{51}V NMR spectra were simply recorded with a one pulse sequence. For ^{27}Al , a selective short pulse length $\pi/2 = 1 \mu\text{s}$ at a rf field of $\nu_1 = 83 \text{ kHz}$ was used at a recycle delay of 0.5 s, while for ^{51}V a selective short pulse length $\pi/2 = 0.75 \mu\text{s}$ at a rf field of $\nu_1 = 83 \text{ kHz}$ was used at a recycle delay of 5 s. All experiments were performed under MAS and the MAS frequencies are given in the figure captions. The ^{27}Al and ^{51}V chemical shifts were externally referenced to a 0.1 M solution of $\text{Al}(\text{NO}_3)_3$ in water at 0 ppm, and to a 0.16 M saturated solution of NaVO_3 in water at -574.4 ppm (corresponding to neat VOCl_3 at 0 ppm). [90]

3.5.4 Glove Box Instrumentation

The glove box was an Inert Lab 2 GB Glove Box System from the company IT – Innovative Technology, see Figure 35. It was a 304 Type SS Construction with an inert atmosphere of less than 0.1 ppm O_2 and less than 1 ppm H_2O . For the insertion of materials a small and a large chamber existed. The larger chamber included a heating system to be able to use it as a vacuum oven to dry materials before entering the glove box.



Figure 35: Glove box – Inert Lab 2 GB Glove Box System (IT – Innovative Technology)

4 Results and Discussion

4.1 V₂O₅ Nanowire Synthesis and Characterisation

The V₂O₅ nanowires, which were synthesized via a hydrothermal method as mentioned in 3.2, were analysed with the aid of an electron microscope and by X-ray diffraction (XRD) measurements. Furthermore the crushed V₂O₅ nanowires with pestle and mortar from the first synthesis and the commercial V₂O₅ powder, which was used as starting material, have been analyzed.

The scanning electron microscope (SEM) pictures of V₂O₅ nanowires (1st synthesis), the crushed nanowires and the commercial V₂O₅ powder are shown in Table 3. According to these SEM pictures in Table 3 the synthesis of V₂O₅ nanowires was successful. During the first synthesis the commercial V₂O₅ powder, which consists of up to 1 mm big agglomerates of powder, was transformed into less than 1 µm thick nanowires. Most of them are also longer than 1 cm. By crushing those nanowires with the help of a pestil and mortar the length of mostly all wires gets strongly reduced down to a couple of micrometers.

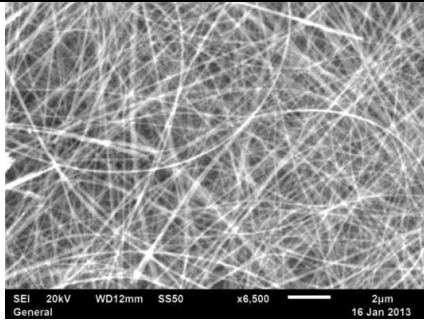
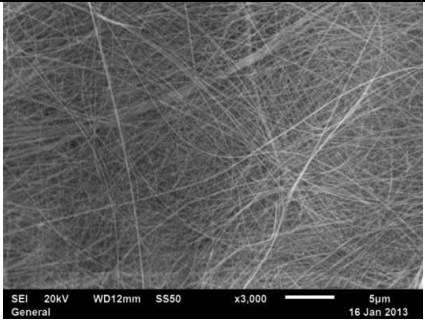
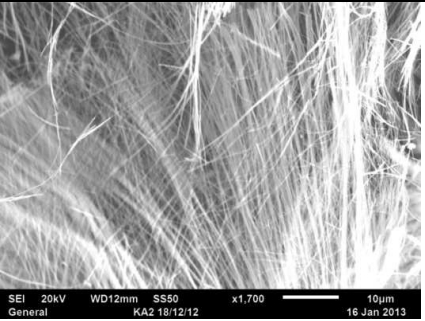
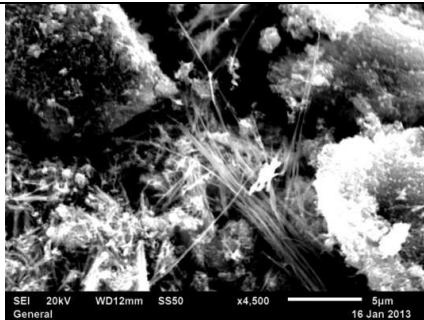
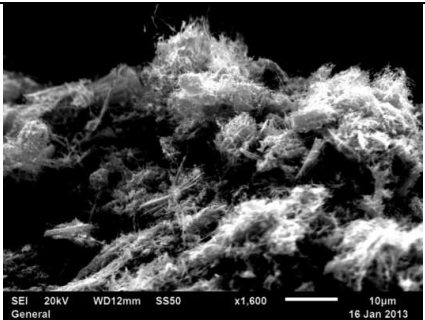
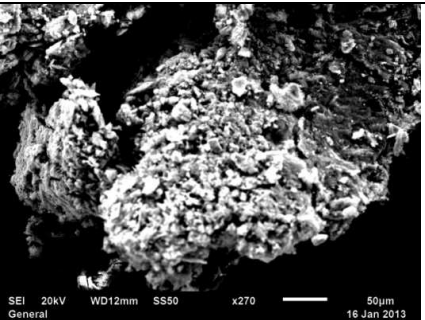
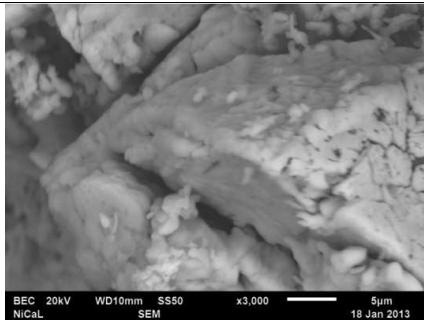
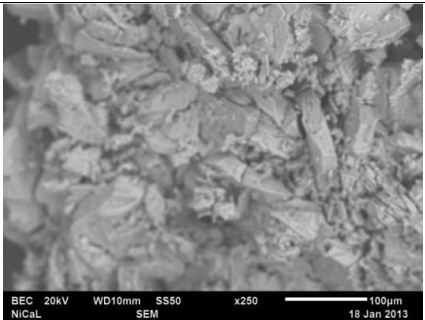
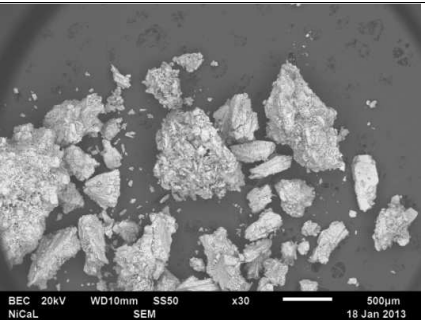
In Figure 36 are the different XRD data plotted against reference V₂O₅ data from the Inorganic Crystal Structure Database (ICSD) of FIZ Karlsruhe – Leibniz Institute for Information Infrastructure. The peak positions of the commercial powder compared to the database agree very well and also the intensity variations are similar to each other, but there is one additional big peak at around 38°, which should not be there. This big peak can also be seen in the spectrum of the first and second synthesised V₂O₅ nanowires. In the third and fourth synthesis product no such peak occurs. Apart from big intensity differences the spectrum of the first synthesis product resembles to the one of the commercial powder. By crushing the nanowires and shortening their lengths the intensities of the different peaks get back to the appearance of the commercial powder, which is very similar to the orthorhombic database data and therefore it could be an evidence for the orthorhombic crystal structure of the V₂O₅ nanowires. The XRD spectrum of the nanowires, produced during the second synthesis, does not differ a lot from the commercial powder, but the third and the fourth synthesis product have less clear peaks, because the intensities especially from 35° upwards are so little that their

peak positions can just be estimated. The peak at about 26° is always the one with the biggest intensity from all measured samples. This stands in contrast to the database where the peak with the biggest intensity is the one at about 20° .

Overall the synthesis of centimetre long V_2O_5 nanowires via a hydrothermal method according to a recent paper [91] was successful.

The used orthorhombic V_2O_5 data from the Inorganic Crystal Structure Database (ICSD) of FIZ Karlsruhe – Leibniz Institute for Information Infrastructure relates to “A refinement of the structure of V_2O_5 ”, Enjalbert, R.; Galy, J., *Acta Crystallographica C* (39,1983-) (1986) 42, p1467-p1469.

Table 3: SEM Pictures of V_2O_5 nanowires (first synthesis), crushed V_2O_5 nanowires (first synthesis) and the commercial V_2O_5 powder (Sigma Aldrich, < 99.99%)

V_2O_5 nanowires (1st Synthesis)		
Scale: 2 μm	Scale: 5 μm	Scale: 10 μm
		
Crushed V_2O_5 nanowires (1st Synthesis)		
Scale: 2 μm	Scale: 10 μm	Scale: 50 μm
		
V_2O_5 commercial powder (Sigma Aldrich, < 99.99%)		
Scale: 5 μm	Scale: 100 μm	Scale: 500 μm
		

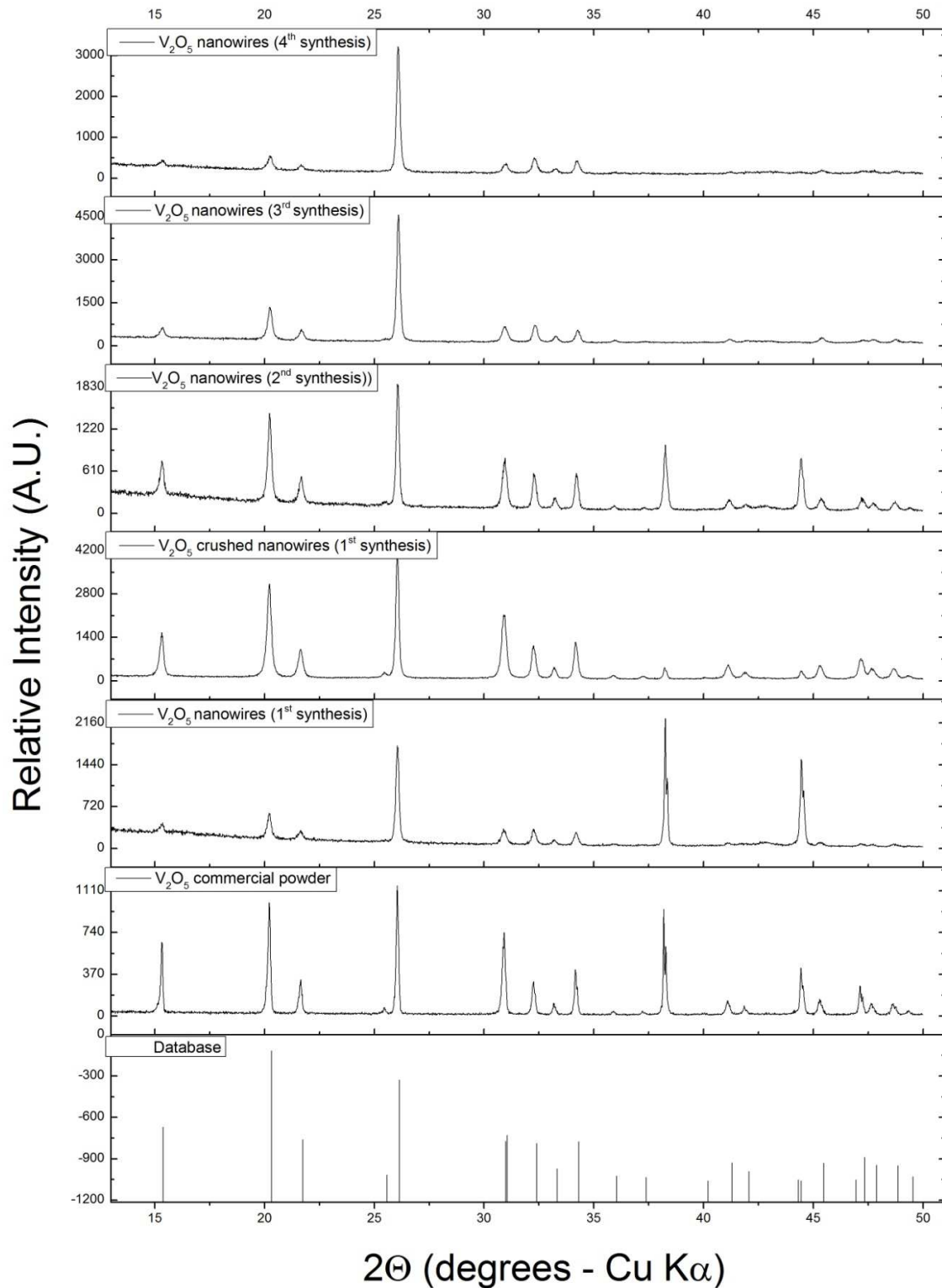


Figure 36: XRD measurements of V_2O_5 (commercial powder, nanowires (1st-4th synthesis), crushed nanowires (1st synthesis) compared to V_2O_5 XRD-data from a database

4.2 Aluminium Ion Battery

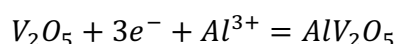
4.2.1 Ionic Liquid Electrolyte

4.2.1.1 Electrochemical Characterisation

- V_2O_5

According to recent investigations [67] the intercalation of aluminium ions into V_2O_5 nanowires using an ionic liquid as electrolyte should be possible. Therefore investigations were undertaken first of all to verify this statement but also in case of success to improve this new kind of battery system. The chemical reaction equation for this intercalation is shown in Equation 28.

Equation 28: Reaction equation for aluminium intercalation into V_2O_5



In Figure 37 a potentiostatically cycled measurement of V_2O_5 nanowires on a stainless steel current collector (60 wt. % V_2O_5 nanowires from 1st synthesis, 20 wt. % Super C65, 20 wt. % PVdF, prepared in NMP) and an aluminium counter electrode is shown. The electrode was cut out with the aid of a scissor and hence it was not possible to calculate the exact amount of active material of the electrode, due to too inaccurate current collector weight estimations. Therefore all CV measurements are plotted against the current I (mA) instead of the current density (mA/g). The electrolyte was 1-ethyl-3-methylimidazolium chloride ([EMIm]Cl) with $AlCl_3$. The measurement was run with a scan rate of 0.2 mV/s and was cycled down to 0 V and back up to 2.4 V. Unfortunately corrosion processes from about 1.5 V above were observed leading to extremely high current values, which are not completely shown in Figure 37. Nevertheless there exists a small cathodic peak at around 0.4 V which could be likely the intercalation of aluminium into the V_2O_5 nanowires. An anodic peak at about 0.8 V hypothesises the reversible reaction of the intercalation process. Another big anodic peak around 1.1 V shows that something else undesirable is happening. By reducing the anodic potential limit to 1.0 V it is possible to cycle the battery potentiostatically without corrosion processes occurring,

see Figure 38. During the first eight cycles the cathodic peak at around 0.4 V moves towards 0.35 V and another peak with 0.1 V less than the other occurs. At the anodic side two peaks at around 0.8 V and 0.9 V shift during the first cycles towards higher voltages. In Figure 39 a cyclic voltammetry of V_2O_5 (commercial powder) on a stainless steel current collector (60 wt. % V_2O_5 , 20 wt. % Super C65, 20 wt. % PVdF, prepared in NMP) is shown. As counter electrode was used an aluminium foil and [EMIm]Cl was used as electrolyte. The scan rate in Figure 39 was 0.2 mV/s and the potential limits 0 V and 1.4 V. During the first cycle a small cathodic peak at around 0.3 V occurred. From 1 V upwards a big peak came about at 1.2 V. After cycling down again a huge cathodic peak at 0.35 V happened, which presumably caused the following big anodic peak at 0.9 V. During the second anodic cycle corrosion processes occurred from 1.2 V upwards. In Figure 40 was the anodic limit reduced to 1 V, which enabled to cycle the battery a couple of times without high current peaks coming up. During the first cycle one broad cathodic peak at 0.1 V and two very small anodic peaks at 0.4 V and 0.6 V occurred. During the second cycle the cathodic peak at 0.1 V got broader and an anodic peak at 0.55 V occurred. From the third cycle on a cathodic peak at 0.4 V and an anodic peak at 0.75 V increased with each cycle while the two peaks from the first two cycles almost vanished completely. In Figure 41 the same cell was cycled a second time with the same parameters. The first cycle again did not show any cathodic peaks but one anodic peak around 0.8 V, which causes from the second cycle on a cathodic peak at 0.45 V, which shifted towards 0.5 V. The anodic peak at 0.8 V shifted towards 0.85 V, while another anodic peak at 0.7 V occurred during the second cycle.

According to the recent paper about a working aluminium ion battery [67] the reversible intercalation of aluminium into V_2O_5 nanowires should cause a cathodic peak at 0.4 V and an anodic peak at 0.8 V. In contrast to the undertaken measurements those peaks should be stable also after 20 cycles and furthermore no other peaks and no corrosion processes occur while cycling the battery anodically up to 2.4 V. It was not possible to gain the same results and therefore it was impossible to produce a stable reversible aluminium ion battery with an electrode made of V_2O_5 nanowires using the ionic liquid [EMIm]Cl as electrolyte.

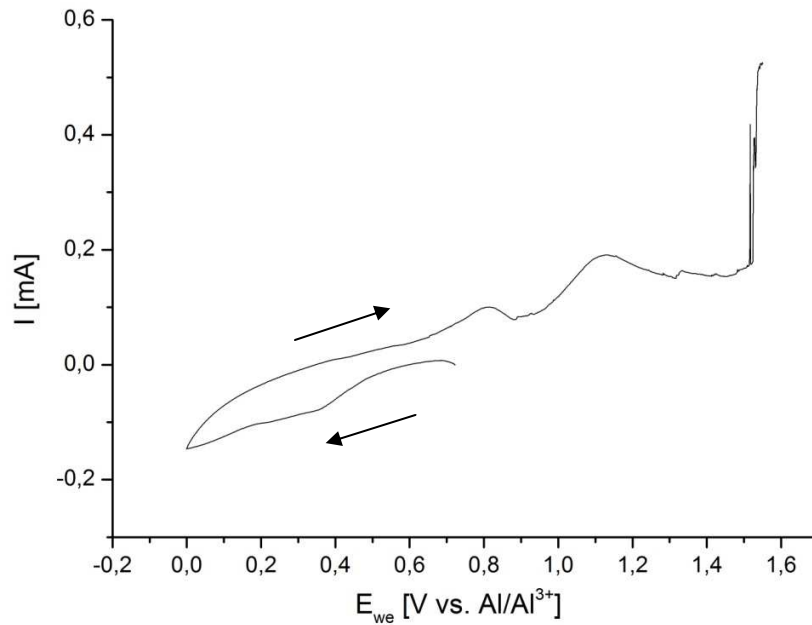


Figure 37: Swagelok cell - Potentiostatic cycling (0.2 mV/s) of V₂O₅ nanowires on stainless steel current collector (60 wt. % V₂O₅ nanowires from 1st synthesis, 20 wt. % Super C65, 20 wt. % PVdF, prepared in NMP) with aluminium counter electrode and ([EMIm]Cl) electrolyte; 0.0 V – 2.4 V

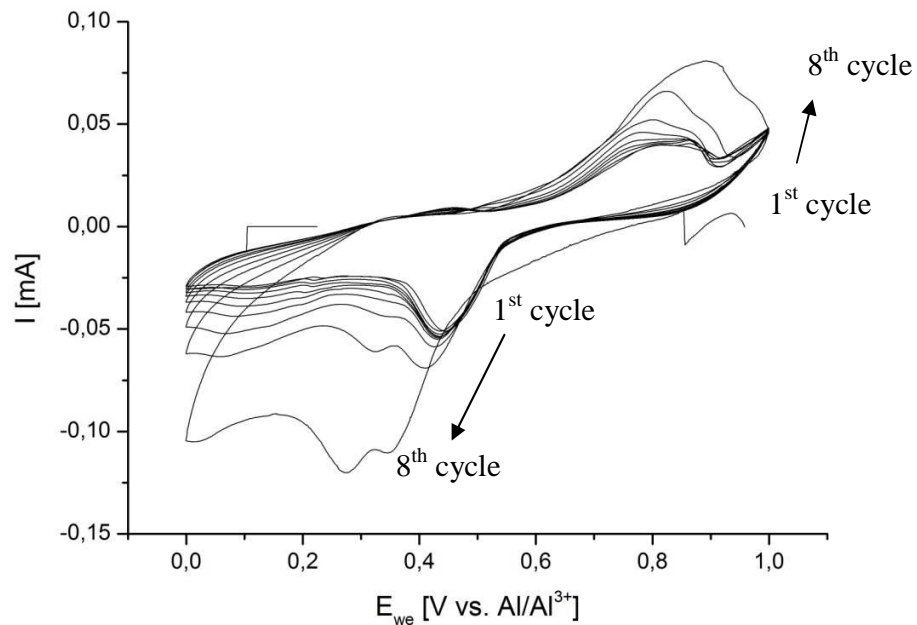


Figure 38: Swagelok cell - Potentiostatic cycling (0.2 mV/s) of V₂O₅ nanowires on stainless steel current collector (60 wt. % V₂O₅ nanowires from 1st synthesis, 20 wt. % Super C65, 20 wt. % PVdF, prepared in NMP) with aluminium counter electrode and ([EMIm]Cl) electrolyte; 0.0 V – 1.0 V

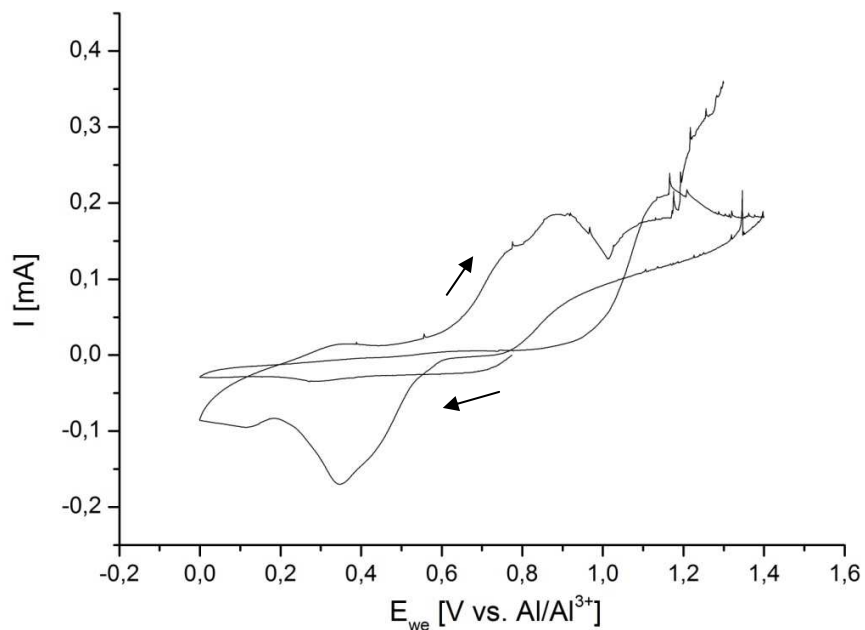


Figure 39: Swagelok cell - Potentiostatic cycling (0.2 mV/s) of V_2O_5 commercial powder on stainless steel current collector (60 wt. % V_2O_5 , 20 wt. % Super C65, 20 wt. % PVdF, prepared in NMP) with aluminium counter electrode and ([EMIm]Cl) electrolyte; 0.0 V – 1.4 V

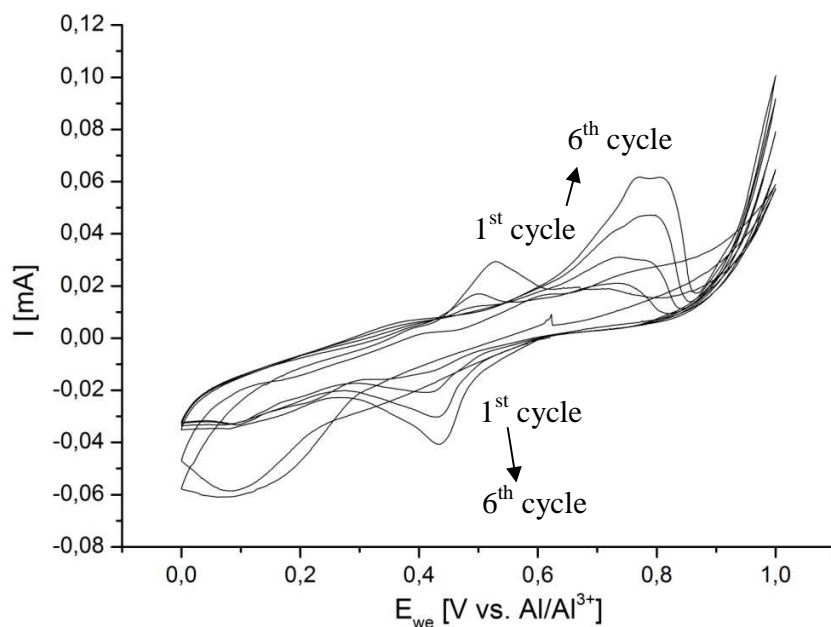


Figure 40: Swagelok cell - Potentiostatic cycling (0.2 mV/s) of V_2O_5 commercial powder on stainless steel current collector (60 wt. % V_2O_5 , 20 wt. % Super C65, 20 wt. % PVdF, prepared in NMP) with aluminium counter electrode and ([EMIm]Cl) electrolyte; 0.0 V – 1.0 V, First run: 1st-6th cycle

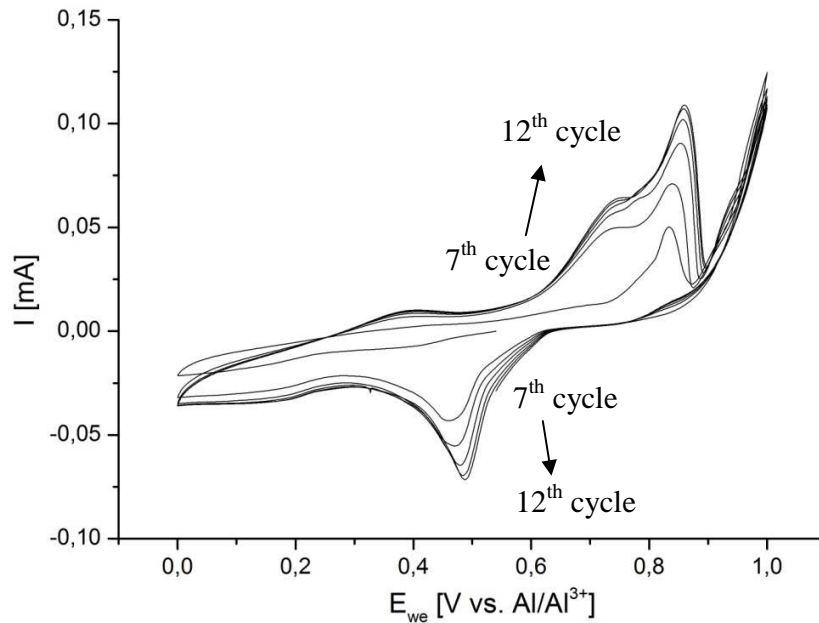


Figure 41: Swagelok cell - Potentiostatic cycling (0.2 mV/s) of V_2O_5 commercial powder on stainless steel current collector (60 wt. % V_2O_5 , 20 wt. % Super C65, 20 wt. % PVdF, prepared in NMP) with aluminium counter electrode and ([EMIm]Cl) electrolyte; 0.0 V – 1.0 V; Second run: 7th-12th cycle

- $LiMn_2O_4$

Additionally to the V_2O_5 electrodes were taken measurements with working electrodes made of $LiMn_2O_4$, see Figure 43 - Figure 46, within an aluminium battery (counter electrode: aluminium foil, electrolyte: [EMIm]Cl). But before trying to intercalate aluminium into $LiMn_2O_4$ the electrode material must get delithiated. With a potential of about 4 V (vs. Li/Li^+) it is possible to de-lithiate to a content of $Li_{0.015}Mn_2O_4$, also called termed λ - MnO_2 [61], also see Chapter 4.3.1.2. This happened with a lithium metal counter electrode and an electrolyte made of 1:1 EC:DMC with 1 M of $LiClO_4$. The cell was swept to 4.4 V with 0,150 mA/h, see Figure 42. The potential was hold for 15h till the current was nearly 0 and then the whole cell was transferred into the glove box, the working electrode washed with pure DMC and dried at room temperature for about an hour. Then the working electrode was stacked in an aluminium battery.

Figure 43 shows the first potentiostatic cycle of the delithiated $LiMn_2O_4$ working electrode (59 wt. % $LiMn_2O_4$, 21 wt. % Super C65, 20 wt. % PVdF, prepared in NMP) on a stainless steel current collector in an aluminium battery using the ionic liquid [EMIm]Cl

including AlCl_3 as electrolyte. The potential limits were set to 0.8 V and 2.4 V. There occurred two cathodic peaks at 1.9 V and 1.1 V. On the anodic side there are also two peaks, which are at 1.5 V and 2.2 V. If the two cathodic peaks are really the intercalation of aluminium into LiMn_2O_4 something additionally is happening at the anodic side, because of the higher current over the whole anodic scan compared to the cathodic one. The same electrode was cycled another time with the same parameters, see Figure 44. During the second cycle one big anodic peak at 1.4 V occurred, which did not appear anymore within the 3rd and the 4th cycle. The other anodic peak at 2.2 V shifted during the next two cycles towards 1.9 V. In all those cycles no cathodic peaks are observed anymore. This means that there is no reversible aluminium intercalation into LiMn_2O_4 and that something else, usually undesirable, is happening at the anodic side.

In Figure 45 is shown a slower potentiostatically measurement with 0.01 mV/s and a smaller voltage window from 1.5 – 2.4 V. During the first cycle appeared one big cathodic peak again at 2.1 V, which could be likely the intercalation of aluminium into LiMn_2O_4 , but because of no anodic peaks, also not in the second cycle see Figure 46, this intercalation appears to be irreversible.

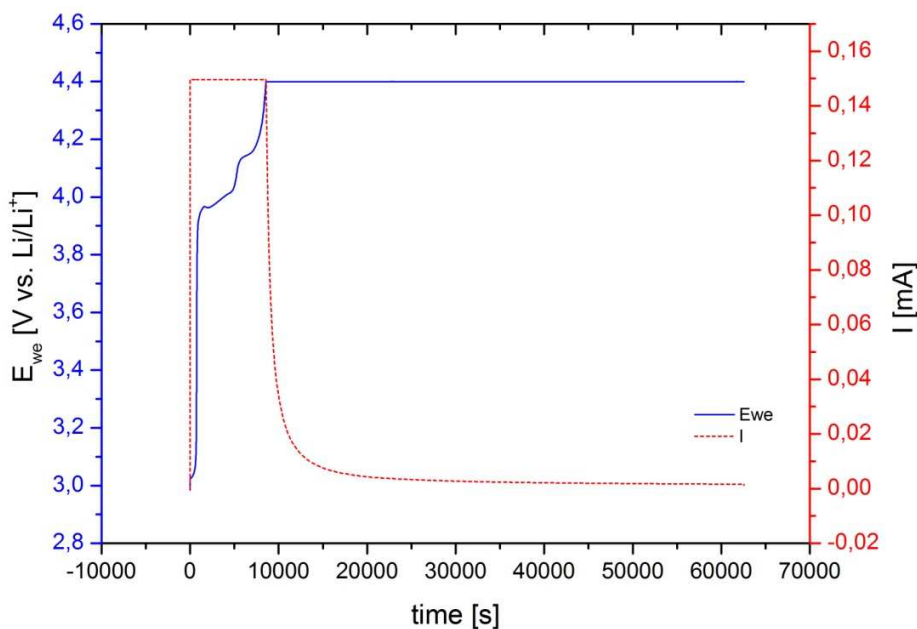


Figure 42: Coin cell - Delithiation of LiMn_2O_4 on stainless steel current collector (59 wt. % LiMn_2O_4 , 21 wt. % Super C65, 20 wt. % PVdF, prepared in NMP) with lithium metal counter electrode and 1:1 EC:DMC electrolyte with 1 M LiClO_4 , galvanostatic sweep to 4.4 V with 0.150 mA/h, hold 4.4 V for 15 h

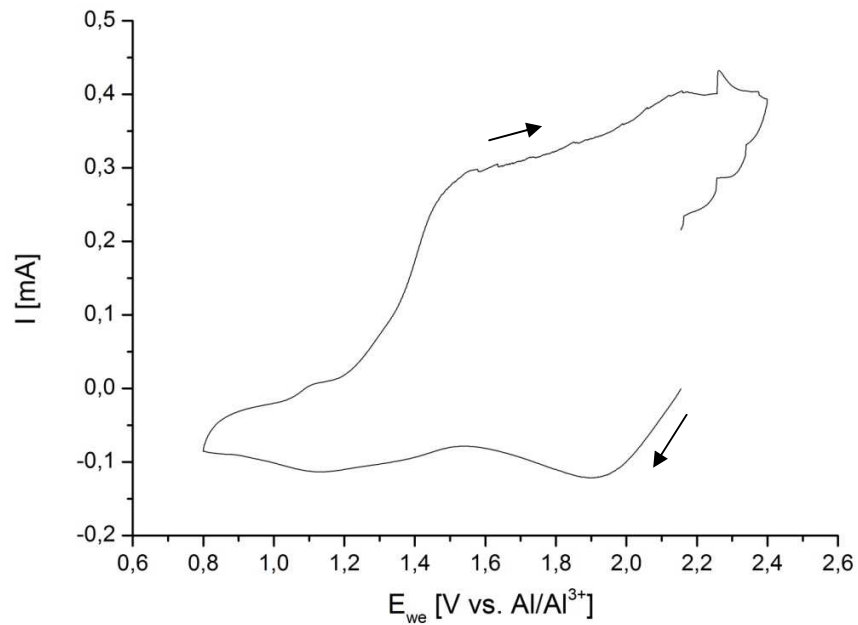


Figure 43: Coin cell - Potentiostatic cycling (0.2 mV/s) of LiMn_2O_4 on stainless steel current collector (59 wt. % LiMn_2O_4 , 21 wt. % Super C65, 20 wt. % PVdF, prepared in NMP) with aluminium counter electrode and $(\text{EMIm})\text{Cl}$ electrolyte; 0.8 V – 2.4 V; First run: 1st

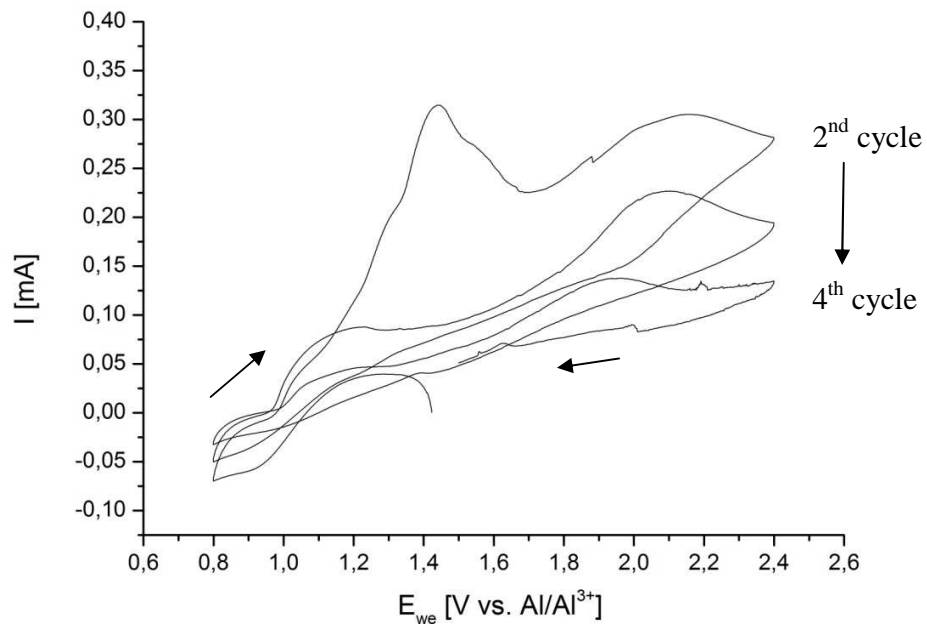


Figure 44: Coin cell - Potentiostatic cycling (0.2 mV/s) of LiMn_2O_4 on stainless steel current collector (59 wt. % LiMn_2O_4 , 21 wt. % Super C65, 20 wt. % PVdF, prepared in NMP) with aluminium counter electrode and $(\text{EMIm})\text{Cl}$ electrolyte; 0.8 V – 2.4 V; Second run: 2nd – 4th

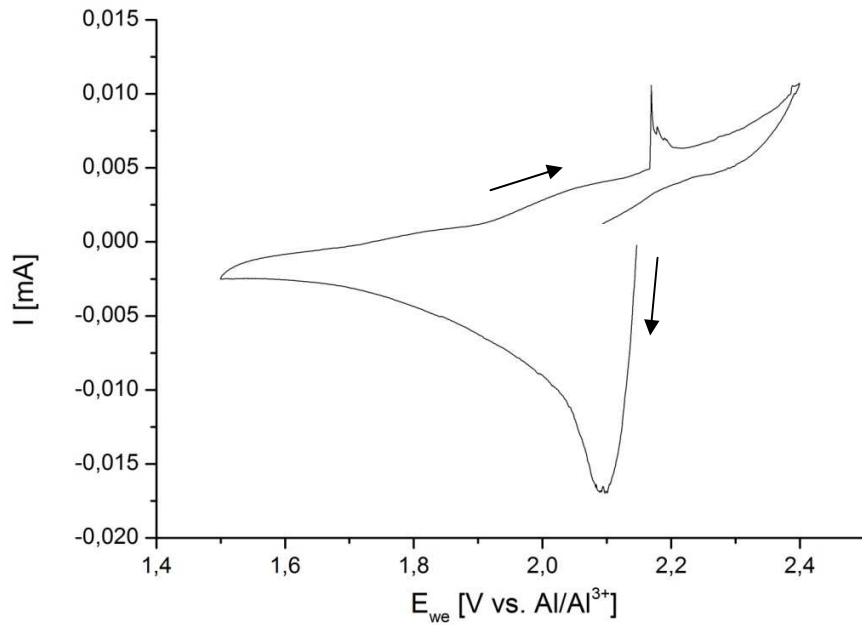


Figure 45: Coin cell - Potentiostatic cycling (0.01 mV/s) of LiMn_2O_4 on stainless steel current collector (59 wt. % LiMn_2O_4 , 21 wt. % Super C65, 20 wt. % PVdF, prepared in NMP) with aluminium counter electrode and $[\text{EMIm}]\text{Cl}$ electrolyte; 1.5 V – 2.4 V; First run: 1st

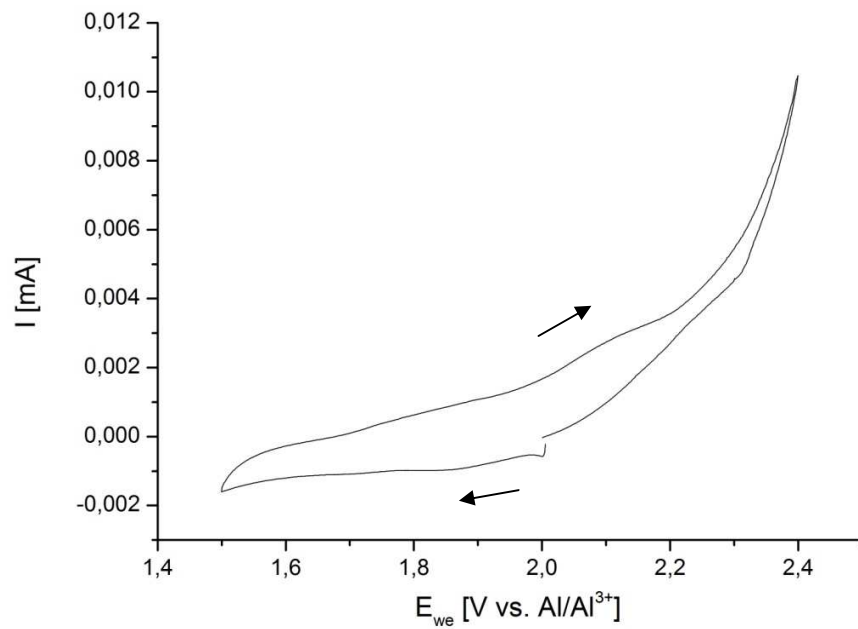


Figure 46: Coin cell - Potentiostatic cycling (0.01 mV/s) of LiMn_2O_4 on stainless steel current collector (59 wt. % LiMn_2O_4 , 21 wt. % Super C65, 20 wt. % PVdF, prepared in NMP) with aluminium counter electrode and $[\text{EMIm}]\text{Cl}$ electrolyte; 1.5 V – 2.4 V; Second run: 2nd

- TiO_2

In Figure 47 is shown a potentiostatically measurement of the working electrode TiO_2 (60 wt. % TiO_2 , 20 wt. % Super C65, 20 wt. % PVdF, prepared in NMP) on a stainless steel current collector in an aluminium battery using $[EMIm]Cl$ with $AlCl_3$ as electrolyte. The scan rate was set to 0.01 mV/s and the voltage limits to 0 V and 1.2 V. There were no peaks observed and at a potential of about 1.05 V corrosion processes occurred. Figure 48 shows a measurement with a similar electrode with a smaller potential window from 0 V to 1.05 V. Again no significant peaks occurred and therefore there is no intercalation reaction of aluminium into TiO_2 .

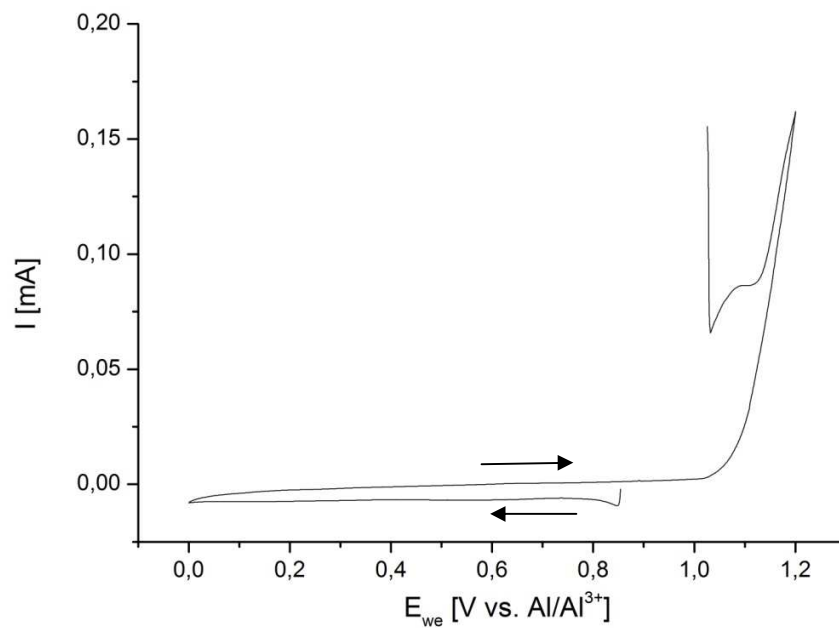


Figure 47: Coin cell - Potentiostatic cycling (0.01 mV/s) of TiO_2 on stainless steel current collector (60 wt. % TiO_2 , 20 wt. % Super C65, 20 wt. % PVdF, prepared in NMP) with aluminium counter electrode and $[EMIm]Cl$ electrolyte; 0 V – 1.2 V

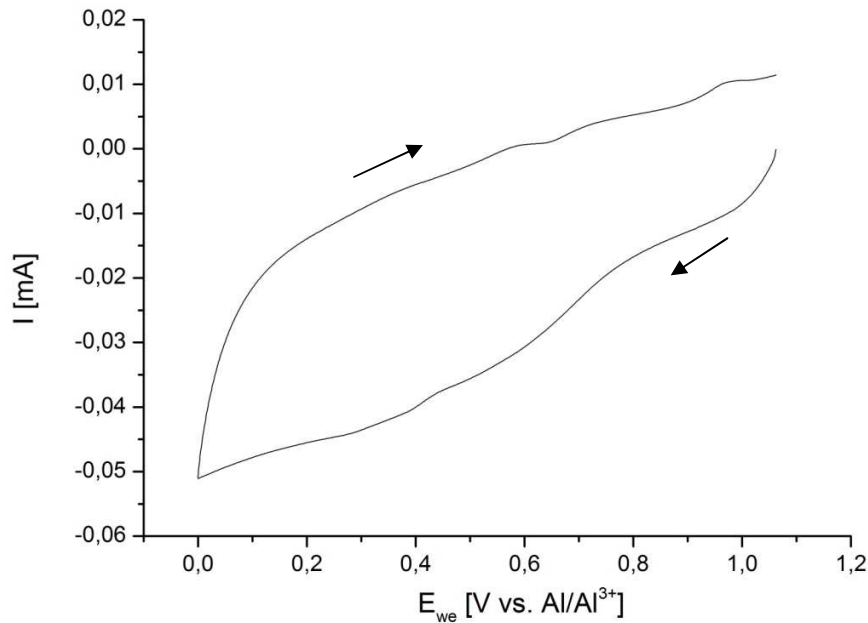


Figure 48: Coin cell - Potentiostatic cycling (0.01 mV/s) of TiO_2 on stainless steel current collector (60 wt. % TiO_2 , 20 wt. % Super C65, 20 wt. % PVdF, prepared in NMP) with aluminium counter electrode and ([EMIm]Cl) electrolyte; 0 V – 1.0 V

4.2.1.2 Solid state NMR measurements

To get more information about the intercalation process of aluminium into the V_2O_5 nanowires solid state NMR measurements were carried out on the aluminium inserted V_2O_5 nanowires. For this measurement an electrode with V_2O_5 nanowires on a stainless steel current collector (27 wt. % V_2O_5 nanowires from the 2nd synthesis, 21 wt. % Super C65, 52 wt. % PVdF, prepared with NMP) in an aluminium battery (counter electrode: aluminium foil, electrolyte: [EMIm]Cl) was galvanostatically swept down to 0 V with a C-rate of C/25 and then the potential was held until the current was less than 0.015 mA, see Figure 49.

After the potential sweep was finished the whole battery was transferred into the glove box. The battery was opened and the working electrode was washed with DMC several times. After drying the electrode at room temperature for about 1 hour in the glove box under argon atmosphere the active material was scratched off the stainless steel current collector and grinded with a pestle and mortar. The powder was then transferred into the solid state NMR measuring rotor, which was subsequently sealed in the glove box. The

sealed rotor was airtight and therefore the electrode was under argon atmosphere for the measurement run.

In Figure 50 a ^{27}Al MAS spectrum of the working electrode made of V_2O_5 nanowires is shown, which was galvanostatically swept down to 0 V in the aluminium ion battery. The pattern shows three broad peaks at a shift of about -13.5, 36 and 77 ppm, which stand for 6-, 5- and 4-fold coordinated aluminium. A narrow peak at 104 ppm represents a 4-fold aluminium site which is likely a remainder from the AlCl_4^- electrolyte.

Figure 51 represents at the bottom a ^{51}V MAS spectrum of V_2O_5 nanowires (2nd synthesis) and above a ^{51}V MAS spectrum of the working electrode from the aluminium ion battery.

The signal noise ratio of the aluminium battery sample is very poor despite the extensive experimental time of two days. The rolling baseline may arise from experimental artefacts (NMR probe ring down) or the presence of paramagnetic vanadium. The paramagnetic V^{III} might be present and is very likely invisible under these conditions (high magnetic field + low MAS frequency) or observed as the broad feature.

The spectrum of the V_2O_5 nanowires is consistent with the literature [92] with a single vanadium environment. Due to quadrupolar broadening a large number of spinning side bands are observed.

The conclusion of this solid state NMR measurement is not completely clear, because it could not be precisely distinguished between intercalated aluminium ions in V_2O_5 nanowires and the oxide Al_2O_3 . Therefore further work has to be undertaken to prove the intercalation of aluminium into V_2O_5 nanowires.

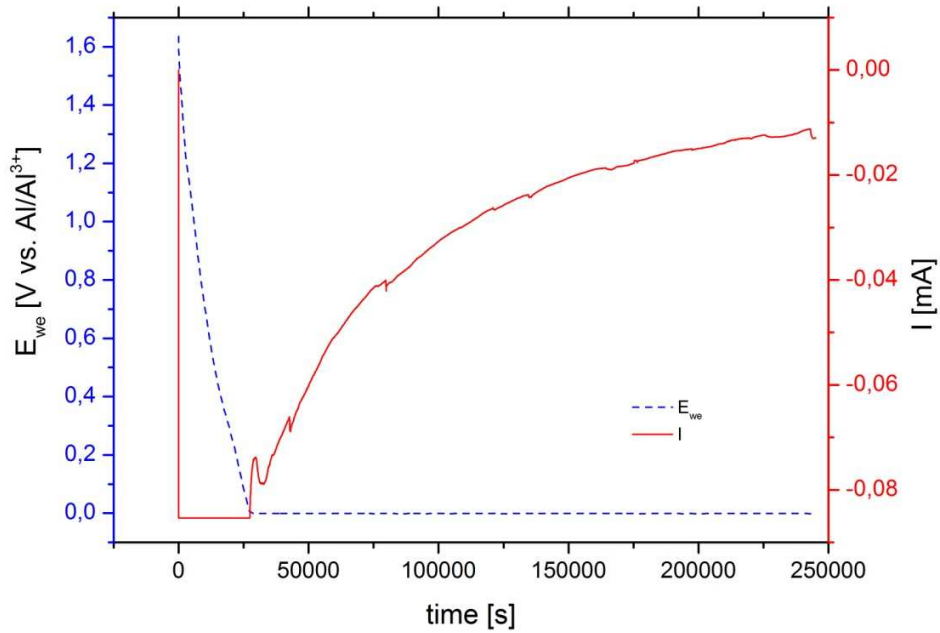


Figure 49: Galvanostatically sweep of V_2O_5 nanowires electrode on a stainless steel current collector (27 wt. % V_2O_5 nanowires from the 2nd synthesis, 21 wt. % Super C65, 52 wt. % PVdF, prepared with NMP) in an aluminium battery (counter electrode: aluminium foil, electrolyte: [EMIm]Cl)

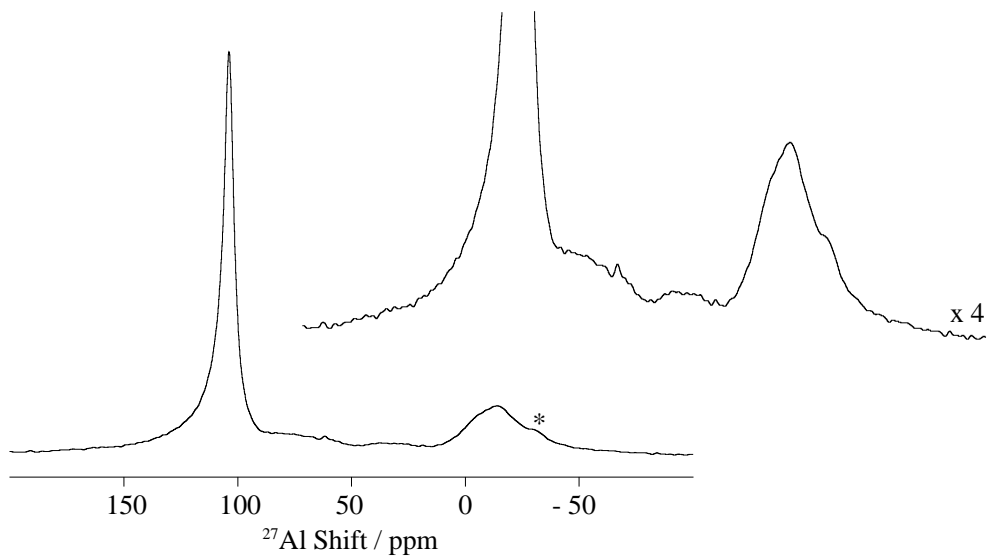


Figure 50: ^{27}Al MAS spectrum of Al-battery recorded under a MAS frequency of $\nu_r = 14$ kHz. The insert shows a magnified view ($\times 4$) of the spectrum. The star denotes spinning sidebands.

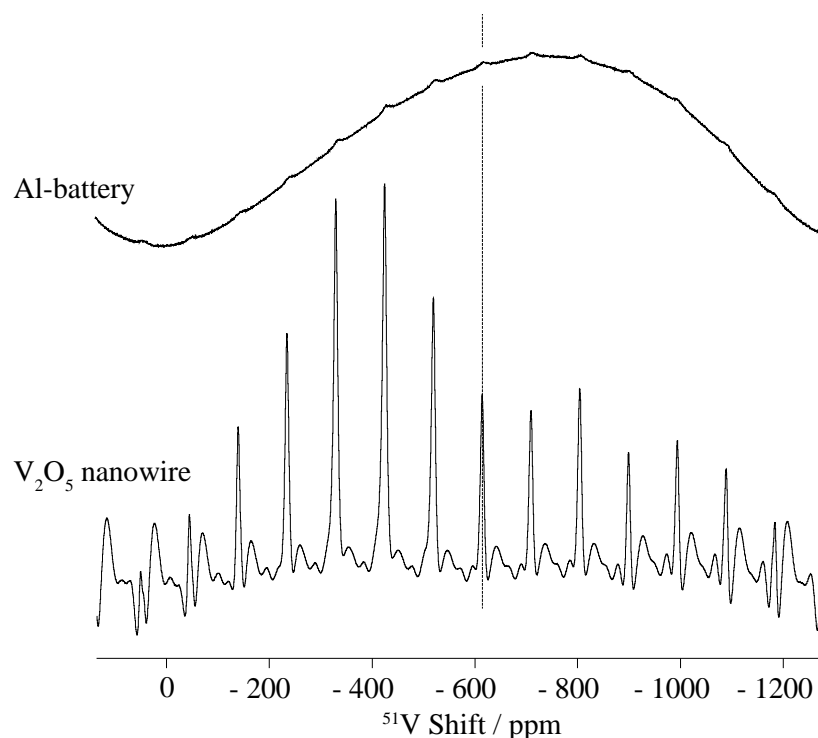


Figure 51: ^{51}V MAS spectrum of V_2O_5 nanowire (from 2nd synthesis) and Al-battery recorded under a MAS frequency of $\nu_r = 10$ kHz. The dashed line shows the ^{51}V isotropic resonance at -620 ppm for V_2O_5 . [92]

4.2.1.3 *In situ* Raman Measurement

An *in situ* Raman measurement of an aluminium battery consisting of a V_2O_5 nanowires working electrode (made via the filter paper preparation method) and an aluminium counter electrode was made. As electrolyte was used the ionic liquid $[\text{EMIm}]\text{Cl}$ with AlCl_3 . Unfortunately it was most of the time not possible to get a good V_2O_5 Raman signal, due to too many background signals from the electrolyte. By using a lot less electrolyte, high laser power of 50%, high confocality and a very short exposure time of just 10 s it was possible to get a spectrum with acceptable signal to noise ratio, see Figure 52. However problems with corrosion reactions occurred and hence the electrochemical cycling was unable to be undertaken in the cell. Therefore further work is required.

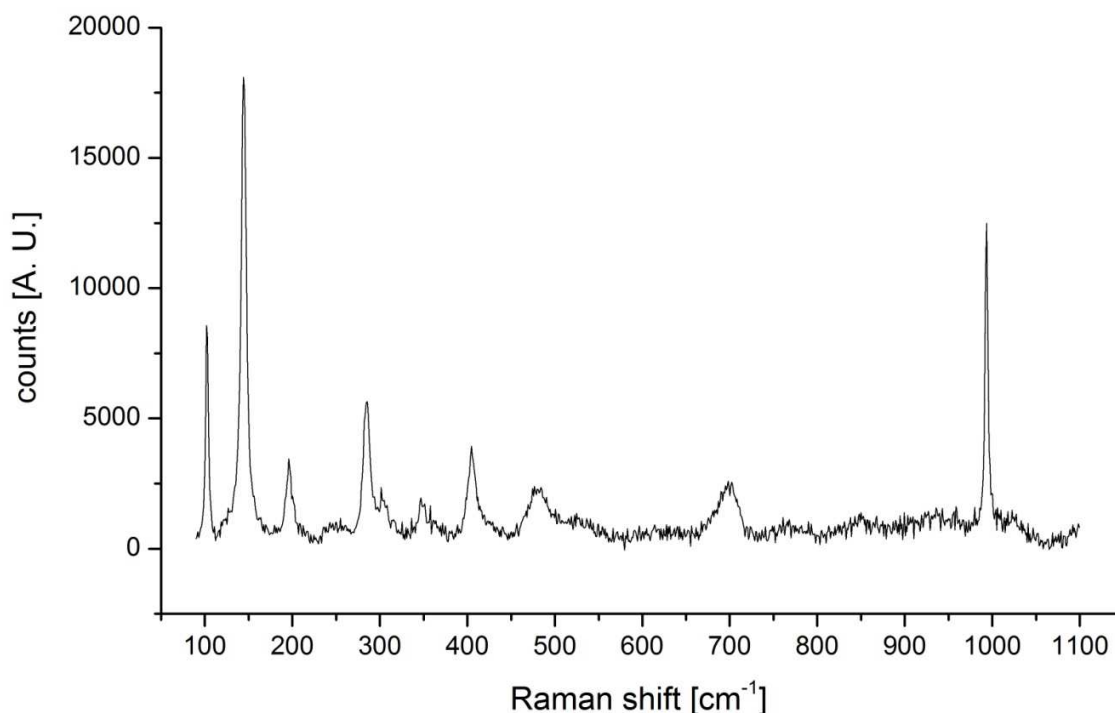


Figure 52: Raman spectrum of V_2O_5 nanowires working electrode within an aluminium battery using [EMIm]Cl as electrolyte; 50% laser power, high confocality, 10 s exposure time, 90-1100 cm^{-1} , baseline correction undertaken

4.2.2 Aqueous $AlCl_3$ Electrolyte

Liu S. et al. [20, 93] suggested in recent papers another aluminium ion battery with an aqueous electrolyte containing $AlCl_3$. As working electrode is used an anatase TiO_2 nanotube array produced by anodization of the metallic titanium foil. Due to the small radius of an aluminium three plus charged ion it should be possible to insert and extract aluminium into and from this anatase TiO_2 nanotube arrays. In this paper researches found a cathodic peak at -1.35 V and an anodic peak at -0.85 V (vs. SCE). The areas under those peaks are very similar to each other and therefore the intercalation seems to be completely reversible.

In Figure 53 is shown a potentiostatic measurement of a TiO_2 electrode (70 wt. % TiO_2 , 15 wt. % Super C65, 15 wt. % PVdF, prepared with Acetone) on an aluminium current collector. This electrode was cut into stripes and one end was put into the 1M aqueous $AlCl_3$ electrolyte. As counter electrode was used a graphite electrode (90 wt. % graphite

SFE 6, 10 wt. % PVdF, prepared with NMP), which was also coated on an aluminium current collector, cut into stripes and put into the electrolyte. The scan rate was 20 mV/s and the potential limits were set to -1.6 V and -0.2 V related to a Ag/AgCl electrode, which was used as reference electrode. The working electrode was cycled four times, but no peaks occurred at all, see Figure 53.

By reducing the scan rate to 1 mV/s a cathodic peak occurred at a potential of about -1.5 V (vs. Ag/AgCl). The saturated Ag/AgCl electrode has a potential of 0.199 V measured against the standard hydrogen electrode and the saturated calomel electrode (SCE) has a potential of 0.241 V (vs. SHE) [94]. This means that -1.5 V vs. Ag/AgCl are -1.542 V vs. SCE. This stands in contrast to the published paper where the cathodic peak for the aluminium insertion should be around -1.35 V (vs. SCE).

After sweeping the cell anodically back towards -0.8 V the cell lost contact at -1.35 V. The reasons for this were corrosion processes which caused the dissolution of the aluminium current collector at the working electrode. This happened every time and therefore it was not possible to measure this kind of battery assembling. All efforts for example changing the current collectors to stainless steel or parafilm were useless. Unfortunately it was not possible to get good spectra of this aluminium battery.

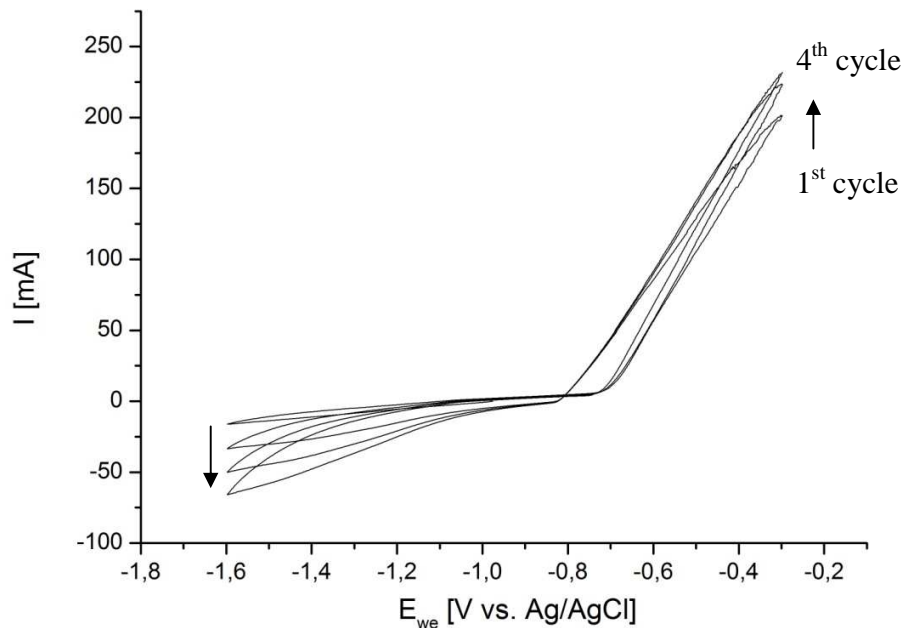


Figure 53: Aqueous aluminium battery, potentiostatically measurement (20 mV/s) of electrode stripes put into the electrolyte (1 M AlCl₃ in water), working electrode: TiO₂ on aluminium current collector (70 wt. % TiO₂, 15 wt. % Super C65, 15 wt. % PVdF, prepared with Acetone), counter electrode: graphite SFE 6 (90 wt. % graphite SFE 6, 10 wt. % PVdF, prepared with NMP)

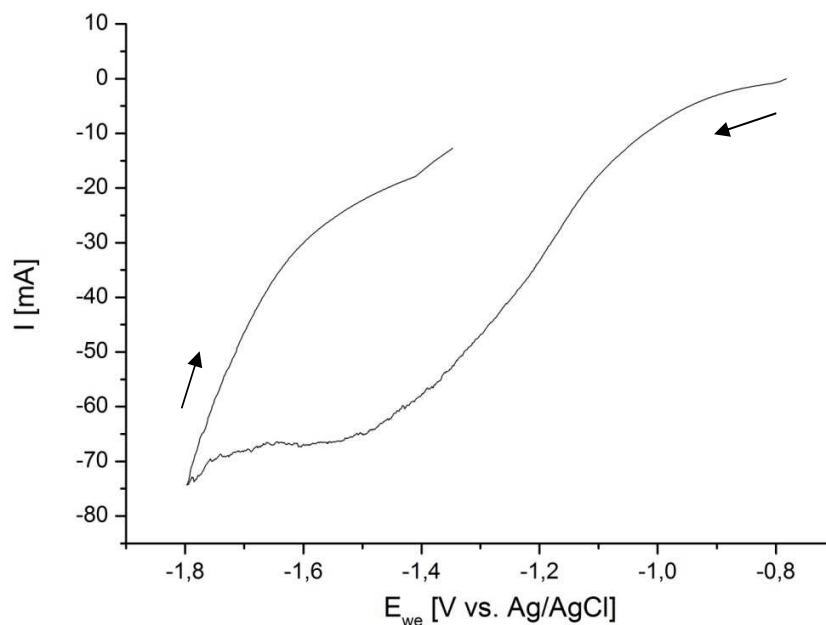


Figure 54: Aqueous aluminium battery, potentiostatically measurement (1 mV/s) of electrode stripes put into the electrolyte (1 M AlCl₃ in water), working electrode: TiO₂ on aluminium current collector (70 wt. % TiO₂, 15 wt. % Super C65, 15 wt. % PVdF, prepared with Acetone), counter electrode: graphite SFE 6 (90 wt. % graphite SFE 6, 10 wt. % PVdF, prepared with NMP)

4.3 Lithium Ion Battery

Different positive and negative electrode materials within a lithium ion battery were electrochemically and spectroscopically analysed. As counter electrode was used lithium metal and as electrolyte a 1:1 solution of EC:DMC including 1 M of a lithium salt (LiPF_6 or LiClO_4).

4.3.1 Electrochemical Characterisation

4.3.1.1 Carbon

In Figure 55 is shown a typical galvanostatic cycling measurement of a working electrode made of Super C 65 (85 wt. % Super C 65, 15 wt. % PVdF, prepared in NMP on a copper current collector) stacked in a coin cell together with a lithium metal reference and a lithium metal counter electrode. As electrolyte was used a solution of 1:1 EC:DMC with 1 M LiClO_4 . The voltage and current is plotted in this diagram against the time.

By analysing the data the voltage gets usually plotted against x , which is the amount of lithium intercalated into the host material relating to the chemical reaction equation, see Figure 56. x can be calculated via the specific charge capacity [Ah/kg] related to the theoretical charge capacity [Ah/kg] of the active material. At ambient temperatures graphitic carbon intercalates one lithium per six carbon atoms [13], see Equation 29, with a theoretical charge capacity of 372 Ah/kg, which can be calculated via Faraday's equation, see Equation 5 in Chapter 0. The measurement was run with a C-rate of C/7, which was calculated for graphitic carbon. In fact one complete discharge or charge was run in about 3,5 hours, see Figure 55. Also the maximum calculated x was only a little bit more than 0.4. The reason for this bad electrochemical behaviour is presumably the fact that the active material was not a carbon with high graphitic contingent, but only a carbon with a high surface area. Super C 65 is usually used as additive for electrodes to provide a high conductivity between the active material and the used current collector. This means that lithium, which preferentially intercalates into graphite sheets, could not intercalate into the whole carbon material and therefore the charge and discharge of the battery was faster than calculated. Nevertheless the typical staging process, which is specified in Chapter 2.2.5.1, can be seen clearly by the three or four steps especially during the

lithiation process see Figure 56. In Figure 57 is shown the corresponding potentiostatic cycling measurement of the Super C 65 electrode. The cathodic peak at 0.6 V during the first cycle relates to the SEI formation.

Equation 29: Intercalation of lithium into carbon at ambient temperatures [13]

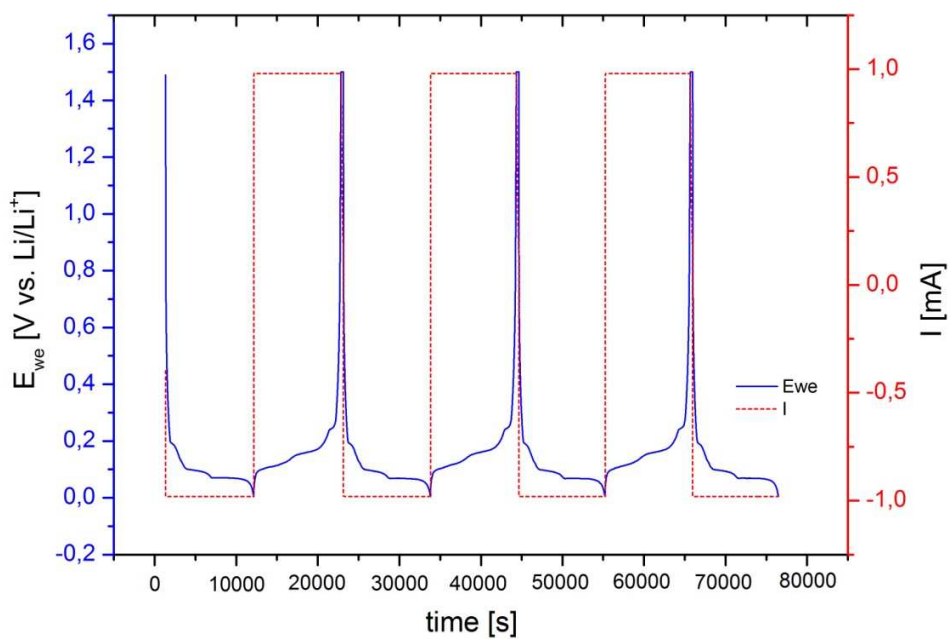
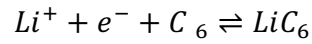


Figure 55: Typical galvanostatic measurement in a coin cell, working electrode: 85 wt. % Super C 65, 15 wt. % PVdF, prepared in NMP on copper current collector, counter electrode: lithium metal, electrolyte: 1:1 EC:DMC with 1 M LiClO₄, reference electrode: lithium metal, actual C-rate of 3.5

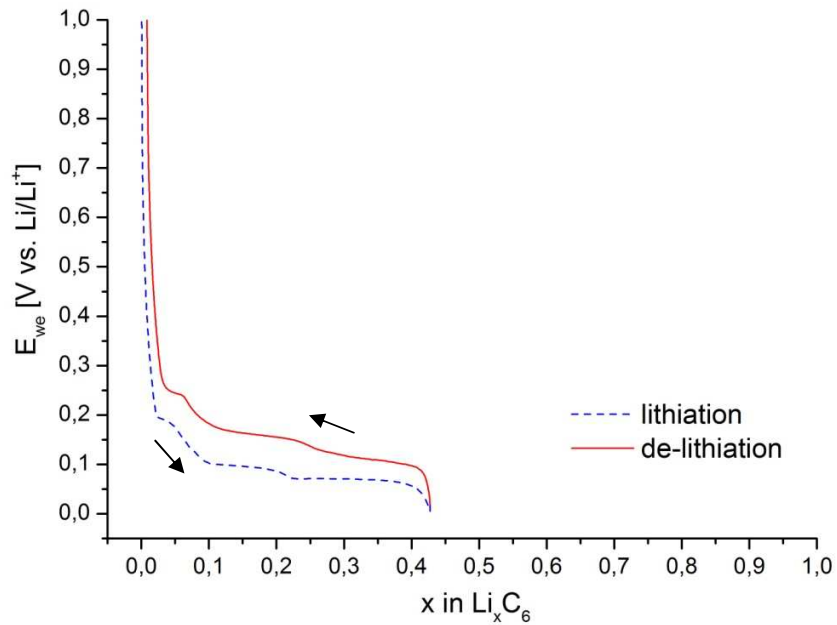


Figure 56: Galvanostatic measurement in a coin cell, one lithiation and de-lithiation of a working electrode: 85 wt. % Super C 65, 15 wt. % PVdF, prepared in NMP on copper current collector, counter electrode: lithium metal, electrolyte: 1:1 EC:DMC with 1 M LiClO₄, reference electrode: lithium metal, actual C-rate of 3.5

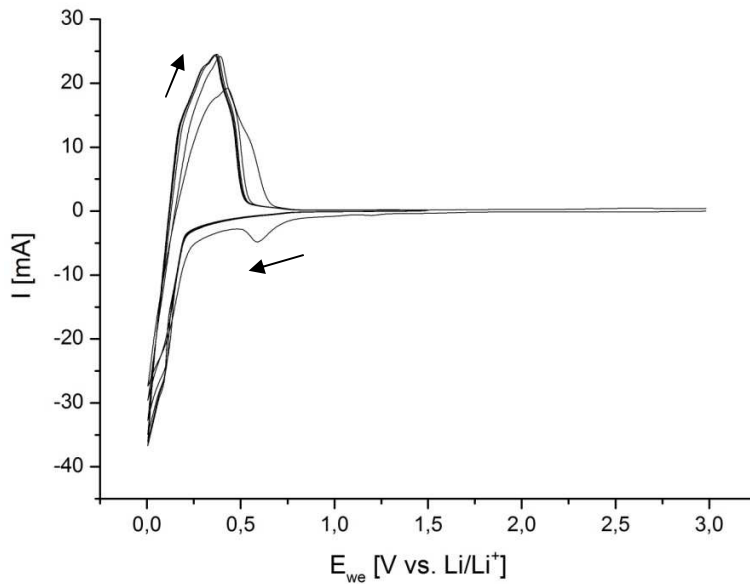


Figure 57: Potentiostatic Cycling of Super C 65 (85 wt. % Super C 65, 15 wt. % PVdF, prepared in NMP on a copper current collector) in a lithium battery; scan rate: 0.1 mV/s; counter electrode: lithium metal, electrolyte: 1:1 EC:DMC with 1 M LiClO₄, reference electrode: lithium metal, potential limits: 0,005 V and 3.0 V

4.3.1.2 LiMn_2O_4

LiMn_2O_4 de-intercalates lithium reversibly at a potential of about 4 V (vs. Li/Li^+) down to $0.015x$ according to the oxidation reaction shown in Equation 30, which is marked by two peaks in the potentiostatic cycling voltammogram shown in Figure 58. During the de-lithiation down to $0.5x$ the LiMn_2O_4 retains in a cubic structure, where the lithium atoms are at the tetrahedral sites. From $0.5x$ on occurs another new cubic structure besides the other one. [13, 61]. In Figure 59 is shown the first cycle of a galvanostatic measurement cycled with $C/5$. Typical for continuous charge-discharge cycling of $\text{Li}_x\text{Mn}_2\text{O}_4$ in a high voltage range is a strong capacity fading see Figure 60, caused by dissolution of manganese ions into the electrolyte leading in a lithium poor defect spinel. [95]

Equation 30: Delithiation reaction of LiMn_2O_4 [61]

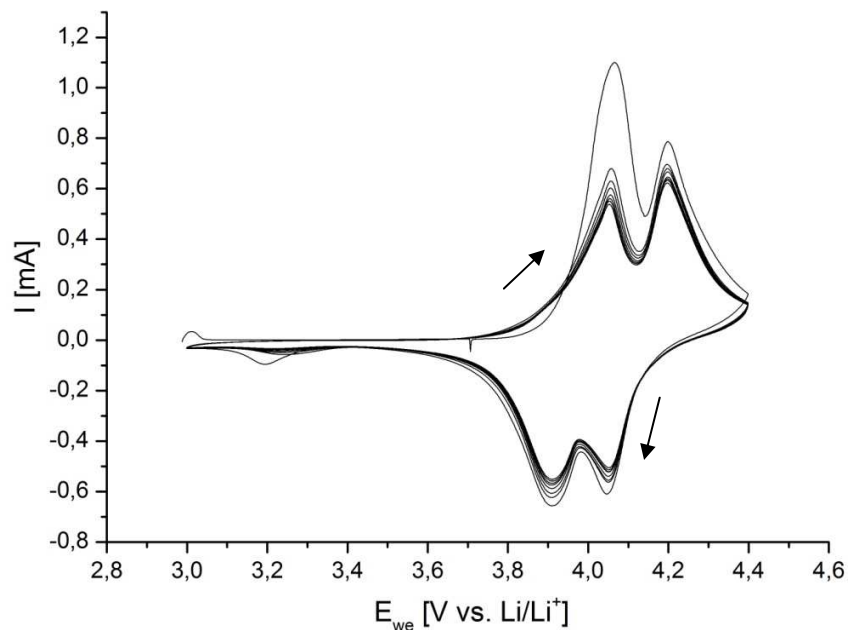
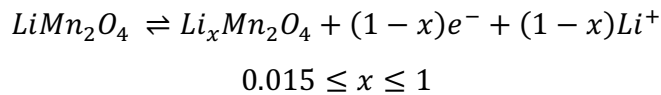


Figure 58: Potentiostatic cycling of LiMn_2O_4 electrode (68 wt. % LiMn_2O_4 , 17 wt. % Super C 65, 15 wt. % PVdF, prepared with NMP, coated on aluminium current collector), counter electrode: lithium metal, electrolyte: 1:1 EC:DMC with 1 M LiClO_4 , reference electrode: lithium metal, scan rate: 0.1 mV/s, potential limits: 3.0 V and 4.4 V

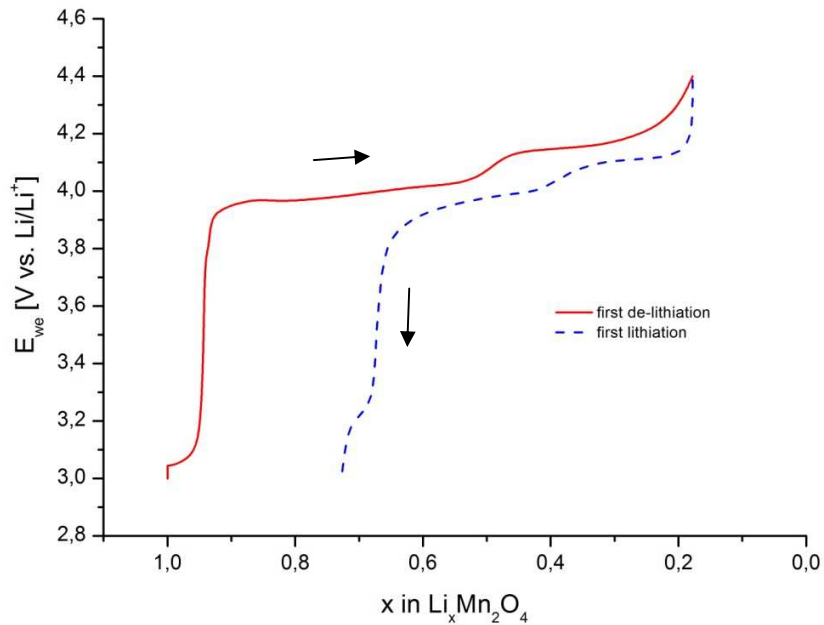


Figure 59: First cycle of a galvanostatic measurement of LiMn_2O_4 (68 wt. % LiMn_2O_4 , 17 wt. % Super C 65, 15 wt. % PVdF, prepared with NMP, coated on aluminium current collector) with C/5, potential limits: 4.4 V and 3.0 V, counter electrode: lithium metal, electrolyte: 1:1 EC:DMC with 1 M LiClO_4 , reference electrode: lithium metal

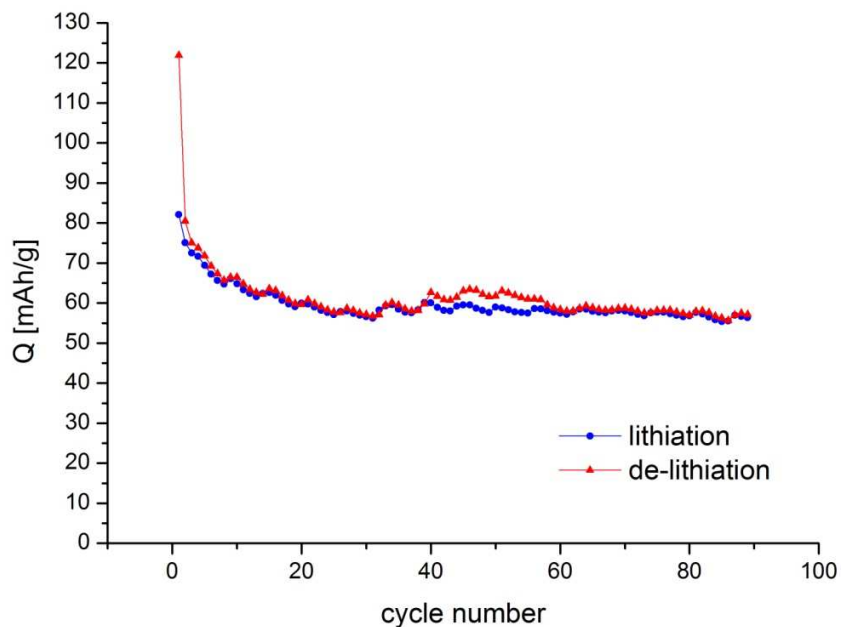


Figure 60: Specific charge capacities of a galvanostatic measurement of LiMn_2O_4 (68 wt. % LiMn_2O_4 , 17 wt. % Super C 65, 15 wt. % PVdF, prepared with NMP, coated on aluminium current collector) with C/5, potential limits: 4.4 V and 3.0 V, counter electrode: lithium metal, electrolyte: 1:1 EC:DMC with 1 M LiClO_4 , reference electrode: lithium metal

4.3.1.3 TiO_2

TiO_2 inserts lithium up to a content of 0.6 lithium atoms per mole of titanium oxide following Equation 31. TiO_2 consists of an orthorhombic crystal lattice, where the lithium ions intercalate into half of the octahedral voids. The maximum possible amount of lithium atoms per titanium oxide molecule was confirmed by theoretical calculations as well as by electrochemical experiments [96]. The intercalation of lithium occurs at a potential of about 1.7 V and the de-lithiation with a little bit higher voltage of about 1.9 V, see Figure 61 and Figure 62. The specific charge capacities for both lithiation and de-lithiation are shown in Figure 63. The increasing capacities could be explained by the possible improved wetting of the electrodes during the first cycles.

Equation 31: Lithiation reaction of TiO_2 [61]

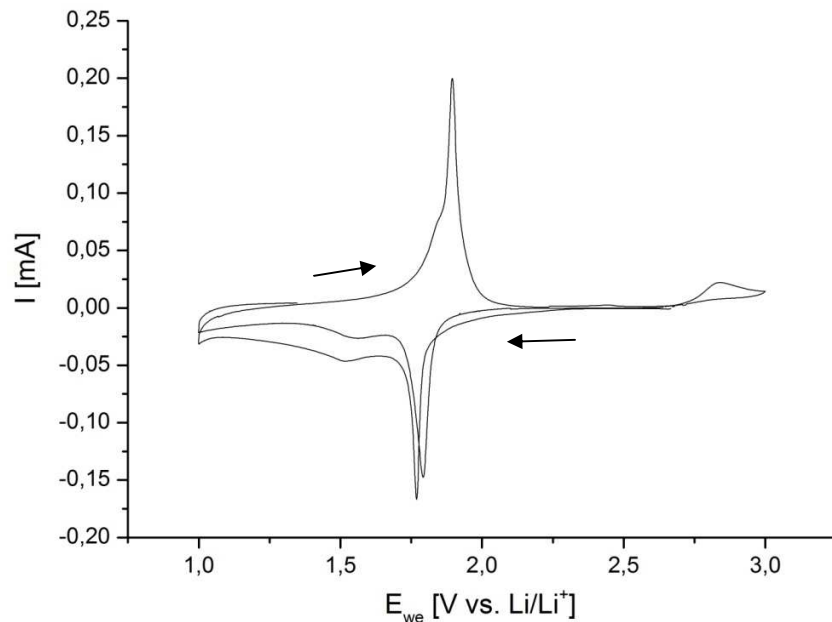
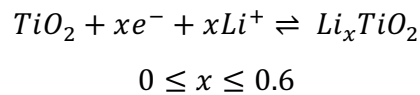


Figure 61: Potentiostatic cycling of TiO_2 (60 wt. % TiO_2 , 20 wt. % Super C 65, 20 wt. % PVdF, prepared with NMP, coated on copper current collector), counter electrode: lithium metal, electrolyte: 1:1 EC:DMC with 1 M $LiClO_4$, reference electrode: lithium metal, scan rate: 0.01 mV/s, potential limits: 1.0 V and 3.0 V

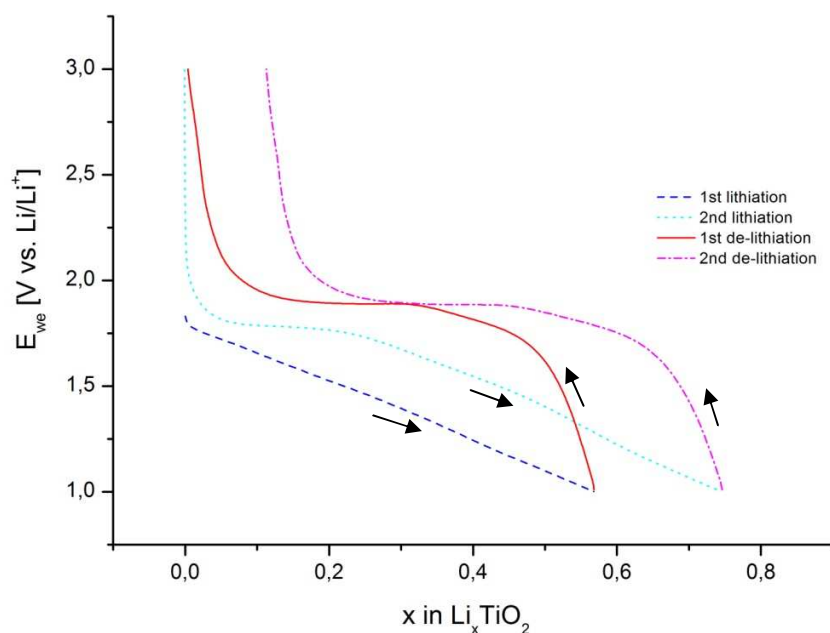


Figure 62: First two cycles of a galvanostatic measurement of TiO_2 (60 wt. % TiO_2 , 20 wt. % Super C 65, 20 wt. % PVdF, prepared with NMP, coated on copper current collector) with C/5, potential limits: 1.0 V and 3.0 V, counter electrode: lithium metal, electrolyte: 1:1 EC:DMC with 1 M LiClO_4 , reference electrode: lithium metal

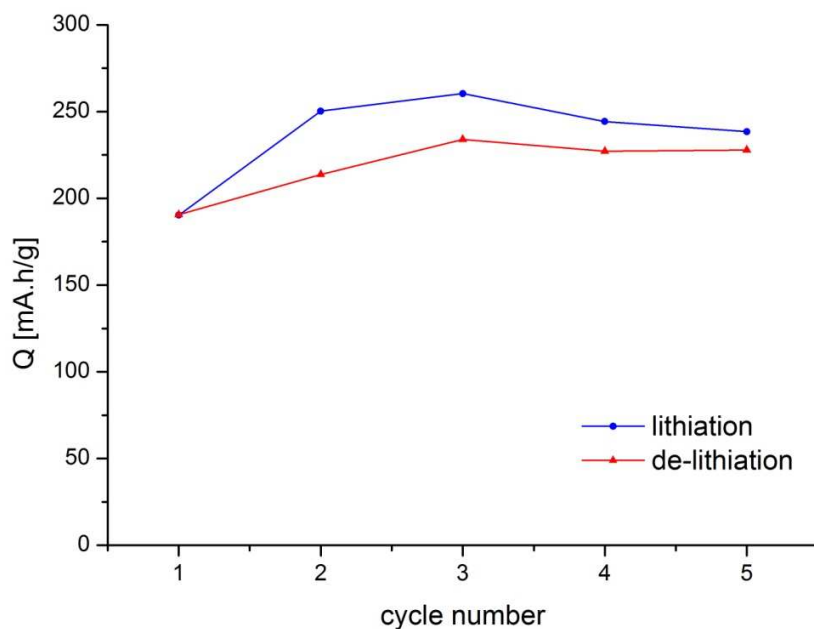
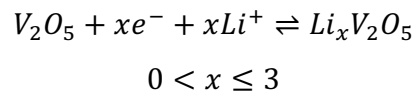


Figure 63: Specific charge capacities of a galvanostatic measurement of TiO_2 (60 wt. % TiO_2 , 20 wt. % Super C 65, 20 wt. % PVdF, prepared with NMP, coated on copper current collector) with C/5, potential limits: 1.0 V and 3.0 V, counter electrode: lithium metal, electrolyte: 1:1 EC:DMC with 1 M LiClO_4 , reference electrode: lithium metal

4.3.1.4 V_2O_5

V_2O_5 inserts lithium up to a stoichiometry of three lithium atoms per V_2O_5 molecule, according to Equation 32. Its discharge curve is characterised by three significant plateaus, caused by different lithiated phases being involved in the discharge process. Their complexity is mainly the reason why the Li/V_2O_5 system is not completely understood by now. Figure 64 shows a typical discharge curve with all different lithiated phases. The α , ε and δ phase transitions occur up to a lithium content of $x=1$ and are all fully reversible. They consist of a similar layered structure like the primary V_2O_5 material. With the increase of lithium content from the α to the ε phase the layers get more puckered and the distance between the layers get stretched. The γ and δ transformations are in contrast to the others irreversible, due to deformations of the V_2O_5 layers, which lead to an irreversible symmetry loss and bond breaking. By the intercalation of three lithium atoms per V_2O_5 molecule a weakly crystallized ω -phase is formed, which has a tetragonal or cubic symmetry. Between those phase transformations is always a region where two phases exist in parallel. [28, 61, 62]

Equation 32: Lithiation reaction of V_2O_5 [61]



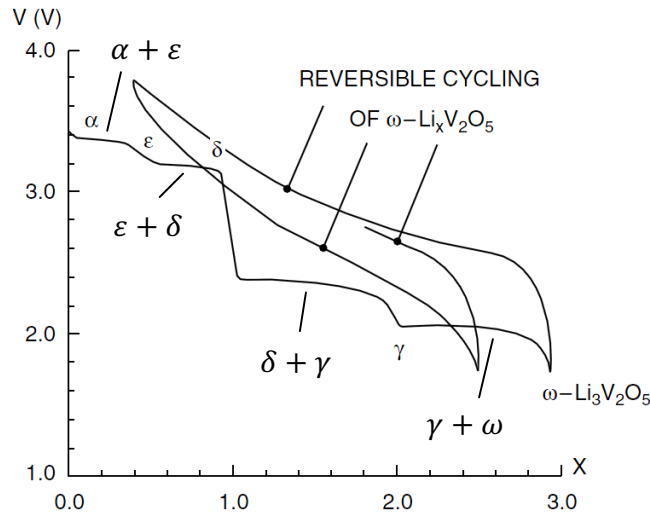


Figure 64: Typical discharge curve of V_2O_5 showing the three significant plateaus with the corresponding phases [28]

- *Commercial Powder*

In Figure 65 is shown the first cycle of a galvanostatic measurement of an electrode made of V_2O_5 commercial powder (60 wt. % V_2O_5 commercial powder, 20 wt. % Super C 65, 20 wt. % PVdF, prepared with NMP, coated on aluminium current collector). The battery was discharged with a C-rate of C/4 and the potential limits were set to 1.0 V and 4.2 V. As counter electrode was used lithium metal and the electrolyte was a solution of 1:1 EC:DMC with 1 M $LiClO_4$. Lithium metal served as a reference electrode.

The first discharge process clearly shows three flat plateaus, which can be attributed to the different phase transformations. The α and ϵ phase cannot be distinguished in this plot, but the phase transformation occurs at a potential of about 3.2 V and is finished before reaching $x=1$, as written in the literature. Between $1 < x < 1.8$ occurs the transformation of the ϵ phase into the δ phase at a potential of 2.25 V. The last transformation to the ω -phase happened at a potential of 1.8 V. The maximum intercalated lithium amount was about 2.5 lithium atoms per V_2O_5 molecule.

In Figure 66 is shown the capacity change of the charge (de-lithiation) and discharge (lithiation) process within 19 cycles. The enormous decrease of capacity from 360 mAh/g to 230 mAh/g can be explained by the irreversible phase transition to the γ and ω phase.

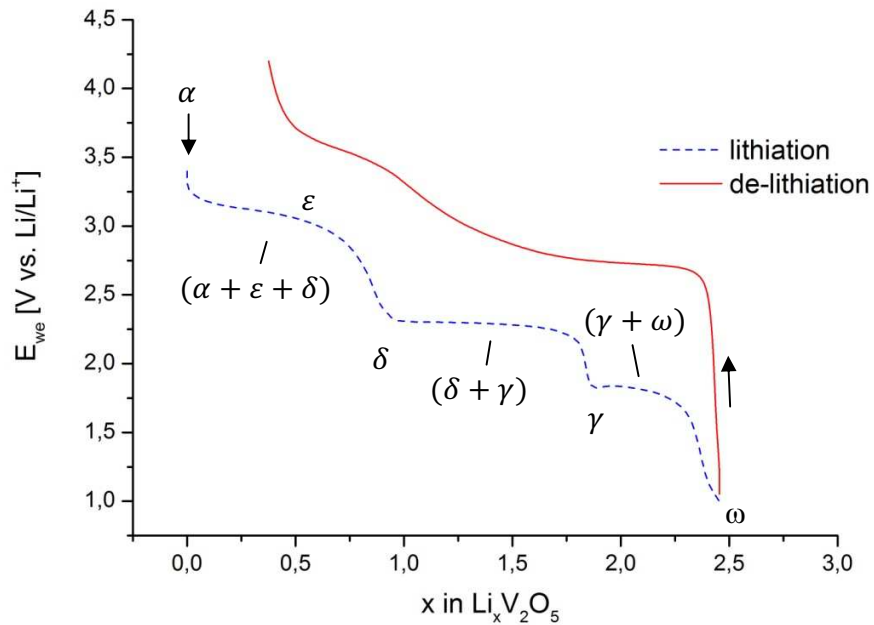


Figure 65: First cycle of a galvanostatic measurement of V_2O_5 commercial powder (60 wt. % V_2O_5 commercial powder, 20 wt. % Super C 65, 20 wt. % PVdF, prepared with NMP, coated on aluminium current collector) with C/4, potential limits: 1.0 V and 4.2 V, counter electrode: lithium metal, electrolyte: 1:1 EC:DMC with 1 M $LiClO_4$, reference electrode: lithium metal

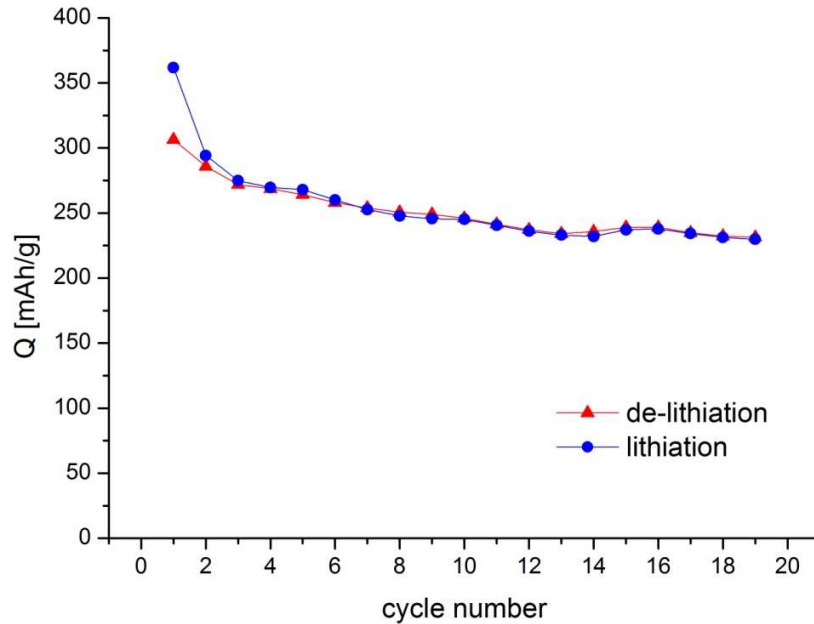


Figure 66: Specific charge capacities of a galvanostatic measurement of V_2O_5 commercial powder (60 wt. % V_2O_5 commercial powder, 20 wt. % Super C 65, 20 wt. % PVdF, prepared with NMP, coated on aluminium current collector) with C/4, potential limits: 1.0 V and 4.2 V, counter electrode: lithium metal, electrolyte: 1:1 EC:DMC with 1 M $LiClO_4$, reference electrode: lithium metal

- *Nanowires*

In Figure 67 is shown the first cycle of a galvanostatic measurement of the system Li/V₂O₅-nanowires. The electrode was made of 60 wt. % V₂O₅ nanowires, 20 wt. % Super C 65, 20 wt. % PVdF. A suspension with those powders was made with the aid of NMP and afterwards it was coated on an aluminium current collector. The battery was stacked with lithium metal as counter electrode and a lithium metal reference electrode. The cell was cycled with C/4 with the potential limits of 1.0 V and 3.5 V. As electrolyte was used 1:1 EC:DMC with 1 M LiClO₄.

As by the commercial powder there occurred just three potential steps. The phase transformation between α , ϵ and δ cannot be distinguished. Those transformations happened at a potential of about 3 V and ended with an x value of about 0.35. This is different to the measurement with the commercial powder, where the x-value was near to 1. The γ phase transformation began at a potential of 2 V and was finished with a stoichiometrie of about x=0.7. The last phase ω came into being at a potential of 1.6 V and reached a lithium content of a little bit less than 1. The biggest difference to the commercial powder is little lithium intercalation content of only about x=1 compared to nearly x=3 of the commercial powder. Another conspicuous difference is that the potential plateaus are steeper. The potentials of the different phase transformations are a little bit lower compared to the commercial V₂O₅ powder.

The capacity changes within the first 50 cycles are shown in Figure 68. There is also a big capacity loss after the first cycle from 140 mAh/g to 60 mAh/g due to the irreversible phase transition to the γ and ω phase within the first discharge cycle. The first charge cycle does only include one de-intercalation step where only half of the lithium atoms were removed. Compared to the commercial V₂O₅ powder, see Figure 66, the nanowires seem to be worse, due to the bigger capacity fading down to less than 30 mAh/g within the first 30 cycles.

In Figure 69 is plotted the corresponding cycling voltammetry measurement. The potential limits were set to 1.6 and 3.8 V and the measurement was run with a scan rate of 0.1 mV/s. In this measurement can be distinguished between the phase transformation of α to ϵ at about 3.25 V and the ϵ to δ transformation at about 3.1 V. At 2.2 V occurs the γ

phase. After the first discharge cycle down to 1.6 V the current was reduced by half. This again is caused presumably by the irreversible phase transformation to the γ phase.

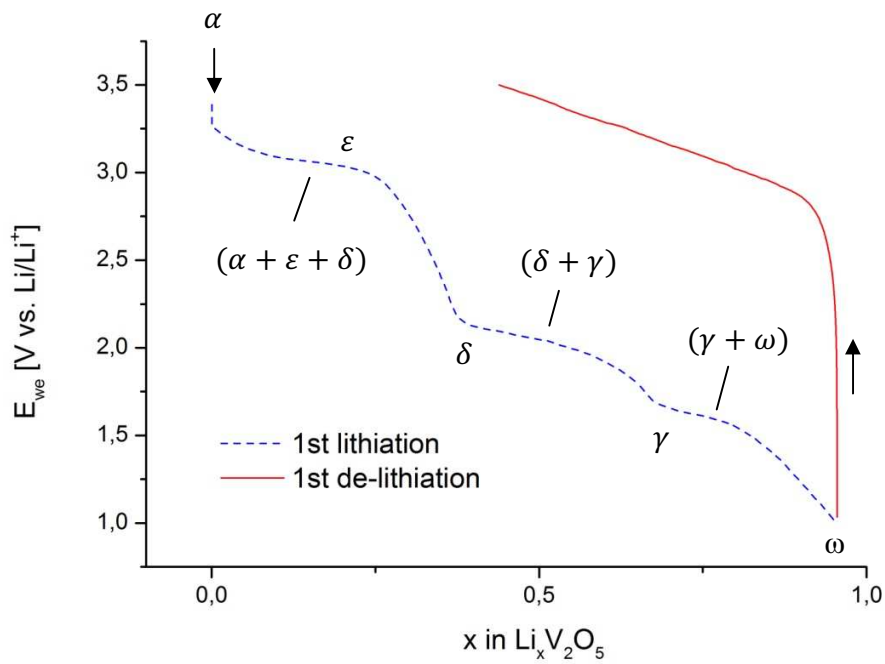


Figure 67: First cycle of a galvanostatic measurement of V_2O_5 nanowires (60 wt. % V_2O_5 nanowires, 20 wt. % Super C 65, 20 wt. % PVdF, prepared with NMP, coated on aluminium current collector) with C/4, potential limits: 1.0 V and 3.5 V, counter electrode: lithium metal, electrolyte: 1:1 EC:DMC with 1 M $LiClO_4$, reference electrode: lithium metal

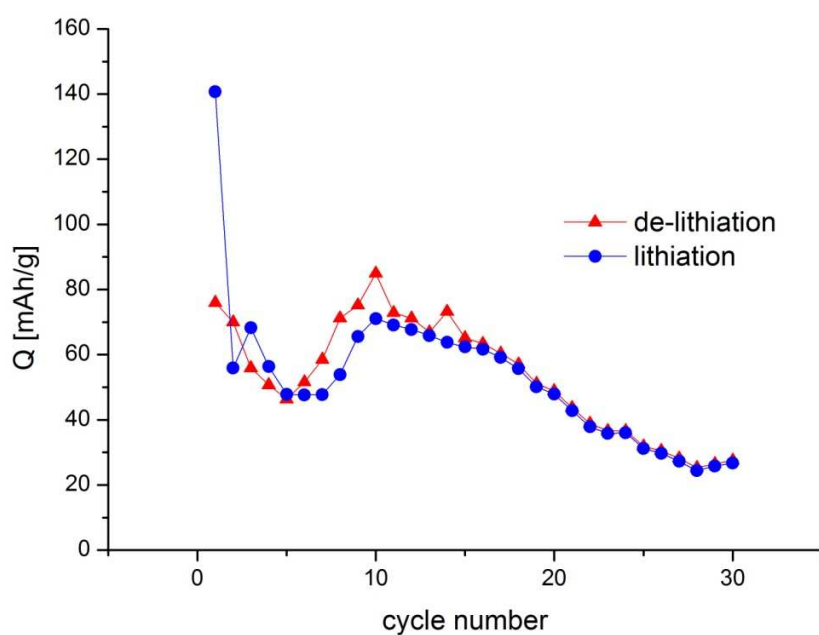


Figure 68: Specific charge capacities of a galvanostatic measurement of V_2O_5 nanowires (60 wt. % V_2O_5 commercial powder, 20 wt. % Super C 65, 20 wt. % PVdF, prepared with NMP, coated on aluminium current collector) with C/4, potential limits: 1.0 V and 3.5 V, counter electrode: lithium metal, electrolyte: 1:1 EC:DMC with 1 M $LiClO_4$, reference electrode: lithium metal

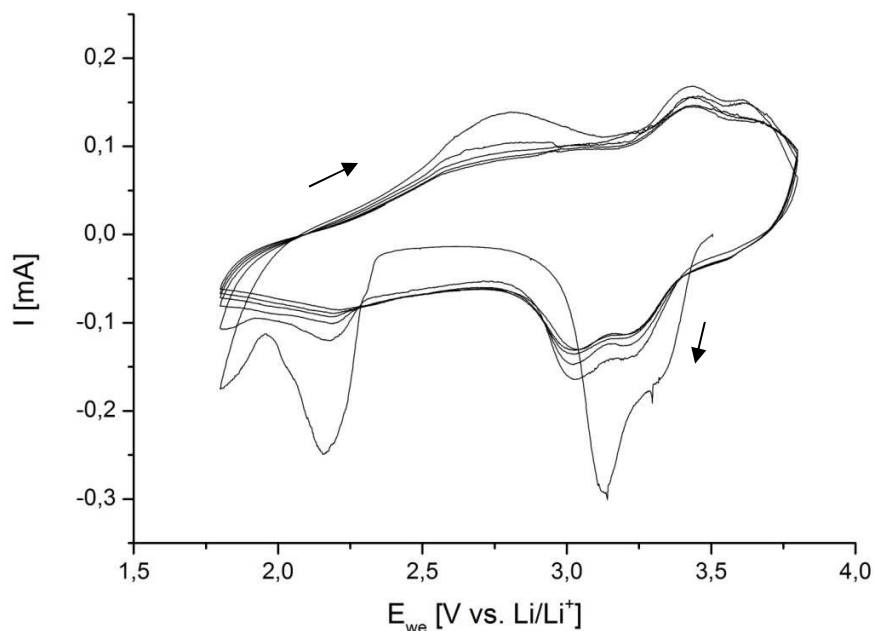
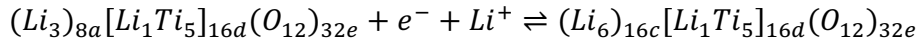


Figure 69: Potentiostatic cycling of V_2O_5 nanowires (60 wt. % V_2O_5 commercial powder, 20 wt. % Super C 65, 20 wt. % PVdF, prepared with NMP, coated on aluminium current collector), counter electrode: lithium metal, electrolyte: 1:1 EC:DMC with 1 M $LiClO_4$, reference electrode: lithium metal, scan rate: 0.1 mV/s, potential limits: 1.6 V and 3.8 V

4.3.1.5 $\text{Li}_4\text{Ti}_5\text{O}_{12}$

The lithium atoms in lithium titanate ($\text{Li}_4\text{Ti}_5\text{O}_{12}$) occupy all tetrahedral 8a voids forming the spinel $(\text{Li}_3)_{8a}[\text{Li}_1\text{Ti}_5]_{16d}(\text{O}_{12})_{32e}$, which has a very low electric conductivity. During discharge the lithium atoms move from the 8a to the 16c interstitials leading to $(\text{Li}_6)_{16c}[\text{Li}_1\text{Ti}_5]_{16d}(\text{O}_{12})_{32e}$ with a better electronic conductivity, see also Equation 33. The reversible lithiation process is characterised by an extremely flat voltage plateau at about 1.55 V (vs. Li/Li^+). [66, 97, 98]

Equation 33: Lithiation intercalation of $\text{Li}_4\text{Ti}_5\text{O}_{12}$ [97]



In Figure 70 are plotted the first two cycles of a galvanostatic cycling measurement of a $\text{Li}_4\text{Ti}_5\text{O}_{12}$ which consisted of 82 wt. % $\text{Li}_4\text{Ti}_5\text{O}_{12}$, 10 wt. % Super C 65 and 8 wt. % of PVdF. Lithium metal was used as counter electrode as well as a separate reference electrode. As electrolyte was used a solution of 1:1 EC:DMC with 1 M LiClO_4 . The potential limits were set to 1.0 V and 3.0 V (vs. Li/Li^+) and the cell was cycled with C/5. The diagram shows a flat voltage plateau at a potential of about 1.5 V. Also in the first charge and second discharge occurred this voltage step. In Figure 71 is shown the corresponding cycling voltammetry measurement scanned with 0.1 mV/s. The intercalation and de-intercalation of lithium can be clearly seen by the two sharp peaks occurring at a potential of 1.5 V during discharge and 1.65 V during charge process.

Figure 72 shows the specific charge capacities within 11 cycles. The charge capacities decrease from 158 mAh/g to 143 mAh/g and the discharge capacities from 148 mAh/g to 142 mAh/g.

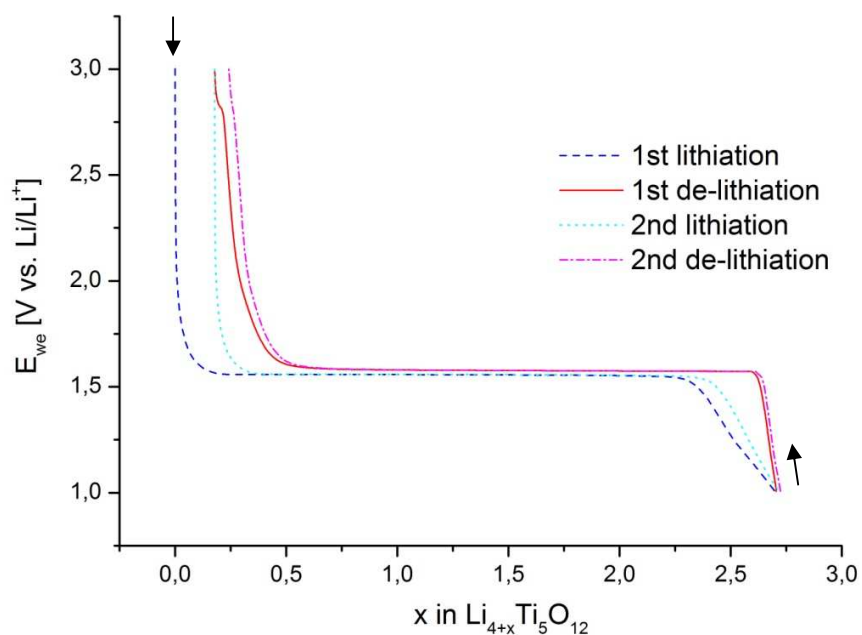


Figure 70: First two cycles of a galvanostatic measurement of a $\text{Li}_4\text{Ti}_5\text{O}_{12}$ electrode made of 82 wt. % $\text{Li}_4\text{Ti}_5\text{O}_{12}$, 10 wt. % Super C 65, 8 wt. % PVdF, prepared with NMP, coated on copper current collector) with C/5, potential limits: 1.0 V and 3.0 V, counter electrode: lithium metal, electrolyte: 1:1 EC:DMC with 1 M LiClO_4 , reference electrode: lithium metal

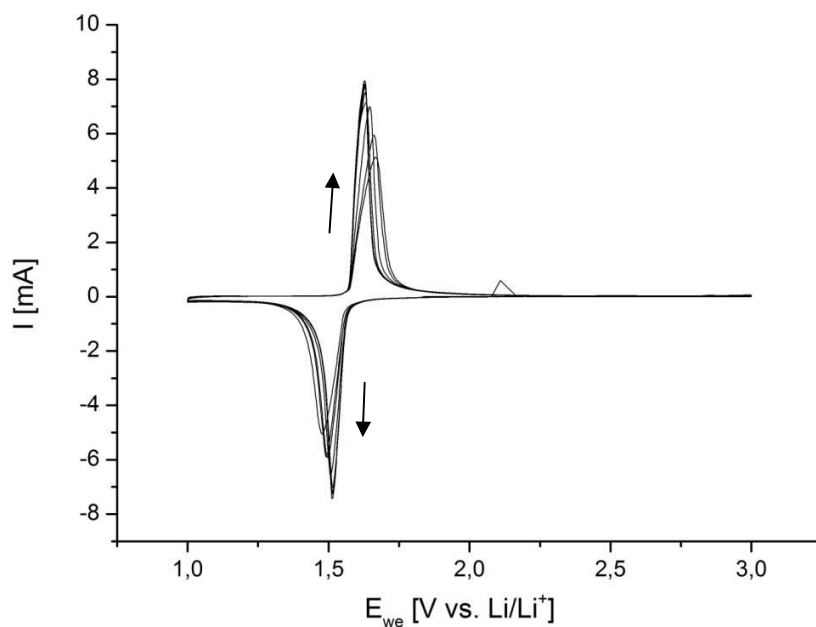


Figure 71: Potentiostatic cycling of a $\text{Li}_4\text{Ti}_5\text{O}_{12}$ electrode made of 82 wt. % $\text{Li}_4\text{Ti}_5\text{O}_{12}$, 10 wt. % Super C 65, 8 wt. % PVdF, prepared with NMP, coated on copper current collector) counter electrode: lithium metal, electrolyte: 1:1 EC:DMC with 1 M LiClO_4 , reference electrode: lithium metal, scan rate: 0.1 mV/s, potential limits: 1.0 V and 3.0 V

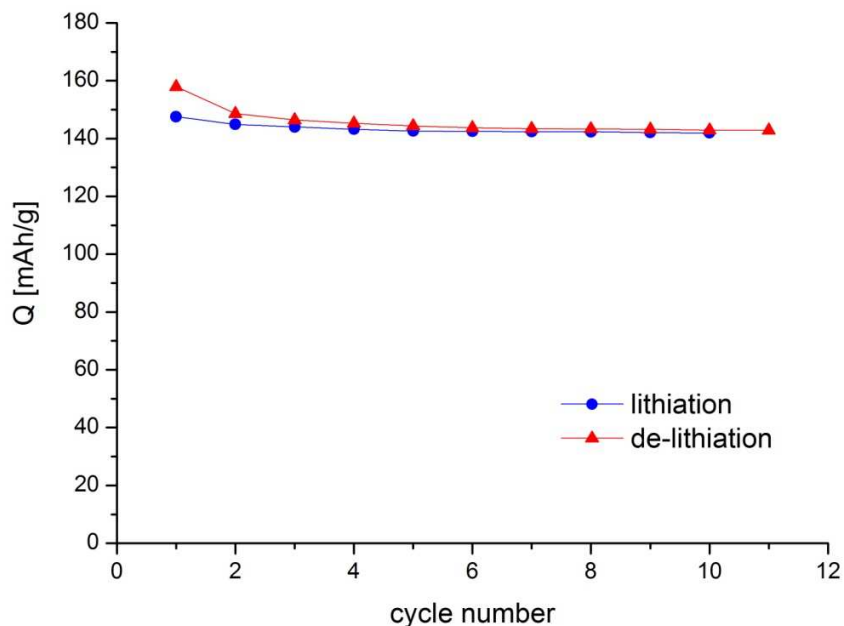


Figure 72: Specific charge capacities of a galvanostatic measurement of a $\text{Li}_4\text{Ti}_5\text{O}_{12}$ electrode made of 82 wt. % $\text{Li}_4\text{Ti}_5\text{O}_{12}$, 10 wt. % Super C 65, 8 wt. % PVdF, prepared with NMP, coated on copper current collector) with C/5, potential limits: 1.0 V and 3.0 V, counter electrode: lithium metal, electrolyte: 1:1 EC:DMC with 1 M LiClO_4 , reference electrode: lithium metal

4.3.2 Raman Measurements

4.3.2.1 PVdF - Binder Material

Polyvinylidene fluoride, with the molecular formula $(\text{CH}_2\text{CF}_2)_n$, is the most widely used binder for lithium electrodes, due to its good electrochemical stability and its great adhesion to the electrode materials and current collector. [99] PVdF is a semi-crystalline polymer with four possible crystal phases called α , β , γ and δ whereat only the β phase is used as an organic piezoelectric and ferroelectric material. It can be easily gained by mechanical stretching of the non-polar α phase, which crystallises directly from the melt. [100]

In Figure 73 is shown a Raman measurement of pure Polyvinylidene Fluoride (PVdF). There occurred significantly peaks at a Raman shift of 287 cm^{-1} , 412 cm^{-1} , 610 cm^{-1} , 795 cm^{-1} , 839 cm^{-1} and 874 cm^{-1} , whereat the one at 795 cm^{-1} has the highest intensity. Additionally one broad peak at around 560 cm^{-1} was measured. The peaks correlate well with the literature, where the peaks for the α -phase occur at 284 cm^{-1} , 410 cm^{-1} , 609 cm^{-1} ,

764 cm^{-1} , 837 cm^{-1} and 872 cm^{-1} using also a He-Ne-laser with a wavelength of 632.8 nm. [100]

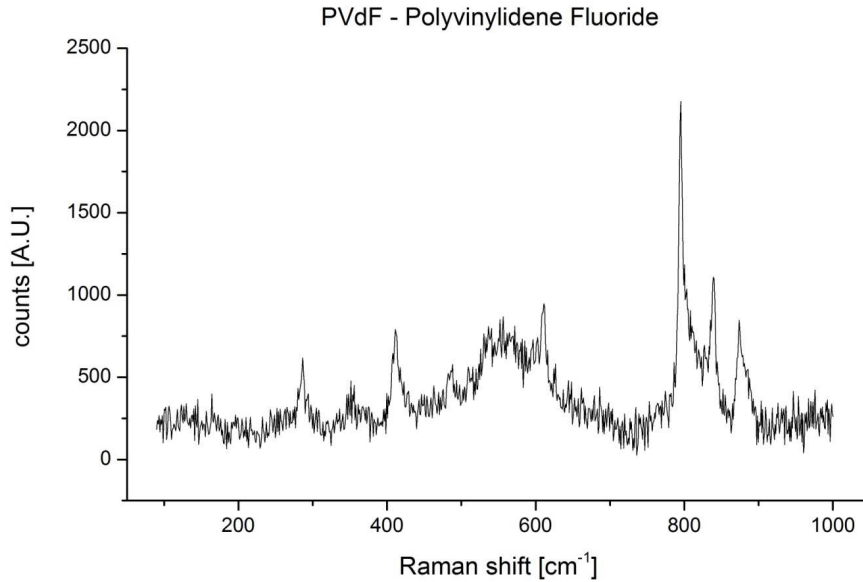


Figure 73: Raman measurement of PVdF binder material, He-Ne-laser ($\lambda=632.816$ nm), laser power: 100%, exposure time: 10 s, range: 90-1000 cm^{-1}

4.3.2.2 V_2O_5

Vanadium pentoxide (V_2O_5) exhibits 21 calculated Raman active modes as precisely specified in Chapter 2.2.6.5. The characteristic V_2O_5 peaks occur up to a Raman shift of about 1000 cm^{-1} whereat the angle-bending modes cover the 200-500 cm^{-1} range and the bond stretching modes cover the interval of 500-1000 cm^{-1} . The peaks with less Raman shift than 200 cm^{-1} can be associated with vanadium atom displacements. All possible normal vibration modes and their corresponding frequency distribution and their assignments to particular atomic displacements are listed in Table 4. The values with an elevated b are not yet experimentally observed. [61]

The peak with the lowest frequency at 104 cm^{-1} belongs to the translational mode of the vanadium atom $Z(\text{V})$, $\delta(\text{O}_3\text{-V-O}_2)$ with an A_g symmetry. The peak with the highest intensity at 144 cm^{-1} belongs to the vanadium displacement $Y(\text{V})$, $\delta(\text{O}_3\text{-V-O}_2)$. It is a mixture of two signals including the shear motion of the ladders (B_{1g}) and the rotations of the ladders along their axes (B_{3g}). The peak at 195 cm^{-1} , $\delta(\text{O}_2\text{-V-O}_2)$, derives from

vanadium atoms oscillating along the x-axis (A_g and B_{3g}). The region between 200 cm^{-1} and 400 cm^{-1} correspond to x- and y- angle bending displacements of the O_1 atom (403 cm^{-1} and 282 cm^{-1}) and the z-displacements of O_{21} and O_{22} atoms (302 cm^{-1}). The peak at 480 cm^{-1} occurs because of V- O_3 -V bridge angle bending vibrations. Due to stretching vibrations, which involve x-displacements of $O_{2'}$ atoms, arises the Raman peak at 526 cm^{-1} (A_g mode). The peak at 700 cm^{-1} originates from the y-displacement of the O_2 atoms. The peak with the highest frequency of about 994 cm^{-1} is caused by z-displacements of the O_1 atom (A_g symmetry). [61]

Table 4: Symmetry and Frequency Distribution of Normal Vibrations of the V_2O_5 Lattice with Their Assignment to Particular Atomic Displacements, ^b not observed experimentally [61]

atomic displacement	assignment	A_g	B_{2g}
Z(O1)	$\nu(d_1)$	994	976^b
X(O3)	$\nu(d_2)$		848^b
X(O2')	$\nu(d_4)$	526	502^b
Z(O3)	$\delta(V-O_3-V)$	480	
X(O1)	$\rho(V=O1)$	403	350^b
Z(O2)		302	310^b
X(V)	$\delta(O_2-V-O_2)$	195	195
Z(V)	$\delta(O_3-V-O_2)$	104	143^b
atomic displacement	assignment	B_{1g}	B_{3g}
Y(O2)	$\nu(d_3)$	700	700
Y(O1)	$\rho(V=O1)$	282	282
Y(O3)	$\delta(O_2-V-O_2)$		220^b
Y(V)	$\delta(O_3-V-O_2)$	144	144

Raman measurements were taken from the pure V_2O_5 commercial powder and from V_2O_5 nanowires synthesised via the 1st and the 2nd synthesis, see Figure 74. All peak positions match well with the literature. In Table 5 are shown all measured Raman peaks, attributed to their atomic displacement and symmetry and compared with the data taken from the literature. [62] The intensities are normalised to the highest peak, which occurred in each spectrum.

One significant difference between the Raman spectrum of the commercial powder and the Raman spectra of the synthesised V_2O_5 nanowires is their intensity distribution. The commercial powder consists of a very intense Y(V) peak at a Raman shift of 145 cm^{-1} .

The two nearest peaks at 104 cm^{-1} and 198 cm^{-1} have a normalised intensity of only 7 % and 5 %. Compared to this the two Z(V) and X(V) peaks in the nanowires spectra around 102 cm^{-1} and 196 cm^{-1} exhibit a normalised intensity of about 26 % and 11 %. The second highest peaks in the nanowires spectra are the Z(O₁) peaks around 993 cm^{-1} with a normalised intensity of about 44 %. In the commercial powder spectrum have the Z(V) peak at 994 cm^{-1} and the Y(O₁) peak at 285 cm^{-1} the same intensity and are therefore both the second highest peak.

Another difference between the nanowires spectra and the commercial powder spectrum is the separation of the Z(O₃) peak around 480 cm^{-1} and the X(O₂) peak around 528 cm^{-1} . Those two peaks in the nanowires spectra are compared to those in the commercial powder spectrum broader and therefore overlap slightly. The two peaks at 481 cm^{-1} and 528 cm^{-1} in the commercial powder are smaller and better separated from each other.

A significant difference between the nanowires spectrum from the first synthesis and the one from the second synthesis cannot be seen.

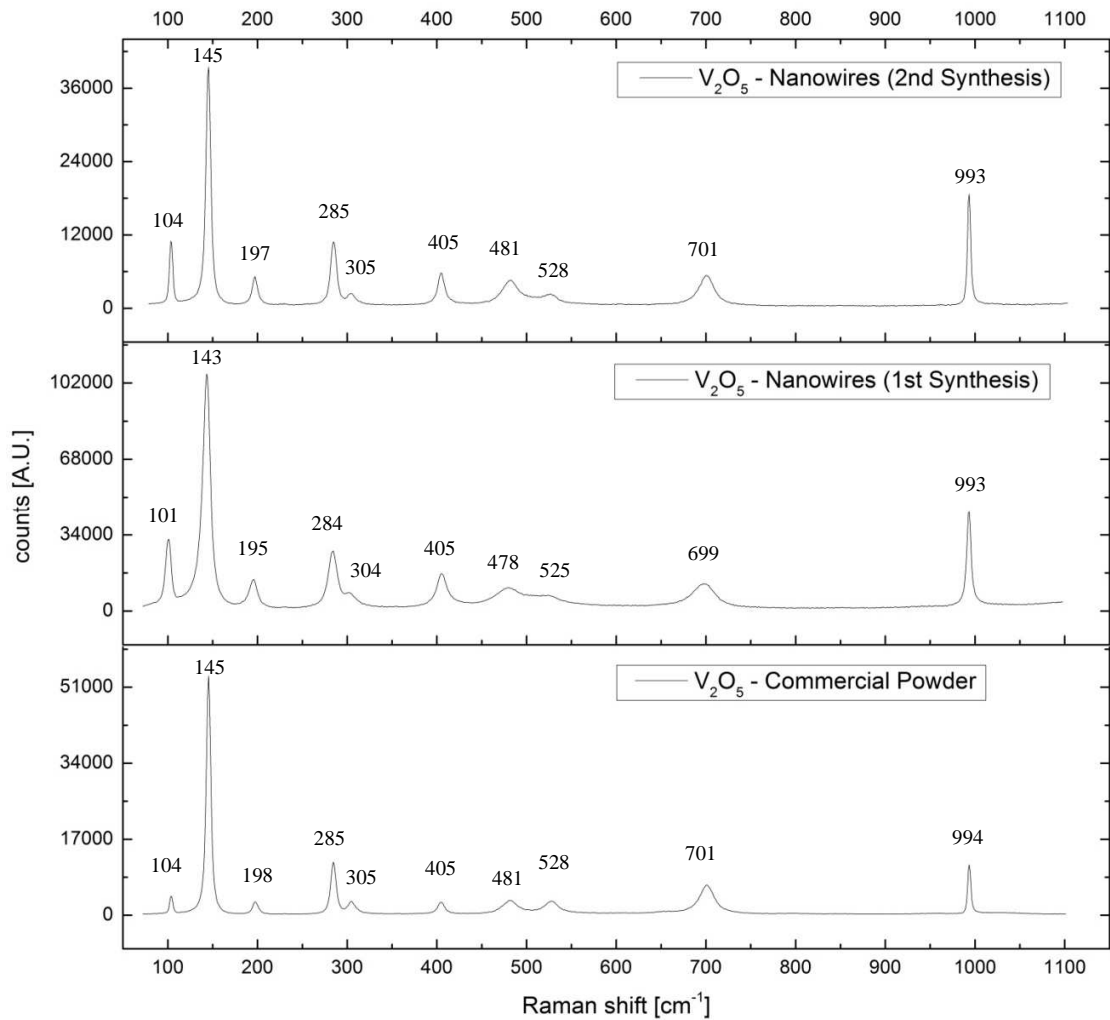


Figure 74: Raman measurement (He-Ne-laser: $\lambda=632.816$ nm) of V_2O_5 - commercial powder (1% laser power, 10 s exposure time), V_2O_5 - nanowires 1st synthesis (100% laser power, 10 s exposure time), V_2O_5 - nanowires 2nd synthesis (10 % laser power, 10 s exposure time)

Table 5: Raman Peaks of measured V_2O_5 samples with Raman shift and normalised intensities, literature data taken from [62]

Atomic displacement	Assignment	Symmetrie	Literature R. shift [cm ⁻¹]	Comm. Powder		Nanowires (1 st synth.)		Nanowires (2 nd synth.)	
				[cm ⁻¹]	[%]	[cm ⁻¹]	[%]	[cm ⁻¹]	[%]
Z(V)	$\delta(O_3-V-O_2)$	A _g	104	104	7	101	27	104	26
Y(V)	$\delta(O_3-V-O_2)$	B _{1g} , B _{3g}	144	145	100	143	100	145	100
X(V)	$\delta(O_2-V-O_2)$	A _g , B _{2g}	195	198	5	195	10	197	12
Y(O ₁)	$\rho(V=O_1)$	B _{1g} , B _{3g}	282	285	20	284	21	285	25
Z(O ₂)	-	A _g	302	305	4	304	2	305	3
X(O ₁)	$\rho(V=O_1)$	A _g	403	405	5	405	13	405	12
Z(O ₃)	$\delta(V-O_3-V)$	A _g	480	481	5	478	10	481	8
X(O ₂)	$\nu(d_4)$	A _g	526	528	4	525	7	528	2
Y(O ₂)	$\nu(d_3)$	B _{1g} , B _{3g}	700	701	11	699	7	701	11
Z(O ₁)	$\nu(d_1)$	A _g	994	994	20	993	41	993	46

4.3.2.3 Dry Electrodes

- Carbon

Single-crystal graphite crystallises in the D_{6h}^4 space group and exhibits two Raman active $2E_{2g}$ modes, which appear at 42 and 1575 cm⁻¹. The one with the lower frequency is difficult to observed, because of its proximity to the lasers Rayleigh line. The higher frequency band (G-band) is a very strong significant peak originating from the relative motion of sp² carbon atoms in rings and chains. Additionally a lot of graphitic materials show another disorder induced A_{1g} line, also called D-band at about 1350 cm⁻¹, due to breathing motions of sp² atoms in rings at edge planes and defects in the graphene sheet. [61, 101]

In Figure 75 is shown a Raman spectrum measured at a dry electrode surface made of 85 wt. % Super C 65 and 15 wt. % PVdF. The G-band was measured at 1578 cm⁻¹ and the D-band at 1335 cm⁻¹. At 1618 cm⁻¹ can be seen a little shoulder from the strong G-band. This peak is called D^I band and is part of the D-band appearance. [102]

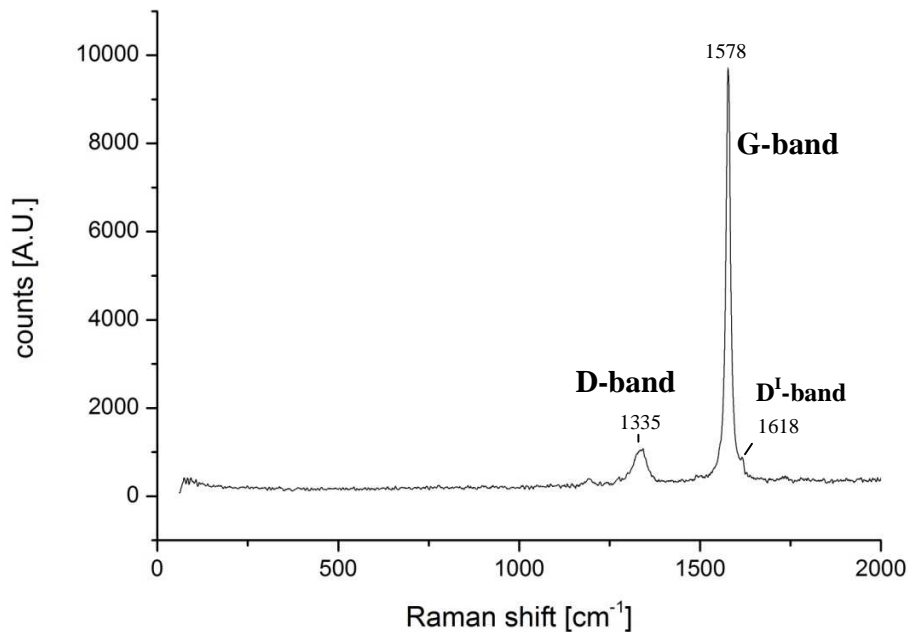


Figure 75: Raman spectrum of a dry carbon electrode (85 wt. % Super C 65, 15 wt. % PVdF), laser power: 10 %, exposure time: 10 s, 10 accumulations

- TiO_2

Tetragonal TiO_2 anatase crystallises in the D_{4h}^{19} space group and therefore, according to the point group analysis, has six expected Raman active modes, but only five can be measured above a temperature of 73 K. The bands at 144 cm^{-1} , 198 cm^{-1} and 398 cm^{-1} relate to O-Ti-O bending and the bands at 518 cm^{-1} and 639 cm^{-1} correspond to Ti-O stretching. [61, 103]

In Figure 76 is plotted a Raman measurement of a dry TiO_2 electrode (60 wt. % TiO_2 , 20 wt. % Super C 65, 20 wt. % PVdF). The significant peaks were occurred at a frequency of 154 cm^{-1} , 204 cm^{-1} , 399 cm^{-1} , 501 cm^{-1} and 618 cm^{-1} and therefore are slightly different to the literature data. The peaks relating to the bending modes were measured at higher frequencies whereas the peaks corresponding to the stretching modes occurred at lower frequencies.

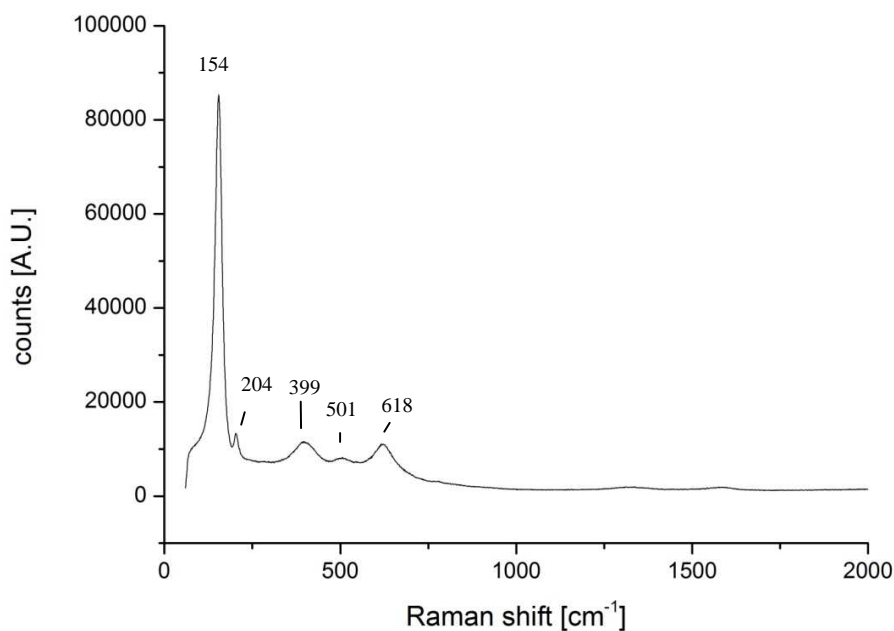


Figure 76: Raman spectrum of a dry TiO₂ electrode (60 wt. % TiO₂, 20 wt. % Super C 65, 20 wt. % PVdF), laser power: 50 %, exposure time: 10 s

- $Li_4Ti_5O_{12}$

$Li_4Ti_5O_{12}$ has the factor group $Fd\bar{3}m$ and by using the factor group analysis for normal $A[B_2]O_4$ spinel-type compounds five Raman active modes are expected, namely A_{1g} , E_g and $3F_{2g}$. Six Raman bands at 160 cm^{-1} , 235 cm^{-1} , 335 cm^{-1} , 430 cm^{-1} , 675 cm^{-1} and 740 cm^{-1} were observed at which the peaks at 235 cm^{-1} , 430 cm^{-1} and 675 cm^{-1} had the highest intensity. The two peaks with the highest frequencies are proposed to arise from Ti-O bond vibrations in TiO_6 octahedra. The two peaks in the middle of the frequency range are supposed to be the stretching vibrations of the Li-O bonds in LiO_4 and LiO_6 polyhedra and the two peaks with the lowest frequencies are bending vibrations of O-Ti-O and O-Li-O bonds. [61]

In Figure 77 is shown a Raman spectrum of a $Li_4Ti_5O_{12}$ electrode (82 wt. % $Li_4Ti_5O_{12}$, 8 wt. % Super C 65, 10 wt. % PVdF). Three significant peaks could be observed at a frequency of 233 cm^{-1} , 428 cm^{-1} and 672 cm^{-1} . Two other peaks occurred at 335 cm^{-1} and 740 cm^{-1} .

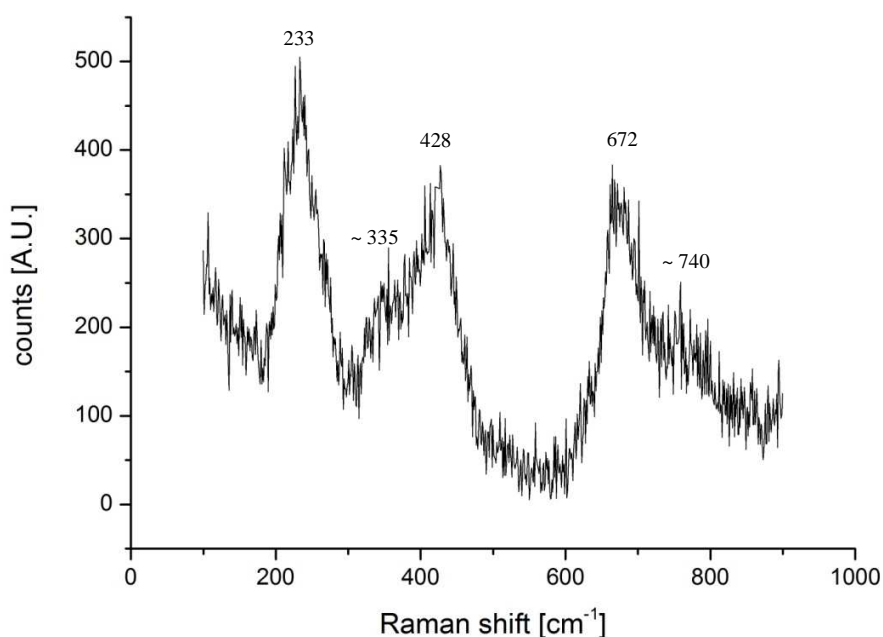


Figure 77: Raman spectrum of a dry $\text{Li}_4\text{Ti}_5\text{O}_{12}$ electrode (82 wt. % $\text{Li}_4\text{Ti}_5\text{O}_{12}$, 8 wt. % Super C 65, 10 wt. % PVdF), laser power: 1%, exposure time: 300 s

4.3.2.4 *In situ* Raman Measurements

- *Graphite – Lithium Battery*

In Figure 78 is plotted an *in situ* Raman measurement showing the initial lithium intercalation into a graphite electrode (70 wt. % SFE 6 Graphite, 30 wt. % PVDF, prepared in acetone). The laser power was set to 10 %, the exposure time to 60 s and it was measured at a Raman shift range of 1200 - 1800 cm^{-1} . The battery cell was cycled with a C-range of C/15 and the voltage limits were set to 0.01 V and 1.5 V. The corresponding galvanostatic measurement is shown in Figure 80. After discharge the battery was subsequently charged again and the intercalated lithium was de-intercalated, see the relating Raman measurement in Figure 79.

All Raman spectra are baseline corrected to allow clear visualisation. In general has to be noted that the Raman signal degrades as the cycle number increases. The signal to noise ratio becomes poorer, because of an increased background base line. The reason for this behaviour is the increasing fluorescence produced by degradation products of the electrolyte. Therefore Raman measurements are best undertaken during the first cycle.

During lithium intercalation into graphite the G-band shifted from 1580 cm^{-1} ($x=0$) to 1591 cm^{-1} ($x=0.29$). This behaviour can be attributed to the beginning of lithium insertion, which starts at a potential of about 0.55 V . [104] The D band at 1333 cm^{-1} and also the D^I band, which was measured at 1615 cm^{-1} , started to decrease from a potential of about 1 V onwards and was completely vanished at a potential of about 0.5 V . Due to the SEI formation starting at a potential of about 0.9 V in EC containing electrolytes, it is believed that the co-intercalation of lithium with EC, which occurs during the formation of a stable SEI film, disrupts the Raman D-band and causes its weakness. [104]

At a x value of 0.30 in Li_xC_6 and a potential of 0.21 V (vs. Li/Li^+) the G-band split into two peaks at 1574 cm^{-1} ($\text{E}_{2g2}(\text{i})$) and 1600 cm^{-1} ($\text{E}_{2g2}(\text{b})$) [61], which is related to a change from the random distribution of lithium ions into a more compact distribution in the staged compound. [104] By continuing of the discharge process the $\text{E}_{2g2}(\text{i})$ peak shifted towards 1571 cm^{-1} whereat the $\text{E}_{2g2}(\text{b})$ one kept constant. At a composition of $\text{Li}_{0.51}\text{C}_6$ all peaks completely vanished.

During subsequently charge of the lithium battery the $\text{E}_{2g2}(\text{b})$ appeared at a potential of about 0.17 V at a Raman shift of 1595 cm^{-1} and the corresponding $\text{E}_{2g2}(\text{i})$ band appeared at 0.19 V at a shift of 1572 cm^{-1} . The reunion of those two peaks to the G-band happened at a potential of about 0.26 and a Raman shift of 1585 cm^{-1} , which shifted towards 1577 cm^{-1} during the last charge steps.

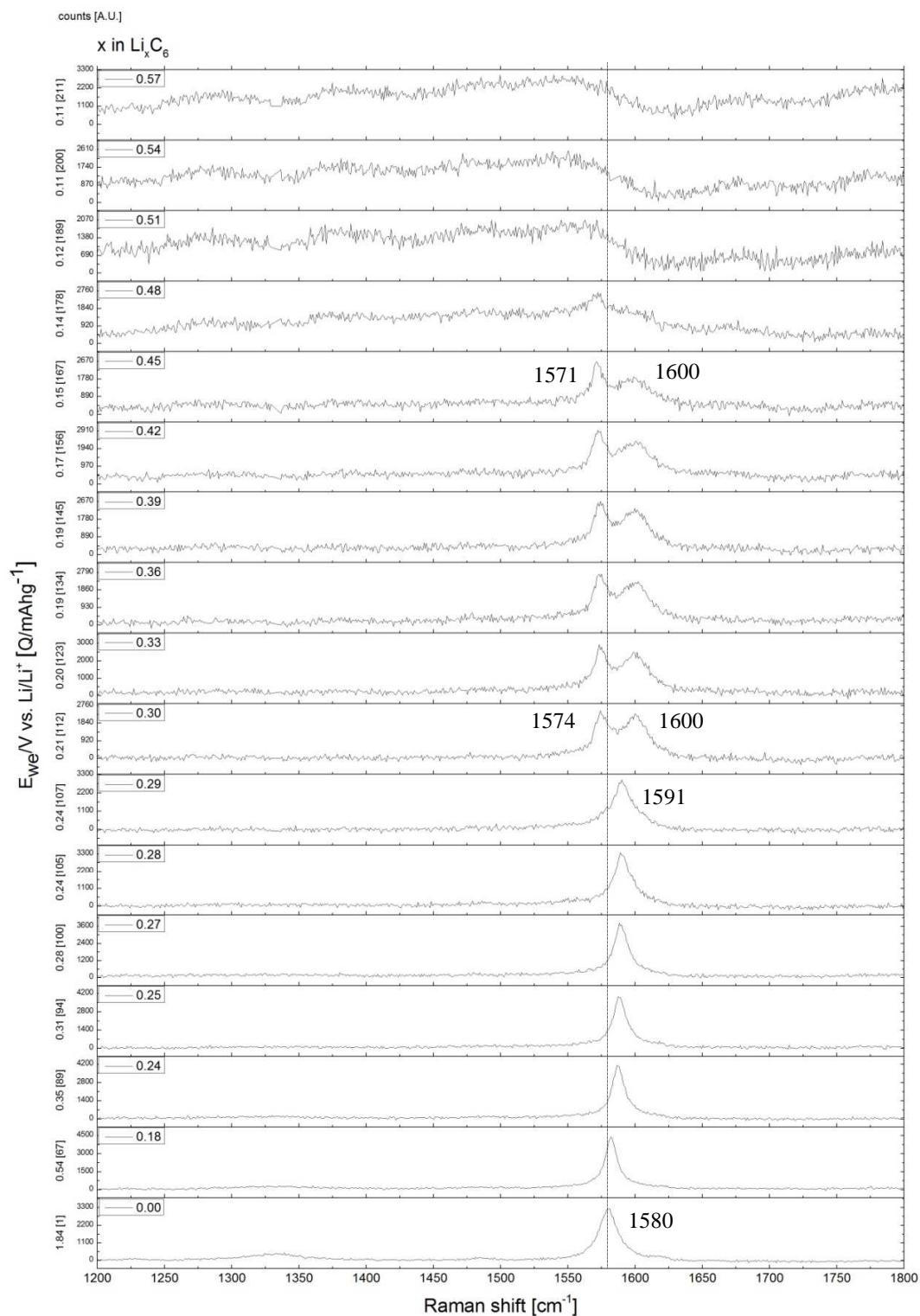


Figure 78: *In situ* Raman spectrum, lithium intercalation into graphite electrode (70 wt. % SFE 6 Graphite, 30 wt. % PVDF, prepared in acetone), laser power: 10 %, exposure time: 60 s, Raman shift range: 1200 – 1800 cm^{-1} , C-range: C/15

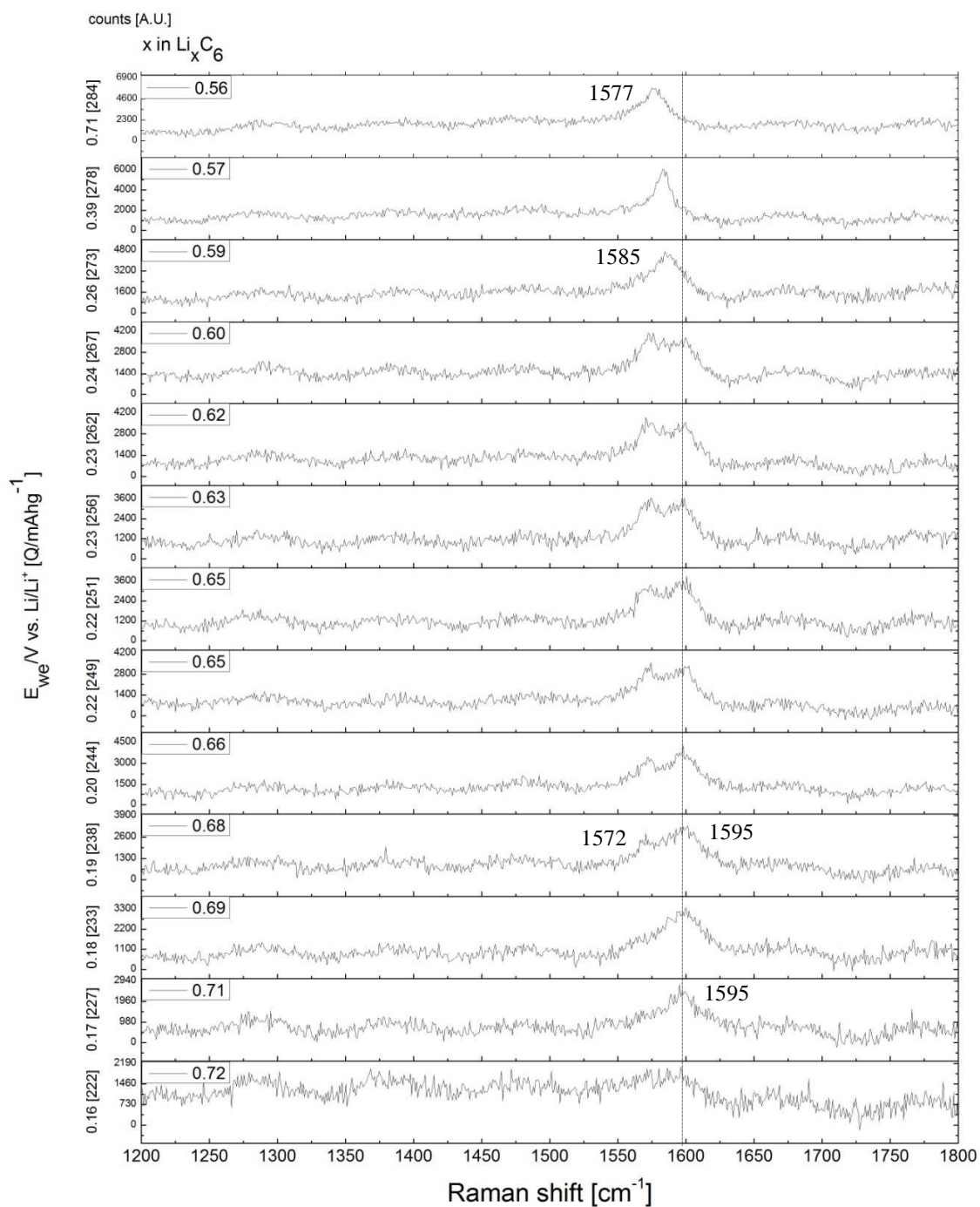


Figure 79: *In situ* Raman spectrum, lithium de-intercalation from graphite electrode (70 wt. % SFE 6 Graphite, 30 wt. % PVDF, prepared in acetone), laser power: 10 %, exposure time: 60 s, Raman shift range: 1200 – 1800 cm^{-1} , C-range: C/15

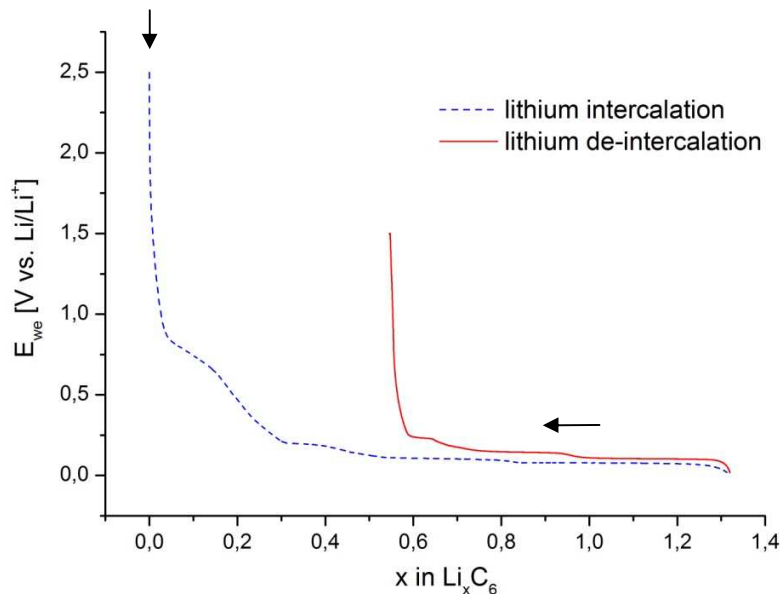


Figure 80: Galvanostatic cycling of graphite electrode (70 wt. % SFE 6 Graphite, 30 wt. % PVDF, prepared in acetone) for *in situ* Raman measurement, with lithium metal as counter electrode and DMC/EC 1:1 + 1 M LiClO₄ as electrolyte, cycled with a C-range of C/15, voltage limits: 0.01 V and 1.5 V (vs. Li/Li⁺)

- *TiO₂ – Lithium Battery*

Figure 81 shows an *in situ* Raman measurement of an TiO₂ electrode (40 wt. % TiO₂, 30 wt. % Super C 65, 30 wt. % PVDF, prepared in acetone) cycled against a lithium metal counter electrode with an electrolyte made of a solution of EC:DMC 1:1 including 1 M LiClO₄. The cell was cycled with a C rate of C/15. The corresponding galvanostatic measurement can be seen in Figure 83.

At the beginning of the discharge process the Raman spectrum exhibited one significant O-Ti-O bending peak at 150 cm⁻¹ and three broad Ti-O stretching peaks at about 395 cm⁻¹, 515 cm⁻¹ and 624 cm⁻¹, related to the literature see Chapter 4.3.2.3. During lithium intercalation the intensity of the O-Ti-O bending peak decreased and it shifted slightly from 150 cm⁻¹ to 153 cm⁻¹. At a potential of about 1.71 V this peak completely vanished, but two new peaks at 168 cm⁻¹ and 234 cm⁻¹ occurred instead, which are presumably caused by splitting up of the O-Ti-O bending peak. A third new peak at about 345 cm⁻¹ rose from 1.79 V onwards. The two Ti-O stretching peaks at 395 cm⁻¹ and 634

cm^{-1} shifted during lithium intercalation closer together towards 529 cm^{-1} and 629 cm^{-1} . At a potential of about 1.49 V and a composition of $\text{Li}_{1.03}\text{TiO}_2$ the Raman signal became very weak and all peaks changed over into very broad signals accompanied with background noise.

During the charge process the intercalated lithium got de-intercalated again, see Figure 82. In these spectra the two peaks, caused by the Ti-O bending peak split up, increased while they shift from about 250 cm^{-1} towards 187 cm^{-1} and 241 cm^{-1} at a potential of ca. 1.93 V. At a potential of 2.04 V and an x value of 0.83 the two peaks combined at a Raman shift of about 150 cm^{-1} . The peak at 350 cm^{-1} does not shift at all during delithiation. Also the two O-Ti-O stretching peaks occurred again and increased their intensity at a Raman shift of about 538 cm^{-1} and 630 cm^{-1} .

In the literature is claimed that the experimental Raman data in addition with lattice dynamics simulation provide different important information about the lithium intercalation into TiO_2 [61]:

- The Li ions are located at different multiple positions in the octahedral interstices of the orthorhombic structure, hypothesised because of peak splitting and multiple Raman bands, which cover a wide wavenumber range
- The splitting up of the low frequency peak gives rise to the presumption that the Li interactions take place with the TiO_2 lattice
- Li positions with short Li-O distances were found to be responsible for high wavenumber features above 800 cm^{-1}
- Strong Li-O bonds, which can't break within the recharge (delithiation/reoxidation) process, correspond to several modes in the high frequency range and therefore can explain the partial electrochemical rechargeability

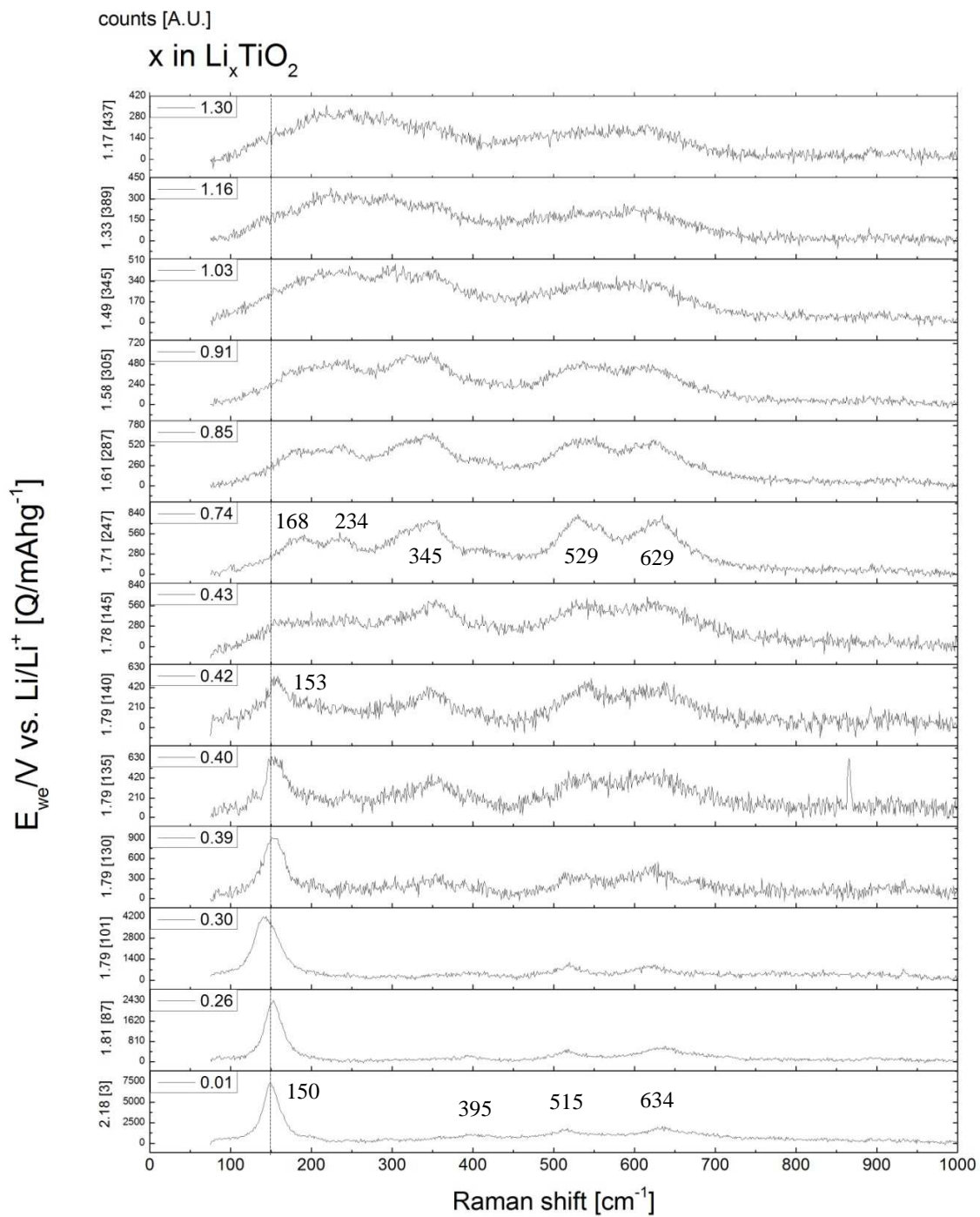


Figure 81: *In situ* Raman spectrum, lithium intercalation into TiO_2 electrode (40 wt. % TiO_2 , 30 wt. % Super C 65, 30 wt. % PVDF, prepared in acetone), laser power: 0.5 %, exposure time: 180 s, Raman shift range: 75 – 1000 cm^{-1} , C-range: C/15

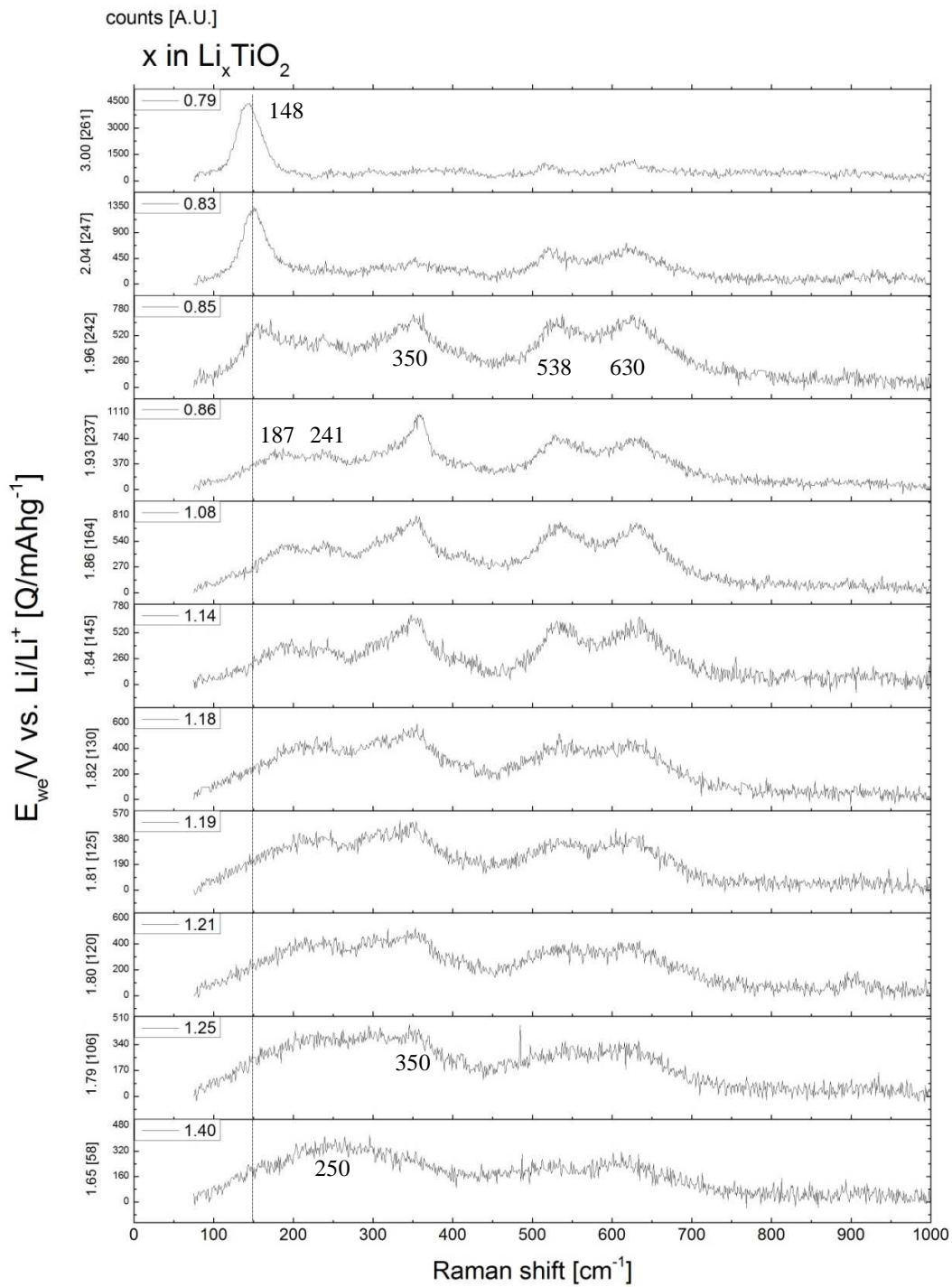


Figure 82: *In situ* Raman spectrum, lithium de-intercalation from TiO_2 electrode (40 wt. % TiO_2 , 30 wt. % Super C 65, 30 wt. % PVDF, prepared in acetone), laser power: 0.5 %, exposure time: 180 s, Raman shift range: 75 – 1000 cm^{-1} , C-range: C/15

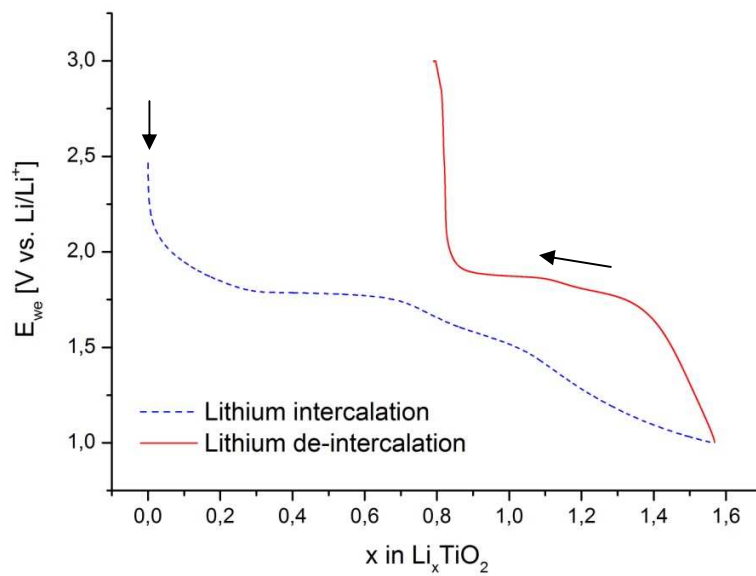


Figure 83: Galvanostatic cycling of TiO_2 electrode (40 wt. % TiO_2 , 30 wt. % Super C 65, 30 wt. % PVDF, prepared in acetone) for *in situ* Raman measurement, with lithium metal as counter electrode and DMC/EC 1:1 + 1 M $LiClO_4$ as electrolyte, cycled with a C-range of C/15, voltage limits: 1 V and 3 V (vs. Li/Li^+)

- $\text{Li}_4\text{Ti}_5\text{O}_{12}$ – Lithium Battery

The intercalation of lithium into lithium titanate ($\text{Li}_4\text{Ti}_5\text{O}_{12}$) occurs at a potential of about 1.5 V (vs. Li/Li^+), see galvanostatic measurement in Figure 85. During this cyclic voltammetry *in situ* Raman measurements were taken, see Figure 84. First of all has to be mentioned, that it was challenging to obtain a good Raman signal from the *in situ* cell, due to background noise. At the beginning was measured a Raman spectrum with five peaks at a Raman shift of 160 cm^{-1} , 233 cm^{-1} , 357 cm^{-1} , 426 cm^{-1} , 674 cm^{-1} and 763 cm^{-1} . Unfortunately the spectrum did not change significantly during discharge. The only difference which can be noticed between the first and the last spectrum is an intensity loss of the Raman signal. The electrochemistry of the *in situ* cell worked well, according to the big flat intercalation plateau at 1.5 V vs. Li/Li^+ within the galvanostatically measurement, sees Figure 85. Therefore it is likely the case that the measured particle was not involved into the electrochemistry. Perhaps it was just not well enough contacted to the carbon particles, which provide a good electric contact between the active material and the current collector. It was very hard to get a suitable Raman signal for an *in situ* measurement and every time when the signal was useful the particle seemed to be apart from the active electrode material and the signal did not change during charge or discharge. During the short time of this project it was not possible to measure changing *in situ* Raman spectra, but further work is under progress.

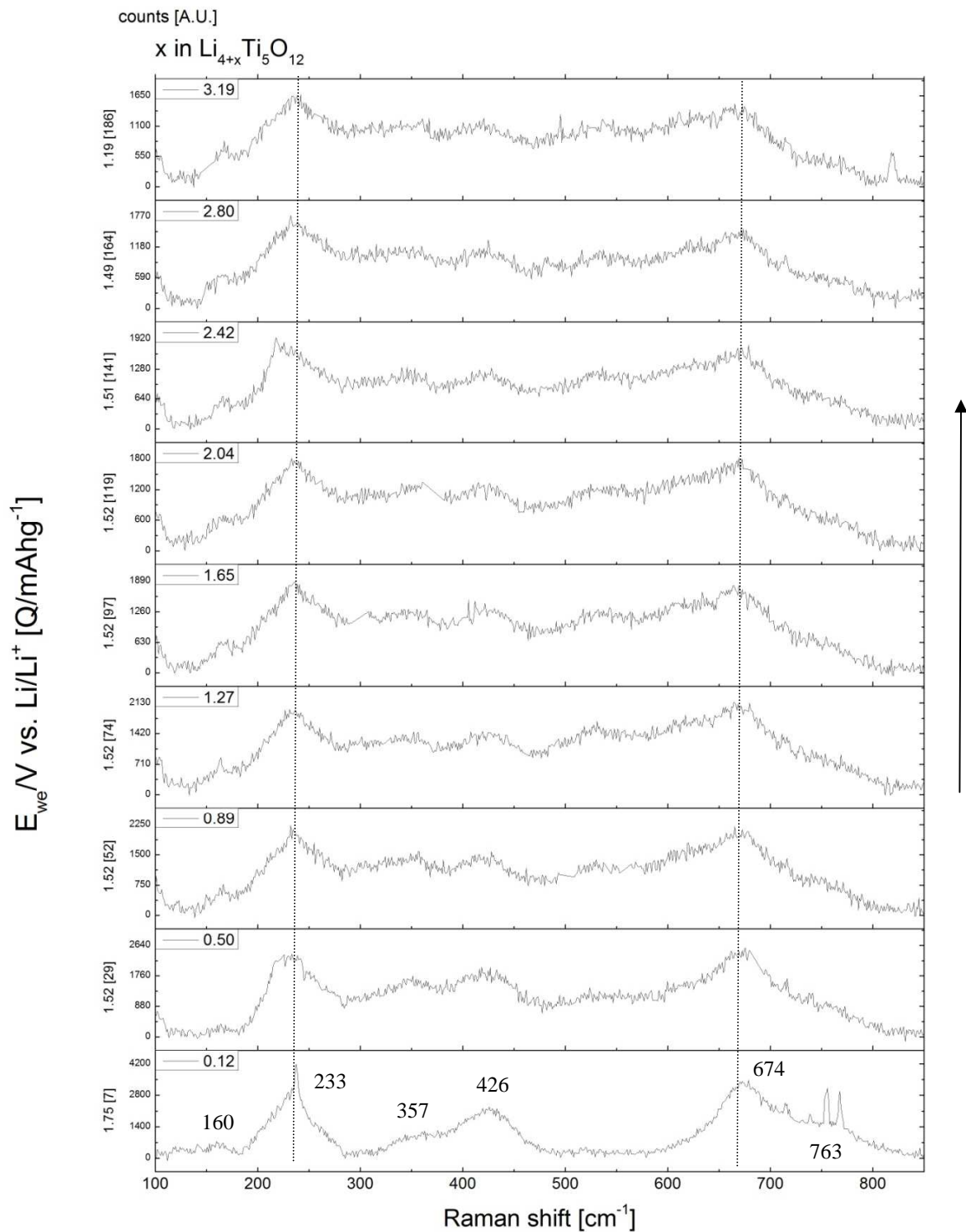


Figure 84: *In situ* Raman spectrum, lithium intercalation into $\text{Li}_4\text{Ti}_5\text{O}_{12}$ electrode (79 wt. % $\text{Li}_4\text{Ti}_5\text{O}_{12}$, 10 wt. % Super C 65, 11 wt. % PVDF, prepared in NMP), laser power: 1%, exposure time: 600 s, Raman shift range: 100 – 850 cm^{-1} , C-range: C/9

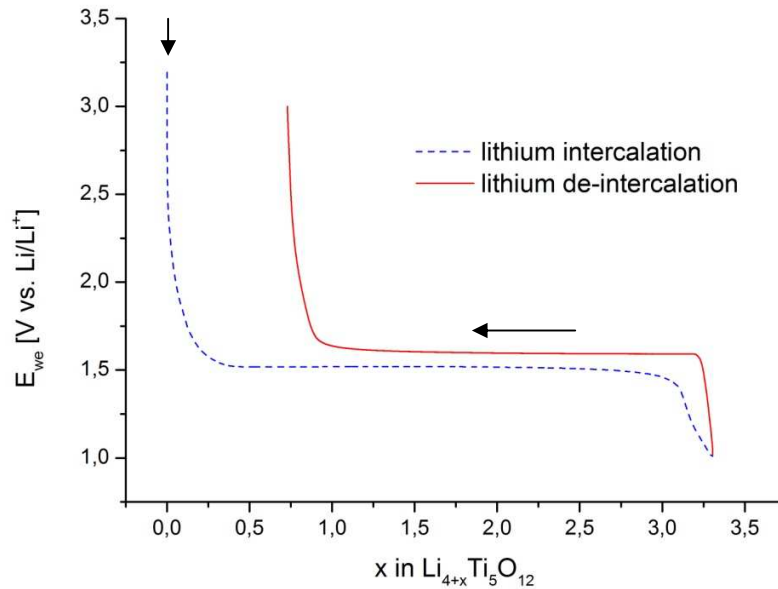


Figure 85: Galvanostatic cycling of $\text{Li}_4\text{Ti}_5\text{O}_{12}$ electrode (79 wt. % $\text{Li}_4\text{Ti}_5\text{O}_{12}$, 10 wt. % Super C 65, 11 wt. % PVDF, prepared in NMP) for *in situ* Raman measurement, with lithium metal as counter electrode and DMC/EC 1:1 + 1 M LiPF_6 as electrolyte, cycled with a C-range of C/9, voltage limits: 1 V and 3 V (vs. Li/Li^+)

- V_2O_5 – Lithium Battery

Commercial Powder Electrodes

In Figure 86 an *in situ* Raman measurement of an electrode made of the commercial powder V_2O_5 is shown. The cell was stacked with a lithium metal counter electrode and a working electrode made by the separator preparation technique, see 3.3.2.2. The electrolyte was a solution of EC:DMC including 1 M LiPF_6 . The cell was galvanostatically cycled down to a potential of 1.8 V with a C-rate of C/4. It was measured with a laser power of 1 % and an exposure time of 60 s at the beginning. After couple of measurement the exposure time was set step by step to higher values, due to weaker Raman signals. In the first measured spectrum occurred ten different peaks at a Raman shift of 103 cm^{-1} , 145 cm^{-1} , 197 cm^{-1} , 284 cm^{-1} , 304 cm^{-1} , 405 cm^{-1} , 480 cm^{-1} , 529 cm^{-1} , 700 cm^{-1} and 994 cm^{-1} . These peaks match well with the literature for V_2O_5 , see Chapter 4.3.2.2. The peak at 145 cm^{-1} exhibits the highest intensity and is therefore

neglected in Figure 86, at which the y scale is zoomed in to provide a better visualization of the smaller peaks. At a potential of about 3.23 V the peak at a Raman shift of 994 cm^{-1} started to decrease in intensity while another peak at a Raman shift of 981 cm^{-1} slowly appeared and increased its intensity. This split up happened until the first peak completely vanished at a potential of about 3.12 V and an x-value of 0.33, see Figure 87 on the left side. This appearance is ended as soon as the δ phase is completely formed. During this phase transformation of the α phase to the ϵ and δ phase also the peaks at 284 cm^{-1} and 304 cm^{-1} changed. They did not shift during lithium intercalation, but their intensity changed to equality. The peak with the highest intensity, which occurred at a potential of 145 cm^{-1} also did not shift, but lost its intensity continuously until it completely disappeared as soon as the entire δ phase was formed, see Figure 87 on the right side. The peak at 700 cm^{-1} got broader during lithium intercalation. The intensity loss of the peaks can be related to the increase of disorder within the V_2O_5 layers. [61] The first measured Raman spectrum of the two phases δ and γ at a potential of 2.32 V and a composition of $\text{Li}_{0.72}\text{V}_2\text{O}_5$ exhibits four broad peaks at a Raman shift of 430 cm^{-1} , 531 cm^{-1} , 630 cm^{-1} and 700 cm^{-1} . The occurred peaks around a Raman shift of 900 cm^{-1} can be likely related to electrolyte background signals and are therefore also neglected in the zoom range. By reaching the γ and ω phase no significant peaks could be seen anymore. In Figure 88 is shown the corresponding galvanostatic cycling measurement of the commercial V_2O_5 powder lithium battery. The different phases, which occur during lithium intercalation, are marked.

After all the spectra are similar to *in situ* Raman measurements of V_2O_5 thin film electrodes, which are displayed in the literature [73], suggesting the insertion mechanism is similar in this nanosized material.

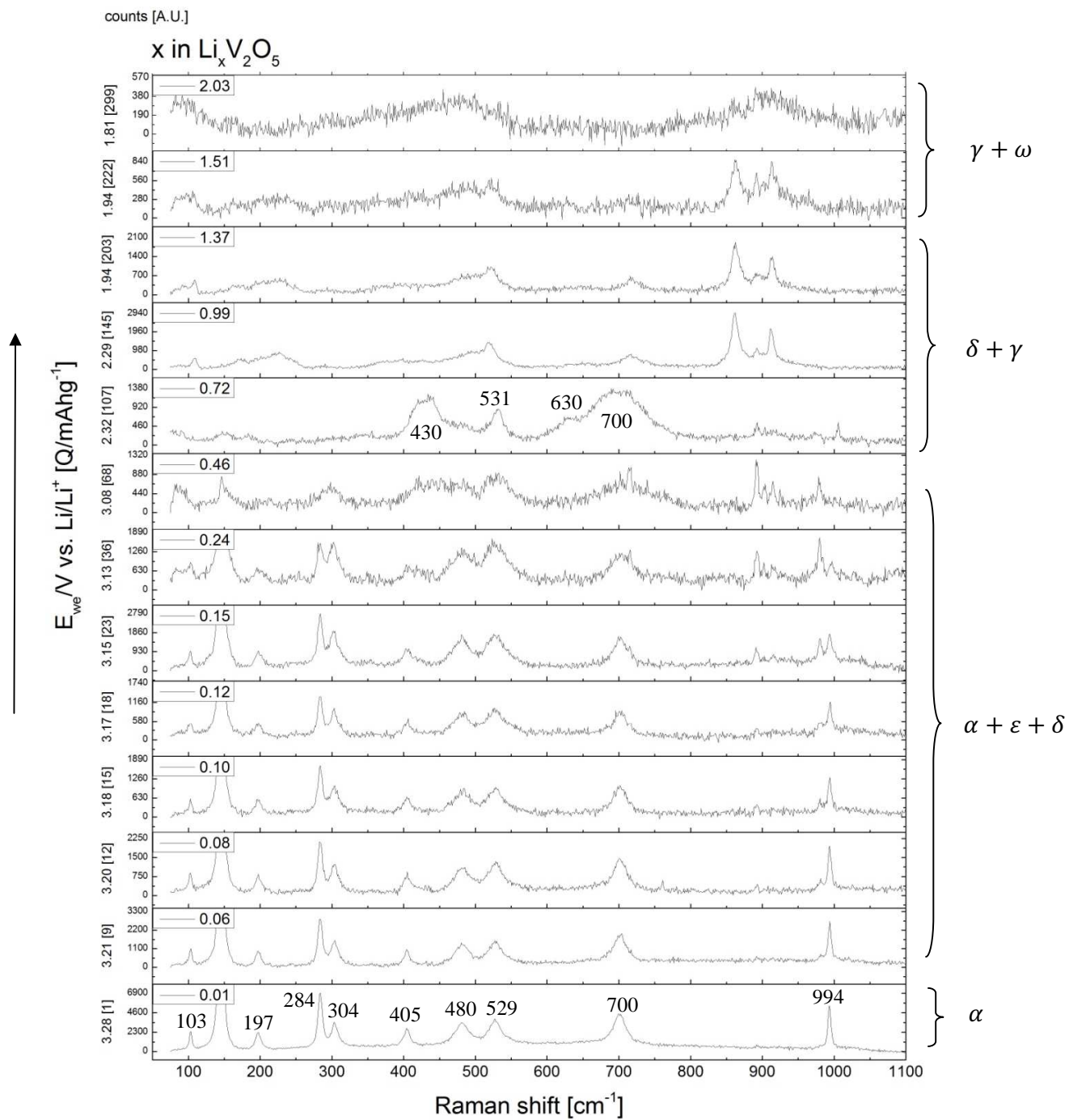


Figure 86: *In situ* Raman spectrum, lithium intercalation into V_2O_5 commercial powder electrode (filter paper preparation technique), laser power: 1%, exposure time: 60 s – 300 s, Raman shift range: 75 – 1100 cm^{-1} , C-range: C/4, voltage limit: 1.8 V, y-scale zoomed in

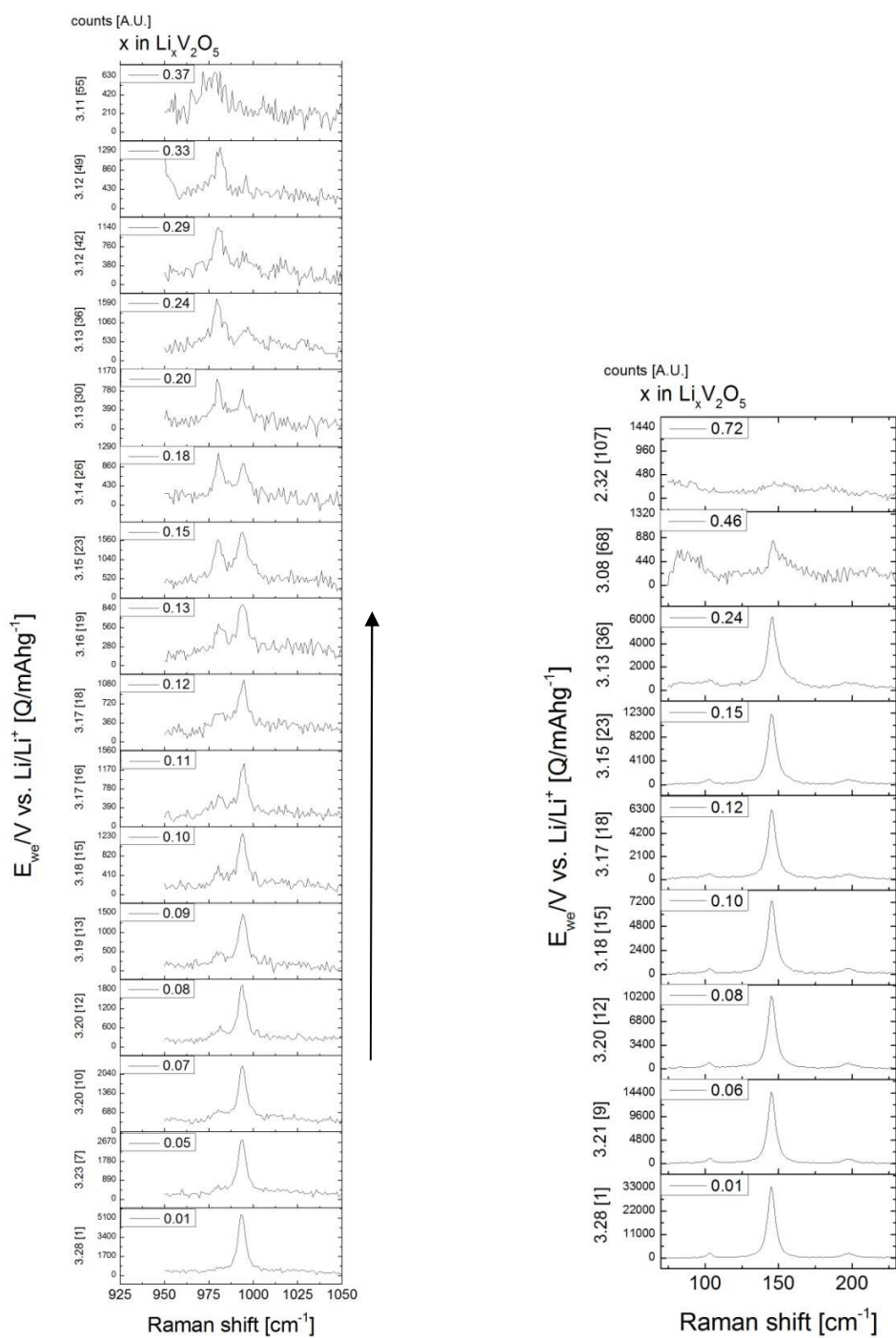


Figure 87: *In situ* Raman spectrum, lithium intercalation into V_2O_5 commercial powder electrode (filter paper preparation technique), laser power: 1%, exposure time: 60 s, Raman shift range: left: 950 cm $^{-1}$ – 1050 cm $^{-1}$, right: 70 cm $^{-1}$ – 230 cm $^{-1}$, voltage limit: 1.8 V (vs. Li/Li^+)

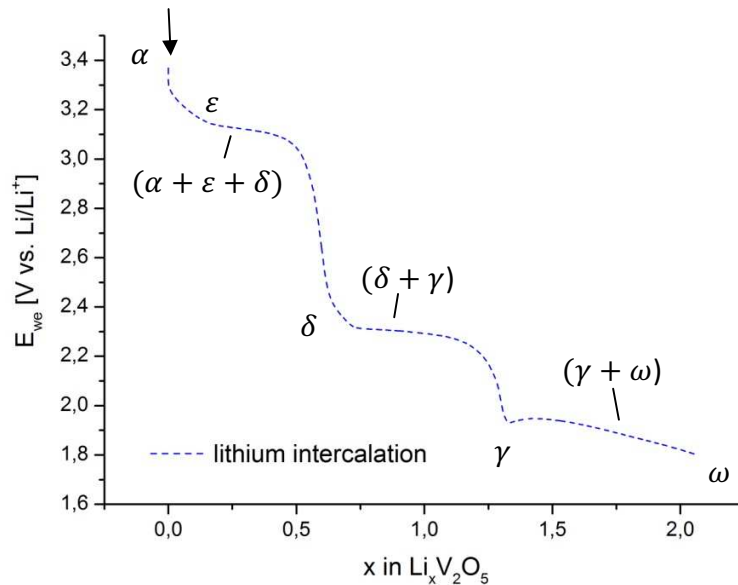


Figure 88: Galvanostatic cycling of commercial V_2O_5 powder electrode (separator preparation technique) for *in situ* Raman measurement, with lithium metal as counter electrode and DMC/EC 1:1 + 1 M $LiPF_6$ as electrolyte, cycled with a C-range of C/4, voltage limit: 1.8 V (vs. Li/Li^+)

Figure 89 displays the galvanostatic measurement of an *in situ* Raman measurement of a commercial powder V_2O_5 working electrode made by the separator preparation technique. The battery was discharged down to a potential of 2 V with a C-range of C/4. In this diagram it is possible to distinguish between the transformation of the α phase to the ϵ phase, which is marked by a flat plateau at 3.25 V, and the further transformation to the δ phase, marked by a flat plateau at 3.1 V can be clearly seen in this diagram. The formation of the γ phase occurred at a potential of about 2.3 V.

The corresponding *in situ* Raman spectra are shown in Figure 90. For better visualisation of the smaller peaks, the peak with the highest intensity at 145 cm^{-1} is neglected in this diagram. This peak lost its intensity within the discharge process until it vanished at a potential of about 3.10 V with the formation of the δ phase. The characteristic peaks of the beginning α phase occurred at a Raman shift of 104 cm^{-1} , 145 cm^{-1} , 196 cm^{-1} , 284 cm^{-1} , 305 cm^{-1} , 404 cm^{-1} , 481 cm^{-1} , 526 cm^{-1} , 699 cm^{-1} and 993 cm^{-1} . During discharge the peak at 104 cm^{-1} lost intensity and shifted towards 94 cm^{-1} until is disappeared out of the measuring range. The peak at 196 cm^{-1} got broader and shifted towards 202 cm^{-1} where it

completely vanished at a potential of 3.20 V. The peaks at 284 cm^{-1} , 305 cm^{-1} , 404 cm^{-1} , 481 cm^{-1} and 526 cm^{-1} did not shift significantly. They lost their intensity and got broader during the measurement. The peak at 699 cm^{-1} shifted slightly to a higher Raman shift of about 705 cm^{-1} . The significant peak split of the 993 cm^{-1} peak started at a potential of about 3.23 V and ended 3.11 V, whereat the second peak exhibited a Raman shift of about 981 cm^{-1} . The δ phase was marked by 5 peaks at a Raman shift of 296 cm^{-1} , 430 cm^{-1} , 530 cm^{-1} , 630 cm^{-1} and 710 cm^{-1} . During the formation of the γ phase disappeared the peak at 296 cm^{-1} .

In Figure 91 is shown the peak split at a Raman shift around 1000 cm^{-1} in more detail. On the left side is shown the transformation within the potential of 0 V and 3.12 V, where the significant peak split occurred. On the right side is shown the further discharge down to a potential of about 2.25 V. During this discharge process the γ phase was build and the peak at 980 cm^{-1} lost its intensity, whereat another peak occurred at a potential of 2.30 V and a Raman shift of 1005 cm^{-1} .

Figure 92 displays the de-intercalation process of lithium from the commercial V_2O_5 powder electrode up to a potential of 3.5 V. During this charge process the peak at 1005 cm^{-1} disappeared and the peak at 980 cm^{-1} appeared, but did not split up anymore. The characteristic α spectrum could not be completely established anymore. This shows the irreversible phase transformation of the γ phase.

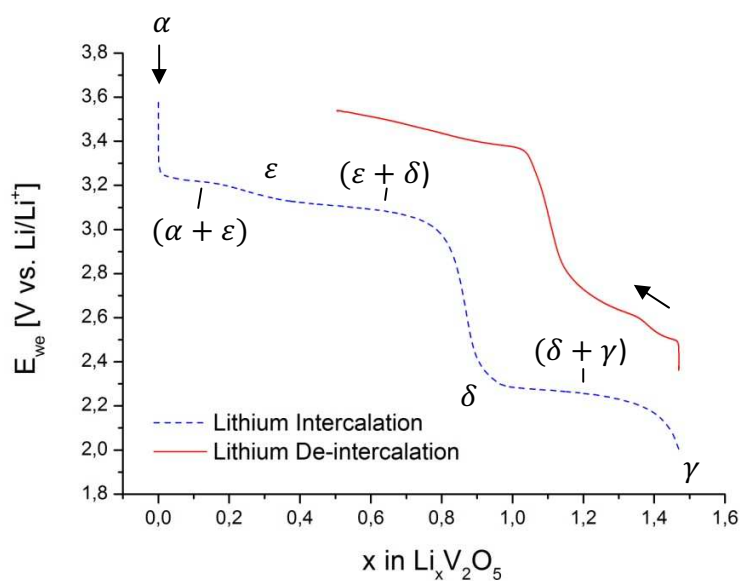


Figure 89: Galvanostatic cycling of commercial V_2O_5 powder electrode (separator preparation technique) for *in situ* Raman measurement, with lithium metal as counter electrode and DMC/EC 1:1 + 1 M LiPF_6 as electrolyte, cycled with a C-range of C/4, voltage limit: 2 V and 3.6 V (vs. Li/Li^+)

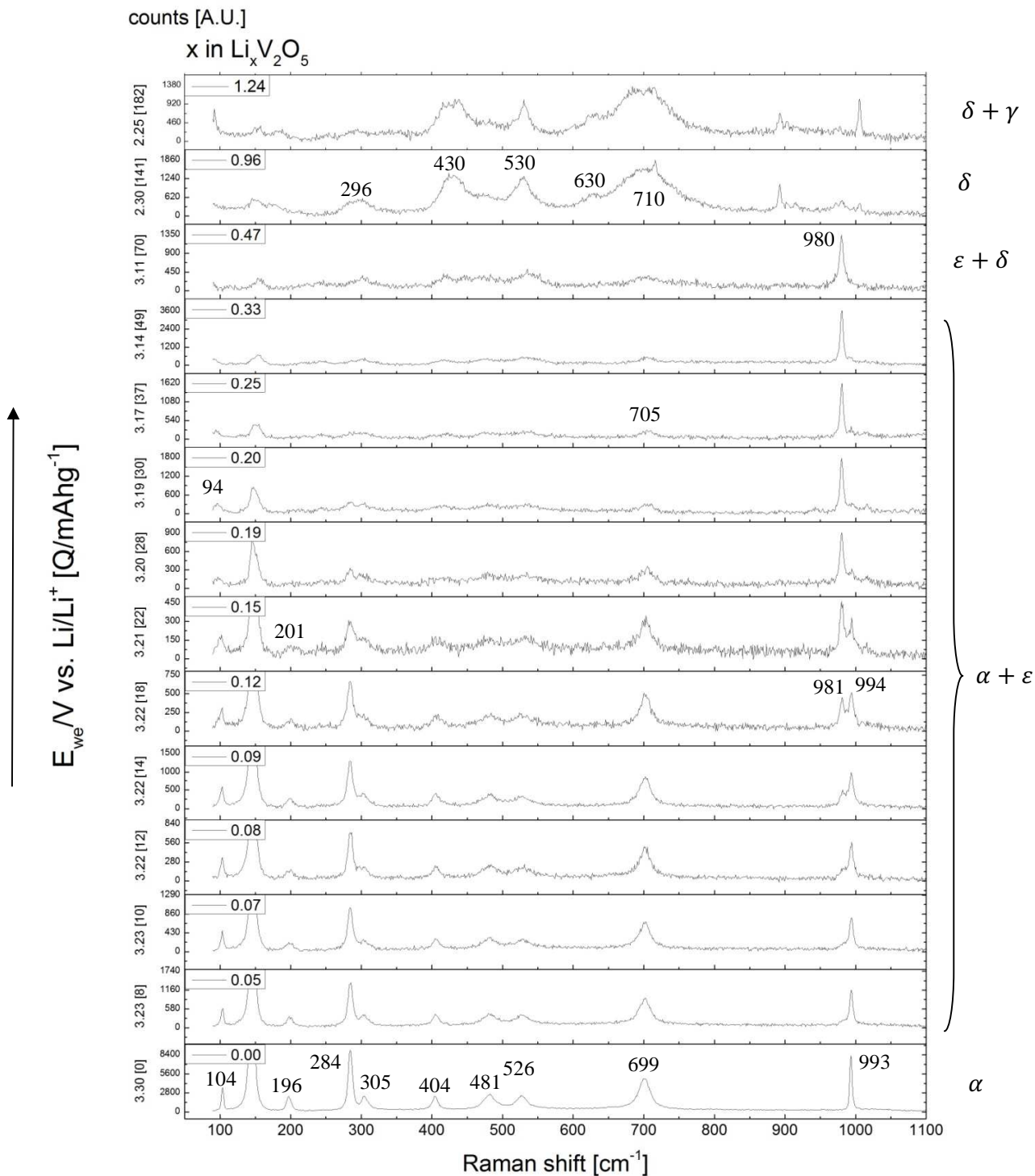


Figure 90: *In situ* Raman spectrum, lithium intercalation into V_2O_5 commercial powder electrode (separator preparation technique), laser power: 0.5 – 1 %, exposure time: 10 s – 300 s, Raman shift range: 90 – 1100 cm^{-1} , C-range: C/4, voltage limit: 2 V (vs. Li/Li^+), y-scale zoomed in

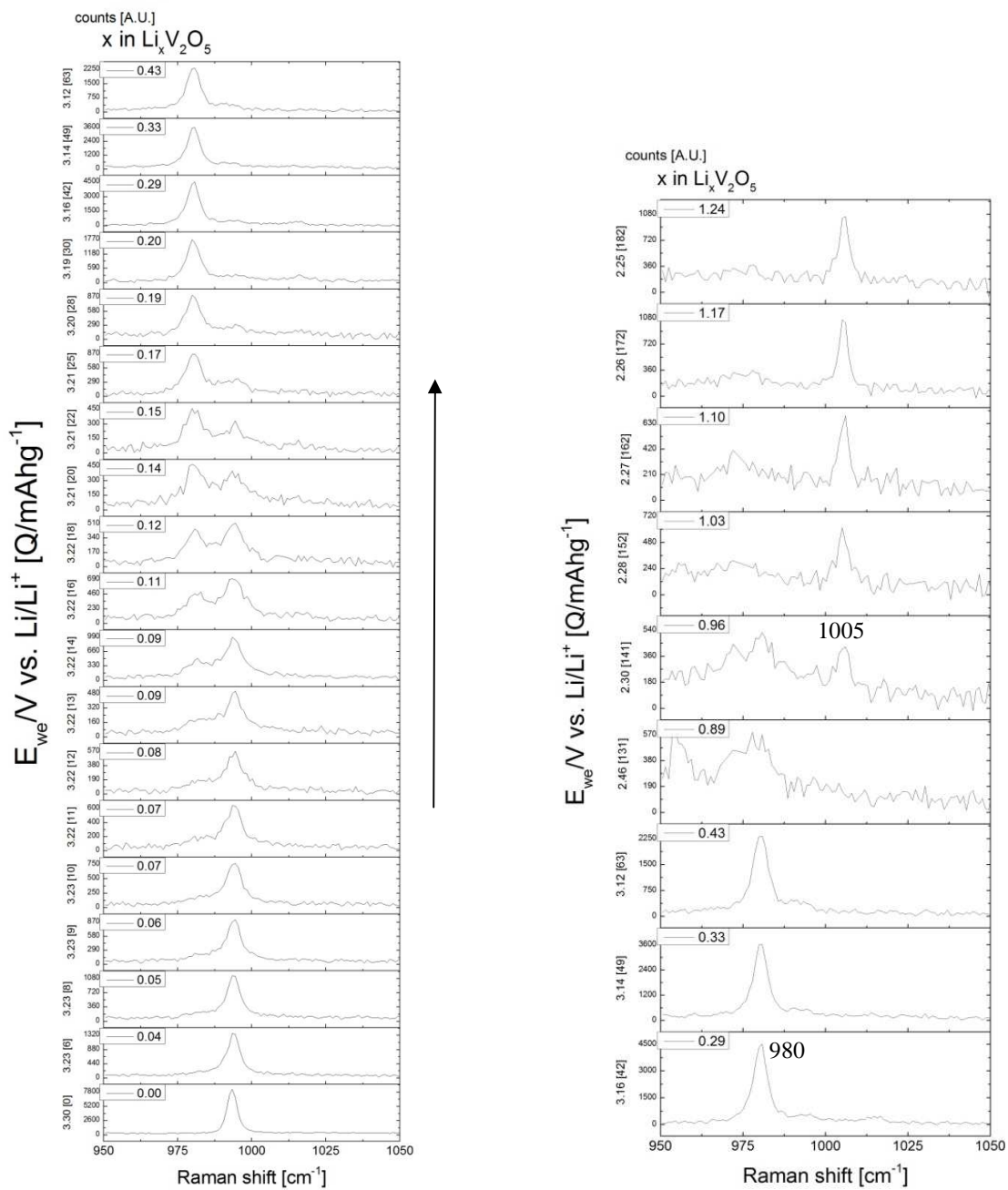


Figure 91: *In situ* Raman spectrum, lithium intercalation into V_2O_5 commercial powder electrode (separator preparation technique), laser power: 0.5 – 1 %, exposure time: 10 s – 300 s, C-range: C/4, voltage limit: 2 V (vs. Li/Li^+), Raman shift range: 950 – 1050 cm^{-1} , left: 3.30 – 3.12 V right: 3.16 – 2.25 V

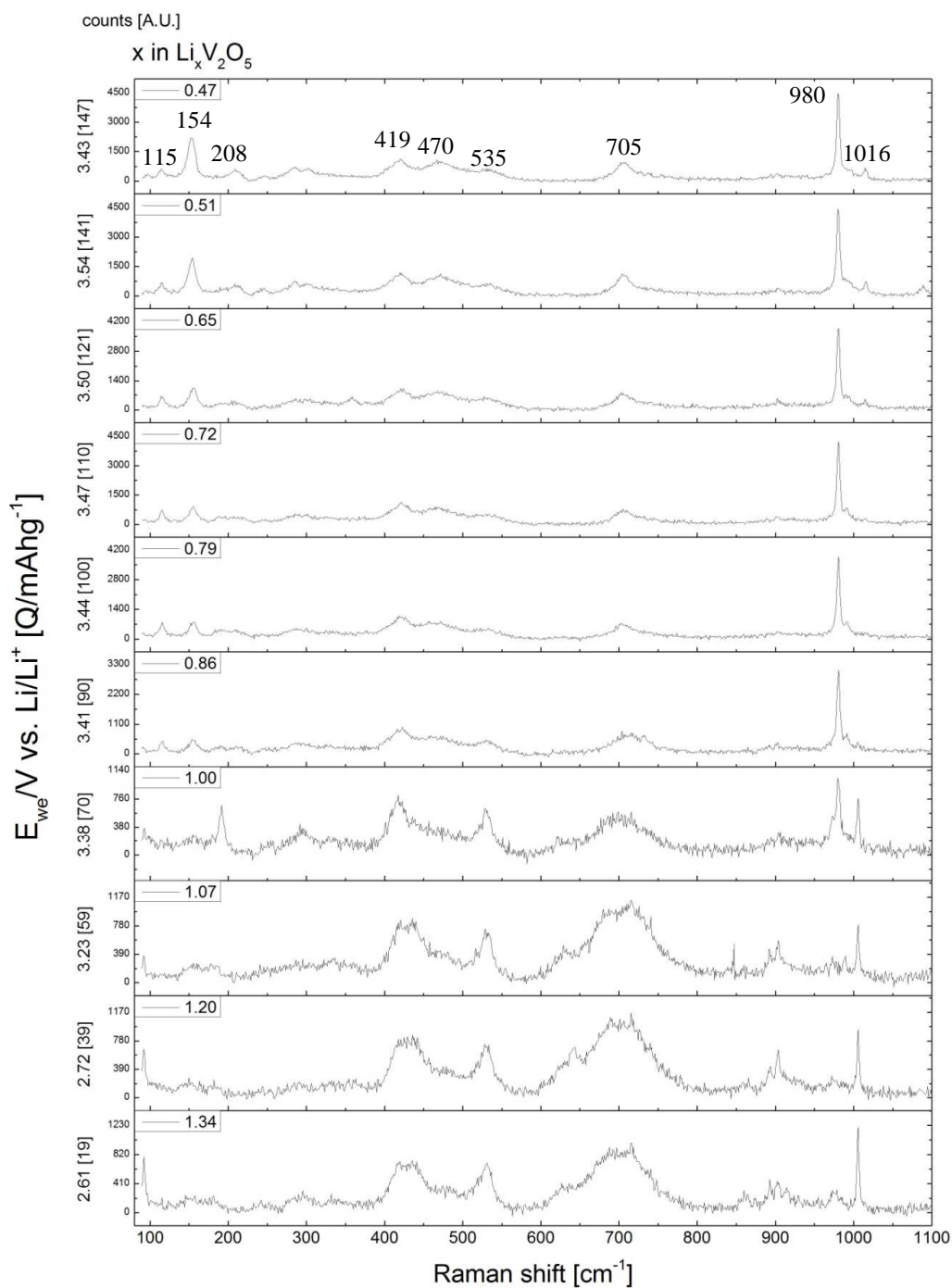


Figure 92: *In situ* Raman spectrum, lithium de-intercalation from V_2O_5 commercial powder electrode (separator preparation technique), laser power: 0.5 – 1 %, exposure time: 10 s – 300 s, Raman shift range: 90 – 1100 cm^{-1} , C-range: C/4, voltage limit: 2 V (vs. Li/Li^+)

Figure 93 - Figure 97 relate to an *in situ* Raman measurement of a V_2O_5 (commercial powder) working electrode, which was discharged down to a potential of 2.8 V and subsequently charged again up to a potential of 3.8 V. The transformation from the α to the ε phase occurred at a potential of 3.25 V and the formation of the δ phase at 3.1 V, see Figure 93. Figure 94 displays the *in situ* Raman spectra, which were taken during the intercalation process of lithium into V_2O_5 . During intercalation the significant peak split of the 994 cm^{-1} peak occurred at a potential of 3.18 V and was finished at a potential of 2.92 V, which can be related to the end of the formation of the δ phase. The peak with the highest intensity at 145 cm^{-1} again lost its intensity enormously within the first spectra, but this time it was still present at a potential of 2.92 V where the formation of the δ phase was nearly completely finished. Also most of the other α phase peaks could be identified. During charge process, see Figure 95, the significant δ phase Raman spectrum suddenly appeared at a potential of 3.34 V, but the peak at 145 cm^{-1} was still there, but lost its intensity. At a final potential of 3.80 V the characteristic α phase was nearly completely rebuild. The only big differences in the Raman spectra were the intensity distributions and that there was still a peak at Raman shift of 981 cm^{-1} next to the peak at 995 cm^{-1} . The split up of the peak could not be reformed completely. The rebuild of the α phase show the reversibility of the lithium intercalation from the δ phase.

Figure 96 and Figure 97 show *in situ* Raman measurements at two different spots. As it can be seen in Figure 96 the intercalated lithium amount varies at different spots. Spot 2 seems to be better contacted to the carbon matrix, see Figure 97 and is therefore faster with the lithium intercalation compared to spot 1. The spectra were measured during an *in situ* measurement where the spots were changed directly after one measurement. At nearly the same potential the spectra diversify enormously, which can be seen particularly at the peak split around the 1000 cm^{-1} Raman shift range. This means that it is very important to provide a good electronic contact to all active material particles to achieve the same lithium concentration anytime all over the electrode.

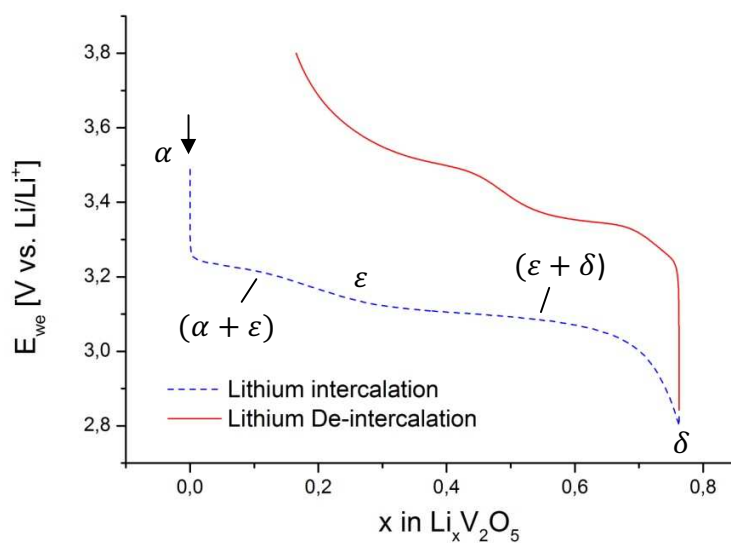


Figure 93: Galvanostatic cycling of commercial V_2O_5 powder electrode (separator preparation technique) for *in situ* Raman measurement, with lithium metal as counter electrode and DMC/EC 1:1 + 1 M LiPF_6 as electrolyte, cycled with a C-range of C/4, voltage limit: 2.8 V and 3.8 V (vs. Li/Li⁺)

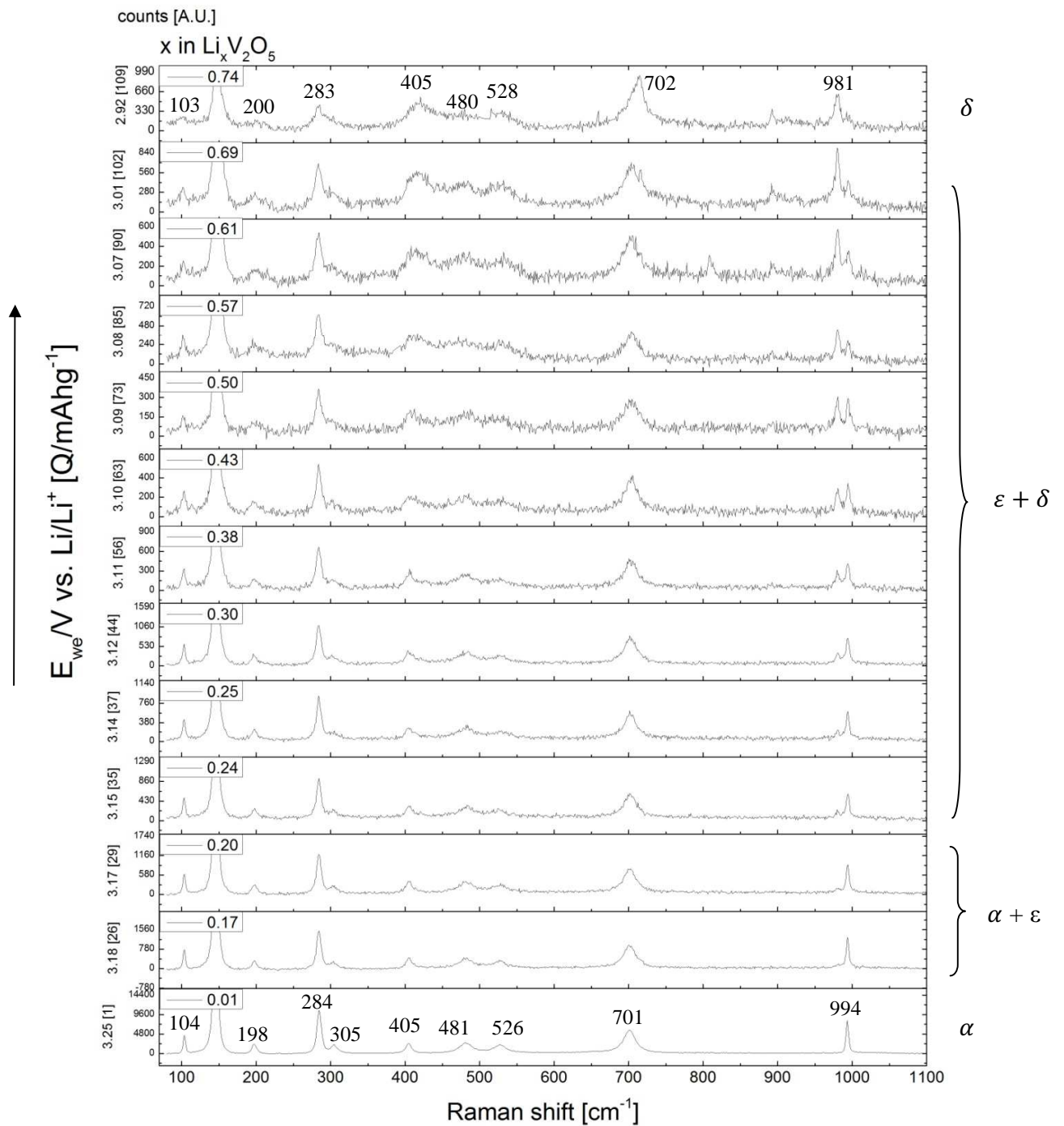


Figure 94: *In situ* Raman spectrum, lithium intercalation into V_2O_5 commercial powder electrode (separator preparation technique), laser power: 0.5 – 1 %, exposure time: 30 s – 300 s, Raman shift range: 80 – 1100 cm^{-1} , C-range: C/4, voltage limit: 2.8 V and 3.8 V (vs. Li/Li^+), y-scale zoomed in

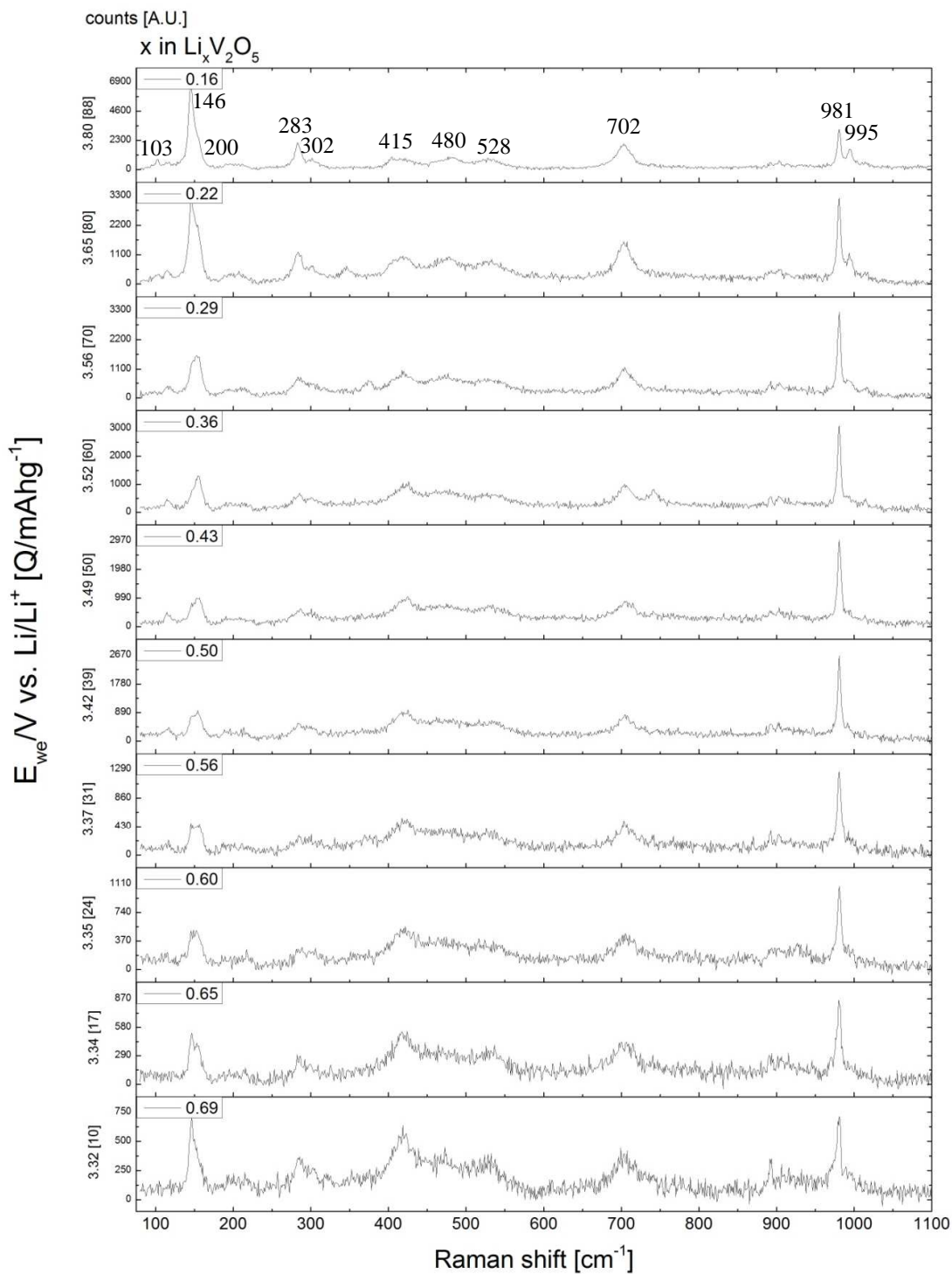


Figure 95: *In situ* Raman spectrum, lithium de-intercalation from V_2O_5 commercial powder electrode (separator preparation technique), laser power: 0.5 – 1 %, exposure time: 30 s – 300 s, Raman shift range: 80 – 1100 cm^{-1} , C-range: C/4, voltage limit: 2.8 V and 3.8 V (vs. Li/Li^+), y-scale zoomed in

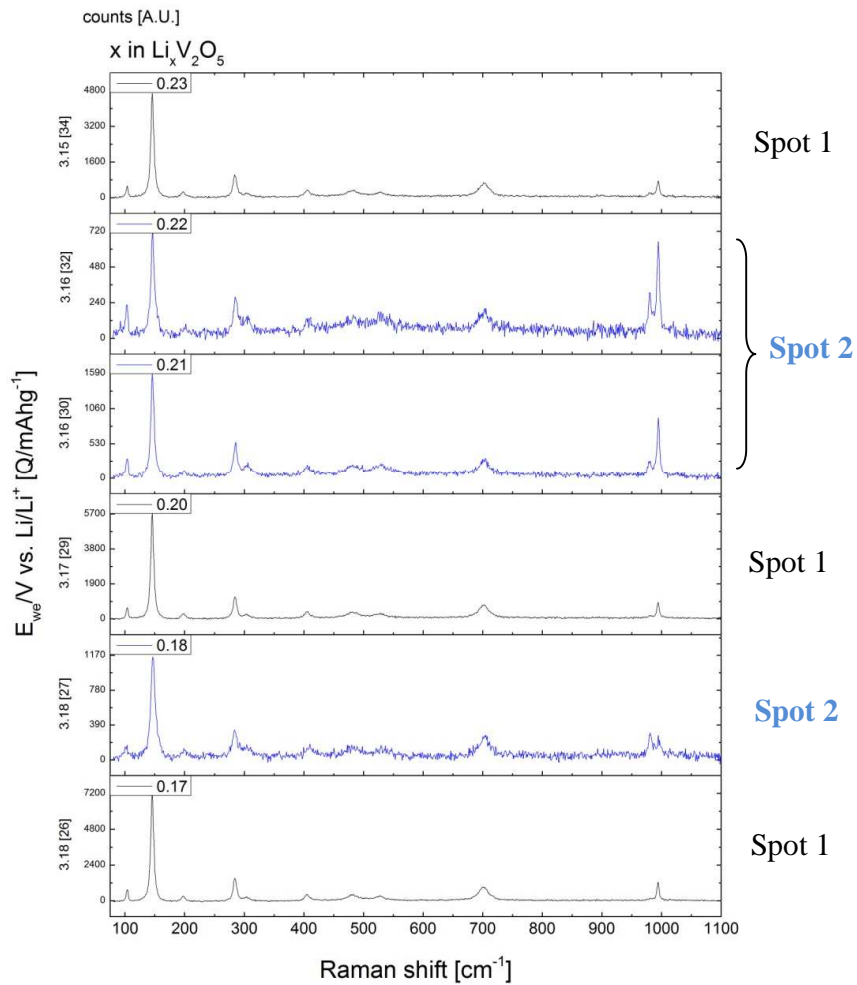


Figure 96: *In situ* Raman spectrum, lithium intercalation into V_2O_5 commercial powder electrode (separator preparation technique), laser power: 0.5 – 1 %, exposure time: 30 s – 300 s, Raman shift range: 80 – 1100 cm^{-1} , C-range: C/4, voltage limit: 2.8 V and 3.8 V (vs. Li/Li^+), comparison of two different measuring spots

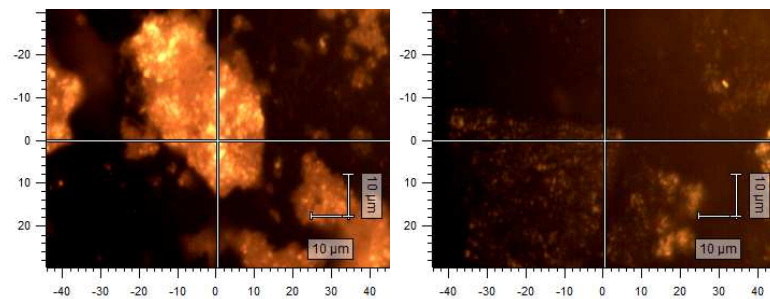


Figure 97: Microscope pictures of two different measuring spots for an *in situ* Raman measurement (lithium intercalation into V_2O_5 commercial powder electrode), left: spot 1, right: spot 2

Nanowires Electrodes

Figure 98 represents a galvanostatic cycling measurement of a working electrode made of V_2O_5 nanowires (3rd synthesis). The cell, including a lithium metal counter electrode and an electrolyte made of a solution of 1:1 EC:DMC including 1 M $LiPF_6$, was cycled down to 1.8 V (vs. Li/Li^+). The different phase formations occurred at 3.3 V for the ϵ phase, at 3.1 V for the δ phase, 2.2 V for the γ phase and 1.9 V for the ω phase. Compared to the electrodes, which were made of the commercial V_2O_5 powder, there exists no significant difference.

In Figure 99 is shown the corresponding *in situ* Raman measurement, which was measured during lithium intercalation (discharge) of the battery. The α phase is characterised by 10 peaks, which occurred at a Raman shift of 103 cm^{-1} , 145 cm^{-1} , 197 cm^{-1} , 284 cm^{-1} , 305 cm^{-1} , 404 cm^{-1} , 480 cm^{-1} , 525 cm^{-1} , 700 cm^{-1} and 993 cm^{-1} . The significant peak split of the 993 cm^{-1} peak started at a potential of about 3.24 V and ended at 3.12 V, which can be related to the end of the δ phase formation. The δ phase consisted of five peaks at a Raman shift of 170 cm^{-1} , 300 cm^{-1} , 420 cm^{-1} , 528 cm^{-1} and 715 cm^{-1} .

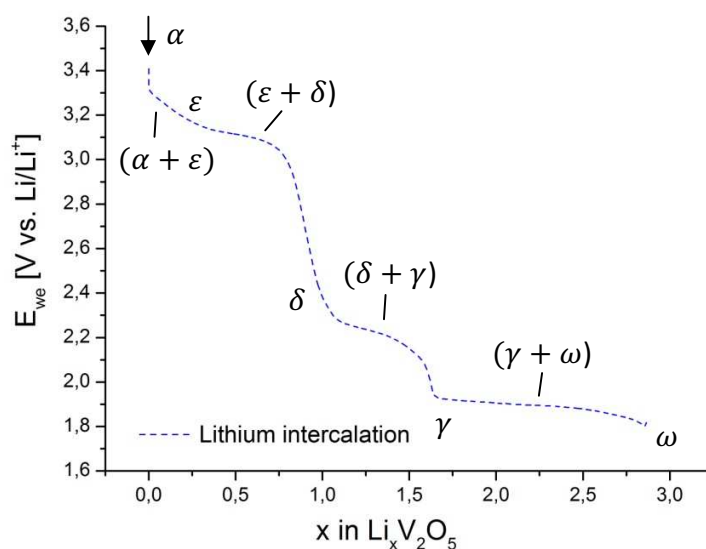


Figure 98: Galvanostatic cycling of V_2O_5 nanowires electrode (separator preparation technique) for *in situ* Raman measurement, with lithium metal as counter electrode and DMC/EC 1:1 + 1 M $LiPF_6$ as electrolyte, cycled with a C-range of C/4, voltage limit: 1.8 V (vs. Li/Li^+)

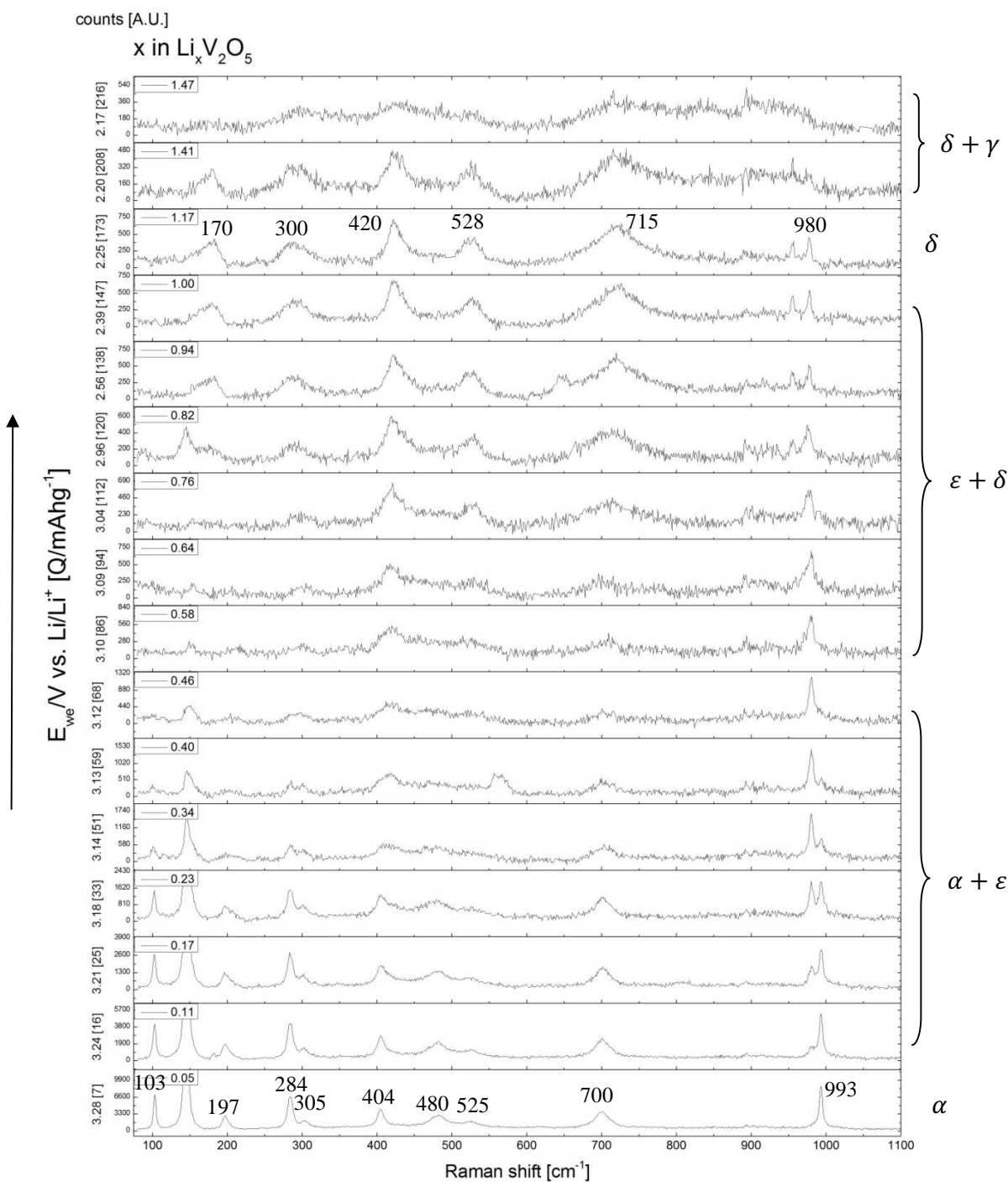


Figure 99: *In situ* Raman spectrum, lithium intercalation into V_2O_5 nanowires electrode (separator preparation technique), laser power: 1 %, exposure time: 60 s – 180 s, Raman shift range: 80 – 1100 cm^{-1} , C-range: C/4, voltage limit: 1.8 V (vs. Li/Li^+), y-scale zoomed in

In Figure 100 is shown a galvanostatic cycling measurement of a working electrode made of V_2O_5 nanowires (3rd synthesis) for an *in situ* Raman measurement. The working electrode was made by the separator preparation technique and the cell was cycled down to 2.0 V (vs. Li/Li^+) with a C-rate of C/4. The α to ε phase transformation started at a potential of about 3.3 V, the δ formation 3.1 V and the γ formation at 2.25 V. In Figure 101 are displayed the *in situ* Raman spectra, which were taken during lithium intercalation. The significant peak split during the α to ε and ε to δ phase transformation started at a potential of 3.26 V and ended at 3.07 V. The other peaks lost their intensity and got broader. The δ phase exhibited six peaks at a Raman shift of 170 cm^{-1} , 300 cm^{-1} , 420 cm^{-1} , 530 cm^{-1} , 710 cm^{-1} and 980 cm^{-1} . From the beginning of the γ phase formation there were no significant peaks observed anymore.

In Figure 102 is shown the *in situ* Raman measurement of the subsequent charge (delithiation) and second discharge (lithiation) of the battery. At the highest charge potential of about 3.8 V the Raman spectrum consisted of two significant peaks at 145 cm^{-1} and 980 cm^{-1} . It did not resemble the α phase, but the interesting thing is, that after subsequently second discharge of the battery the Raman spectrum got first back to the appearance of the α phase at a potential of 3.27 V with one 994 cm^{-1} peak and a high 145 cm^{-1} peak. After that it changed back to the typical discharge behavior. Probably the cell was cycled too fast and the active material particle, at which was measured, did not have enough time to reach equilibrium. The occurrence of the α phase after the charge process shows, that the formation of the γ back to the α phase is possible and therefore is reversible with V_2O_5 nanowires in contrast to the commercial V_2O_5 powder, where no α phase could be measured anymore after discharging down to a potential of about 2 V.

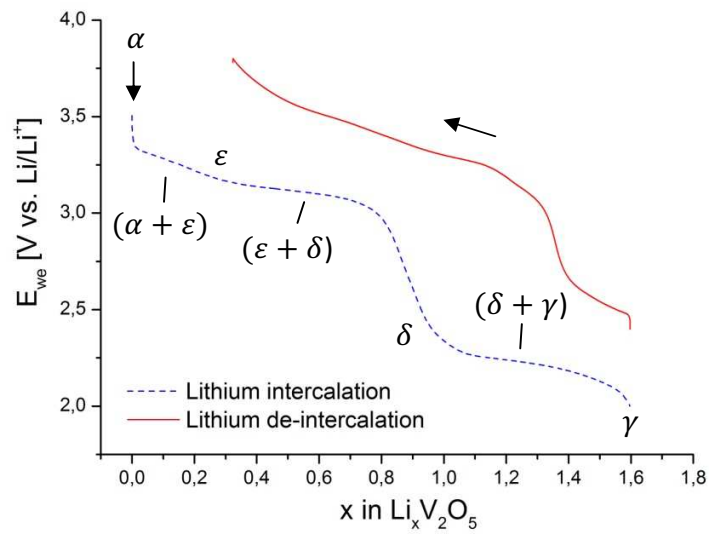


Figure 100: Galvanostatic cycling of V_2O_5 nanowires electrode (separator preparation technique) for *in situ* Raman measurement, with lithium metal as counter electrode and DMC/EC 1:1 + 1 M $LiPF_6$ as electrolyte, cycled with a C-range of C/4, voltage limit: 2 V (vs. Li/Li⁺)

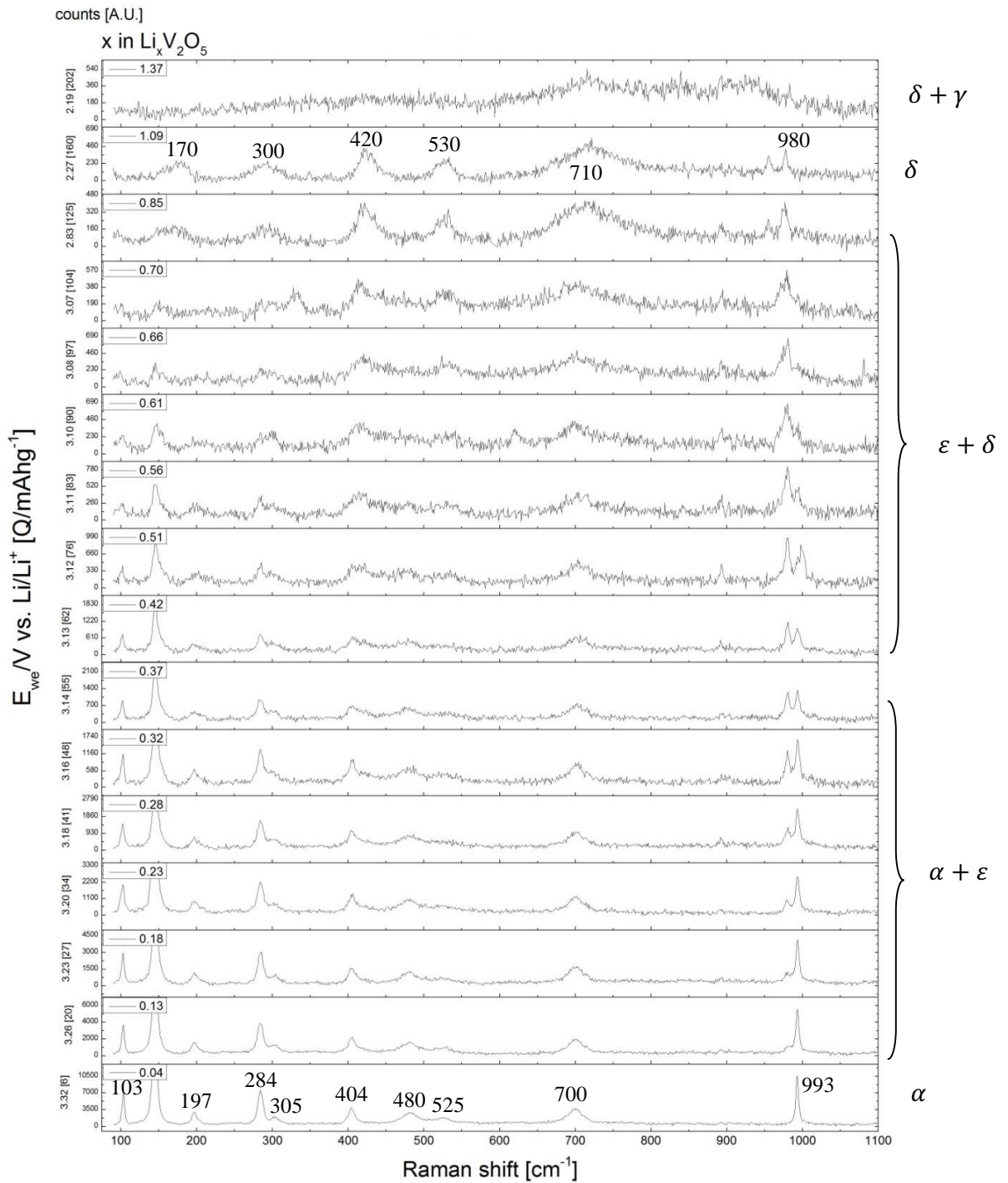


Figure 101: *In situ* Raman spectrum, lithium intercalation into V_2O_5 nanowires electrode (separator preparation technique), laser power: 1 %, exposure time: 180 s, Raman shift range: 90 – 1100 cm^{-1} , C-range: C/4, voltage limit: 2.0 V (vs. Li/Li^+), y-scale zoomed in

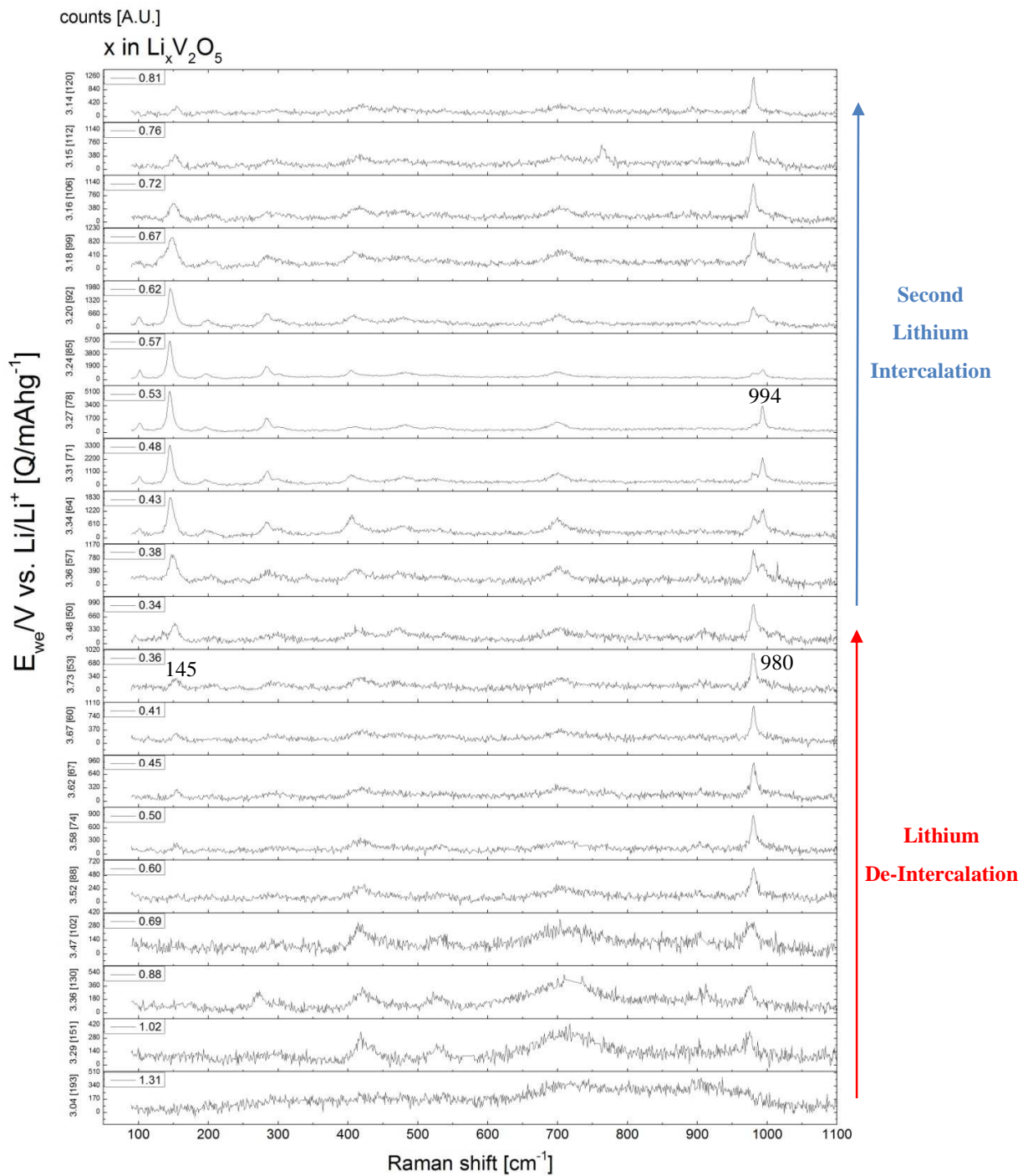


Figure 102: *In situ* Raman spectrum, lithium de-intercalation from and second lithium intercalation into V_2O_5 nanowires electrode (separator preparation technique), laser power: 1 %, exposure time: 180 s, Raman shift range: 90 – 1100 cm^{-1} , C-range: C/4, voltage limit: 2.0 V (vs. Li/Li^+), y-scale zoomed in

Figure 103 displays a galvanostatic cycling measurement of a working electrode made of V_2O_5 nanowires, which was cycled down to a potential of 2.8 V and back up to 3.8 V (vs. Li/Li^+) with $C/4$. In both charge and discharge curves can be seen the two significant flat voltage plateaus, which characterise the phase transformations of the α to ϵ phase started at a potential of 3.32 V and the ϵ to δ phase transformation, which started at a potential of about 3.15 V. The phase transformations during the charge process occurred at slightly lower potentials of about 3.1 V and 3.25 V.

The corresponding *in situ* Raman measurement during lithiation is shown in Figure 104. The intensity loss of the Raman signal within the first spectra, especially of the 145 cm^{-1} peak, can be seen in Figure 106. The peak at 993 cm^{-1} started to split up at 3.25 V during the ϵ formation and brought a peak at 980 cm^{-1} about. At the end of the δ phase transformation the peak at 993 cm^{-1} completely disappeared and only the 980 cm^{-1} peak remained. The Raman spectrum of the δ phase consisted of five peaks at a Raman shift of about 293 cm^{-1} , 422 cm^{-1} , 525 cm^{-1} , 708 cm^{-1} and 980 cm^{-1} .

During de-intercalation of lithium, see Figure 105, the peak at 993 cm^{-1} and also the peak at 145 cm^{-1} appeared again. All in all the spectrum resembles the spectrum of the α phase and therefore it can be said, that the phase transformation to the δ phase is reversible.

In comparison to the commercial V_2O_5 powder there could not be observed any peak at a Raman shift of 1005 cm^{-1} within the δ phase formation.

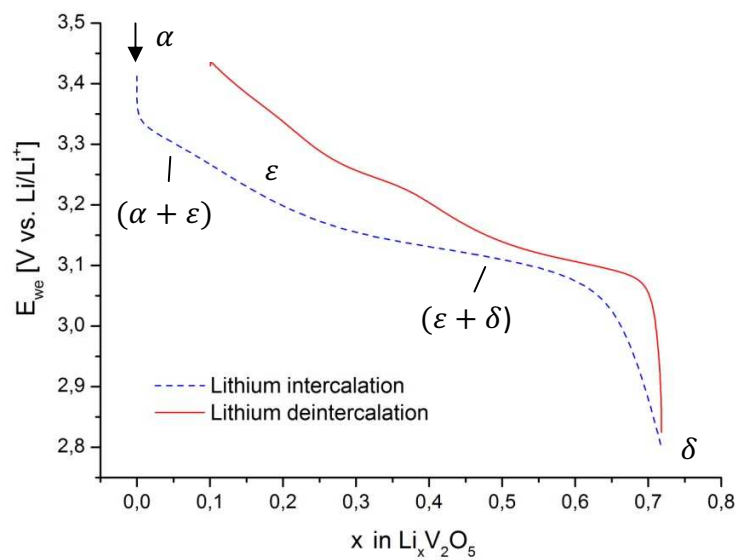


Figure 103: Galvanostatic cycling of V_2O_5 nanowires electrode (separator preparation technique) for *in situ* Raman measurement, with lithium metal as counter electrode and DMC/EC 1:1 + 1 M LiPF_6 as electrolyte, cycled with a C-range of C/4, voltage limit: 2.8 V and 3.6 V (vs. Li/Li⁺)

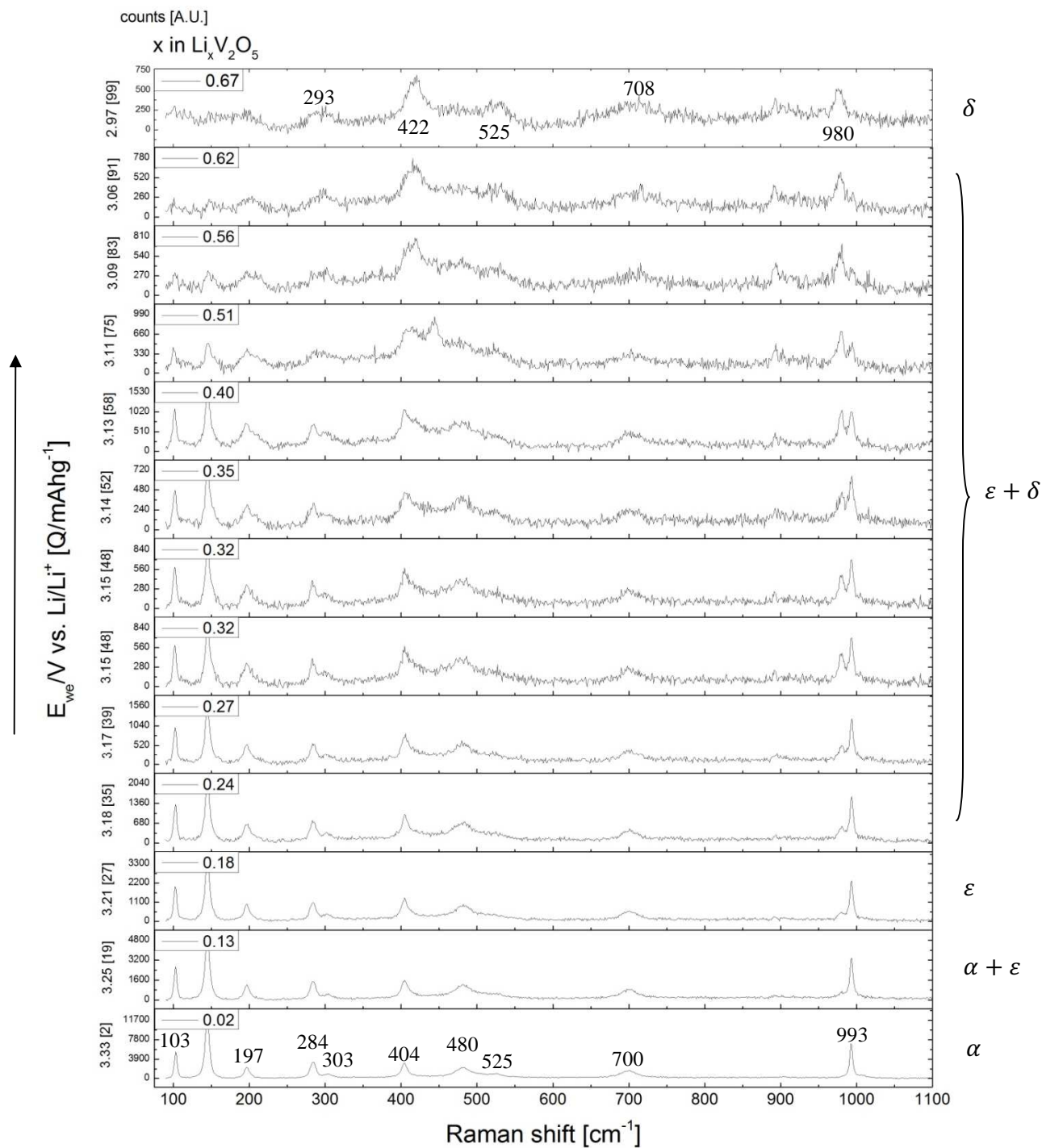


Figure 104: *In situ* Raman spectrum, lithium intercalation into V_2O_5 nanowires electrode (separator preparation technique), laser power: 1 %, exposure time: 60 - 180 s, Raman shift range: 90 – 1100 cm^{-1} , C-rate: C/4, voltage limit: 2.8 V (vs. Li/Li^+), y-scale zoomed in

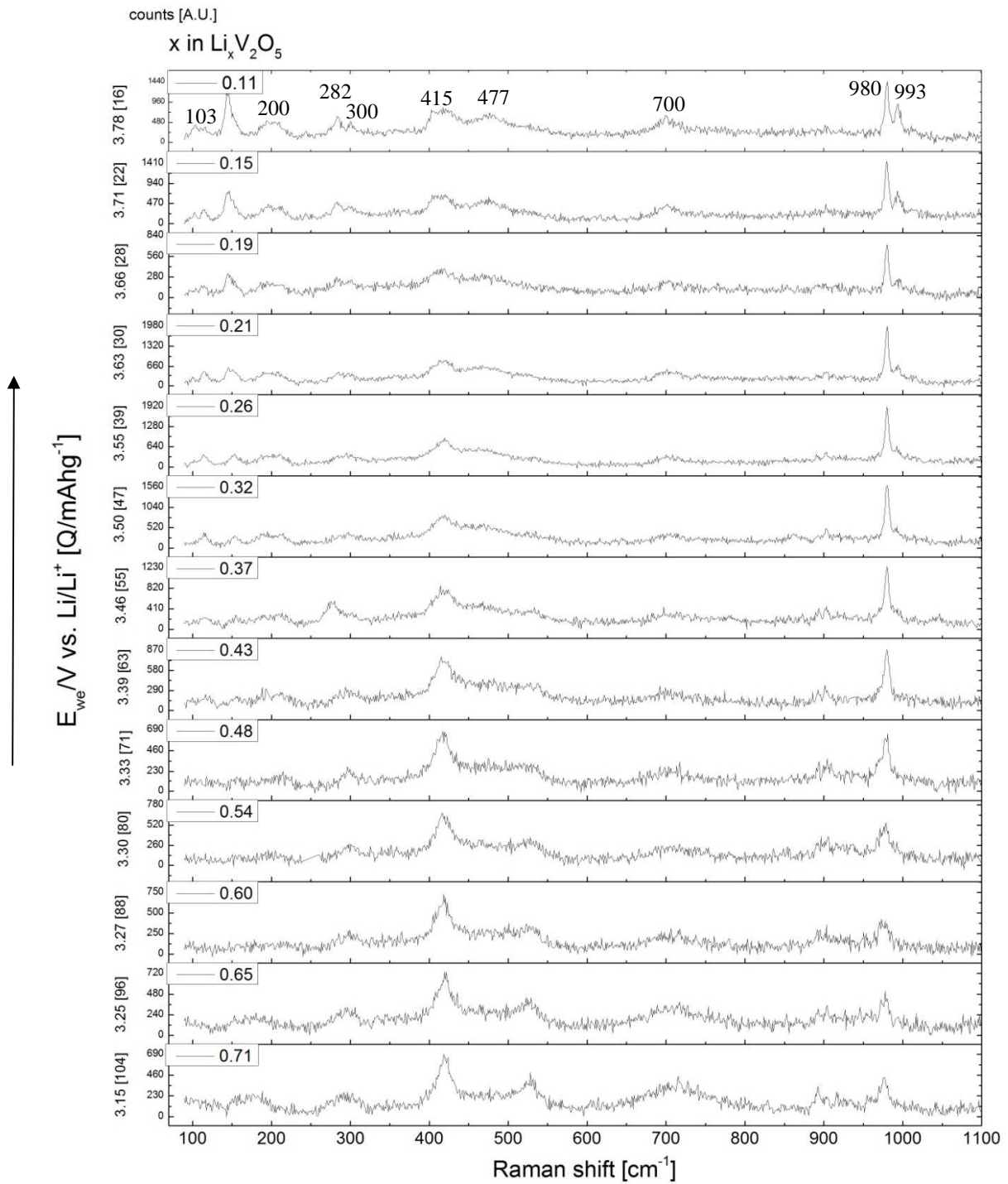


Figure 105: *In situ* Raman spectrum, lithium de-intercalation from V_2O_5 nanowires electrode (separator preparation technique), laser power: 1 %, exposure time: 60 - 180 s, Raman shift range: 90 – 1100 cm^{-1} , C-range: C/4, voltage limit: 3.8 V (vs. Li/Li^+), y-scale zoomed in

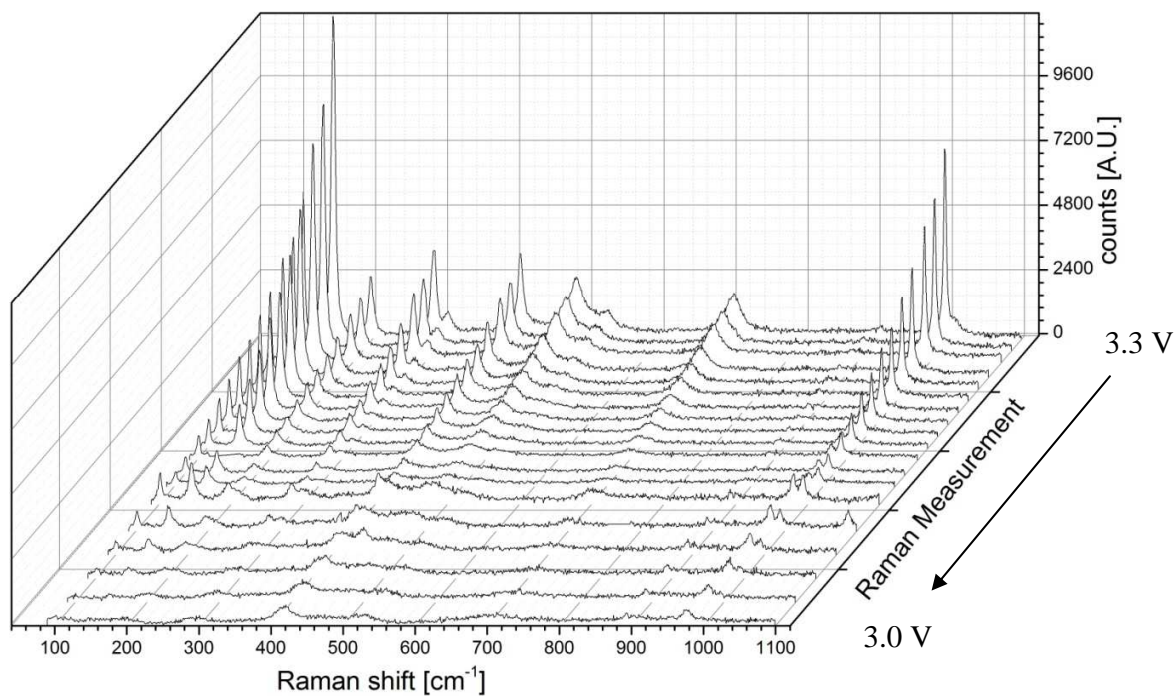


Figure 106: *In situ* Raman spectrum, lithium intercalation into V₂O₅ nanowires electrode (separator preparation technique), laser power: 1 %, exposure time: 60 - 180 s, Raman shift range: 90 – 1100 cm⁻¹, C-range: C/4, voltage limit: 2.8 V (vs. Li/Li⁺), waterfall stacked, showing the loss of intensity within the first discharge measurement from 3.3 V to 3.0 V

5 Conclusions

The non aqueous aluminium battery with the ionic liquid [(EMIm)Cl] including AlCl_3 as electrolyte as well as the aqueous aluminium battery with an aqueous AlCl_3 solution as electrolyte and a TiO_2 working electrode showed challenges, due to destructive corrosion processes, which could not be overcome within the short time of this project. Efforts of changing the current collectors and the active materials unfortunately did not lead to success. Solid state NMR measurements of the cycled V_2O_5 nanowires working electrode within a non aqueous aluminium battery were undertaken. Their results were difficult to interpret and did not bring significant information about the aluminium intercalation.

In situ Raman measurements were successfully undertaken of lithium batteries including Graphite, TiO_2 and V_2O_5 as working electrodes. Either the commercial V_2O_5 powder as well as the self-made V_2O_5 nanowires, which were produced via a hydrothermal method and characterised by XRD and SEM pictures, showed well electrochemical behaviour. *In situ* Raman spectra of $\text{Li}_4\text{Ti}_5\text{O}_{12}$ did not show any peak changes within lithiation or delithiation although the electrochemistry worked properly.

With the help of a special designed two electrodes *in situ* Raman cell and a new established electrode preparation technique were taken a lot of spectra during the lithium intercalation as well as the de-intercalation of lithium with a good signal to noise ratio. It was possible to distinguish between the different V_2O_5 phases and to observe the shifting of the peaks. The significant peak split at a Raman shift of about 993 cm^{-1} could be clearly observed.

The spectra of the V_2O_5 nanowires favour the spectra of thin film V_2O_5 layers, produced by atomic layer deposition (ALD) [62], rather than the bulk V_2O_5 , showing that the nanoscale has an effect on the course of lithium insertion into V_2O_5 .

6 Further Work

In situ Raman measurements are a powerful tool to investigate the relationship between the structure and electrochemistry of electrode processes. A significant improvement of Raman spectroscopy and a wider application of this technique will be gained by systematically combination of an experimental approach with appropriate lattice dynamic simulations. This includes the development of reliable theoretical analysis and a relevant interpretation of the measures Raman bands. [61]

To improve the aluminium ion battery it is necessary to investigate a new system in the best case including an aqueous electrolyte, which is less aggressive to metals and hence to the current collectors. This would cause less corrosion processes and therefore a functional battery could hopefully be developed.

7 References

1. Owen, J.R., *Rechargeable lithium batteries*. Chemical Society Reviews, 1997. 26(4): p. 259-267.
2. *Key World Energy Statistics 2012*. 2012 [cited 2012 02.10.]; Available from: <http://www.iea.org/publications/freepublications/publication/name,31287,en.html>.
3. Scrosati, B. and J. Garche, *Lithium batteries: Status, prospects and future*. Journal of Power Sources, 2010. 195(9): p. 2419-2430.
4. Tammilehto, O. and O. Tammilehto, *On the Prospect of Preventing Global Climate Catastrophe due to Rapid Social Change*. Capitalism Nature Socialism, 2012. 23(1): p. 79-92.
5. Liu, C., et al., *Advanced Materials for Energy Storage*. Advanced Materials, 2010. 22(8): p. E28.
6. Woynillowicz, D., *Tar Sands Fever*, in *World Watch Magazine* 2007, Worldwatch Institute: Washington, DC 20036.
7. Goodenough, J.B., et al., *Challenges for Rechargeable Li Batteries*. Chemistry of Materials, 2010. 22(3): p. 587-603.
8. Winter, M., et al., *What Are Batteries, Fuel Cells, and Supercapacitors?* Chemical Reviews, 2004. 104(10): p. 4245-4269.
9. Tarascon, J.M. and M. Armand, *Issues and challenges facing rechargeable lithium batteries*. Nature, 2001. 414(6861): p. 359-367.
10. Mikolajczak, C., et al., *Lithium-Ion Batteries Hazard and Use Assessment* 2012: Springer.
11. Cheng, F., et al., *Functional materials for rechargeable batteries*. Advanced Materials, 2011. 23(15): p. 1695-1715.
12. Dell, R., D.A.J. Rand, and R.S.o. Chemistry, *Understanding Batteries* 2001: Royal Society of Chemistry.
13. Winter, M., et al., *Insertion electrode materials for rechargeable lithium batteries*. Advanced Materials, 1998. 10(10): p. 725-763.
14. Bard, A.J., G. Inzelt, and F. Scholz, *Electrochemical Dictionary* 2012: Springer.
15. Crompton, T.P.J., *Battery Reference Book* 2000: Elsevier Science.
16. Engel, T. and P.J. Reid, *Physikalische Chemie* 2006: Pearson Studium.
17. Pletcher, D., *A First Course in Electroge Processes* 2009: ROYAL SOC OF CHEMISTRY.
18. Fafilek, G., *164.197 Technische Elektrochemie II - TU Wien*, 2011.
19. Scrosati, B., J. Hassoun, and Y.K. Sun, *Lithium-ion batteries. A look into the future*. Energy and Environmental Science, 2011. 4(9): p. 3287-3295.
20. Liu, S., et al., *Aluminum storage behavior of anatase TiO₂ nanotube arrays in aqueous solution for aluminum ion batteries*. Energy & Environmental Science, 2012.
21. Etacheri, V., et al., *Challenges in the development of advanced Li-ion batteries: A review*. Energy and Environmental Science, 2011. 4(9): p. 3243-3262.

22. Di Pietro, B., M. Patriarca, and B. Scrosati, *On the use of rocking chair configurations for cyclable lithium organic electrolyte batteries*. *Journal of Power Sources*, 1982. 8(2): p. 289-299.
23. Yoshio, M., R.J. Brodd, and A. Kozawa, *Lithium-Ion Batteries: Science and Technologies* 2009: Springer.
24. Ardel, G., et al., *Rechargeable lithium/hybrid-electrolyte/pyrite battery*. *Journal of Power Sources*, 2002. 110(1): p. 152-162.
25. *Fast ion transport in solids : electrodes, and electrolytes : proceedings of the International Conference on Fast Ion Transport in Solids, Electrodes, and Electrolytes, Lake Geneva, Wisconsin, U.S.A., May 21-25, 1979*, ed. P. Vashishta, J.N. Mundy, and G.K. Shenoy 1979, North Holland: New York.
26. Kelly, I.E., J.R. Owen, and B.C.H. Steele, *Poly(ethylene oxide) electrolytes for operation at near room temperature*. *Journal of Power Sources*, 1985. 14(1-3): p. 13-21.
27. Tarascon, J.M., et al., *Performance of Bellcore's plastic rechargeable Li-ion batteries*. *Solid State Ionics*, 1996. 86-88, Part 1(0): p. 49-54.
28. Huggins, R.A., *Advanced Batteries: Materials Science Aspects* 2009: Springer London, Limited.
29. Linden, D. and T.B. Reddy, *Handbook of batteries* 2002: McGraw-Hill.
30. Xu, K., *Nonaqueous liquid electrolytes for lithium-based rechargeable batteries*. *Chemical Reviews*, 2004. 104(10): p. 4303-4417.
31. Rogers, R.D., K.R. Seddon, and S. Volkov, *Green Industrial Applications of Ionic Liquids* 2003: Springer.
32. Stassen, I. and G. Hambitzer, *Metallic lithium batteries for high power applications*. *Journal of Power Sources*, 2002. 105(2): p. 145-150.
33. Zinck, L., et al., *Purification process for an inorganic rechargeable lithium battery and new safety concepts*. *Journal of Applied Electrochemistry*, 2006. 36(11): p. 1291-1295.
34. Dünger, H.J., G. Hambitzer, and W. Lutter, *Lithium-cycling efficiency in inorganic electrolyte solution*. *Journal of Power Sources*, 1993. 44(1-3): p. 405-408.
35. Kim, G.T., et al., *Development of ionic liquid-based lithium battery prototypes*. *Journal of Power Sources*, 2012. 199: p. 239-246.
36. Balducci, A., et al., *Development of safe, green and high performance ionic liquids-based batteries (ILLIBATT project)*. *Journal of Power Sources*, 2011. 196(22): p. 9719-9730.
37. SEEO. *DryLyte™ Battery Advantages*. 2012 15.04.2013]; Available from: <http://seeo.com/drylyte-battery-advantages>.
38. Jónsson, E., M. Armand, and P. Johansson, *Novel pseudo-delocalized anions for lithium battery electrolytes*. *Physical Chemistry Chemical Physics*, 2012. 14(17): p. 6021-6025.
39. Besenhard, J.O., et al., *Filming mechanism of lithium-carbon anodes in organic and inorganic electrolytes*. *Journal of Power Sources*, 1995. 54(2): p. 228-231.

40. Yi, T.-F., et al., *Recent development and application of Li₄Ti₅O₁₂ as anode material of lithium ion battery*. Journal of Physics and Chemistry of Solids, 2010. 71(9): p. 1236-1242.
41. Ohzuku, T., A. Ueda, and N. Yamamoto, *Zero-strain insertion material of Li[Li^{1/3}Ti^{5/3}]O₄ for rechargeable lithium cells*. Journal of the Electrochemical Society, 1995. 142(5): p. 1431-1435.
42. Yi, T.F., et al., *Structural and thermodynamic stability of Li₄Ti₅O₁₂ anode material for lithium-ion battery*. Journal of Power Sources, 2013. 222: p. 448-454.
43. Ouyang, C.Y., Z.Y. Zhong, and M.S. Lei, *Ab initio studies of structural and electronic properties of Li₄Ti₅O₁₂ spinel*. Electrochemistry Communications, 2007. 9(5): p. 1107-1112.
44. Park, K.-S., et al., *Nitridation-Driven Conductive Li₄Ti₅O₁₂ for Lithium Ion Batteries*. Journal of the American Chemical Society, 2008. 130(45): p. 14930-14931.
45. Li, J., et al., *Microwave solid-state synthesis of spinel Li₄Ti₅O₁₂ nanocrystallites as anode material for lithium-ion batteries*. Solid State Ionics, 2007. 178(29–30): p. 1590-1594.
46. Yin, S.Y., et al., *Synthesis of spinel Li₄Ti₅O₁₂ anode material by a modified rheological phase reaction*. Electrochimica Acta, 2009. 54(24): p. 5629-5633.
47. Yuan, T., et al., *Cellulose-assisted combustion synthesis of Li₄Ti₅O₁₂ adopting anatase TiO₂ solid as raw material with high electrochemical performance*. Journal of Alloys and Compounds, 2009. 477(1–2): p. 665-672.
48. Bai, Y., et al., *Influence of composite LiCl–KCl molten salt on microstructure and electrochemical performance of spinel Li₄Ti₅O₁₂*. Electrochimica Acta, 2008. 54(2): p. 322-327.
49. Huang, S., et al., *Preparation and electrochemical performance of Ag doped Li₄Ti₅O₁₂*. Electrochemistry Communications, 2004. 6(11): p. 1093-1097.
50. Sun, Y.K., et al., *Synthesis and electrochemical characterization of spinel Li[Li_{(1-x)/3}Cr_xTi_{(5-2x)/3}]O₄ anode materials*. Journal of Power Sources, 2004. 125(2): p. 242-245.
51. Reale, P., et al., *Iron-substituted lithium titanium spinels: Structural and electrochemical characterization*. Chemistry of Materials, 2003. 15(18): p. 3437-3442.
52. Kubiak, P., et al., *Phase transition in the spinel Li₄Ti₅O₁₂ induced by lithium insertion - Influence of the substitutions Ti/V, Ti/Mn, Ti/Fe*. Journal of Power Sources, 2003. 119-121: p. 626-630.
53. Chen, C.H., et al., *Studies of Mg-Substituted Li_{4-x}Mg_xTi₅O₁₂ Spinel Electrodes (0 < x < 1) for Lithium Batteries*. Journal of the Electrochemical Society, 2001. 148(1): p. A102-A104.
54. Huang, S., et al., *Effects of dopant on the electrochemical performance of Li₄Ti₅O₁₂ as electrode material for lithium ion batteries*. Journal of Power Sources, 2007. 165(1): p. 408-412.
55. Huang, S., et al., *The high-rate performance of the newly designed Li₄Ti₅O₁₂/Cu composite anode for lithium ion batteries*. Journal of Alloys and Compounds, 2008. 457(1–2): p. 400-403.

56. Wang, J., et al., *Li₄Ti₅O₁₂-TiO₂ composite anode material for lithium-ion batteries*. *Journal of Power Sources*, 2013. 222(0): p. 196-201.
57. Croy, J.R., et al., *Examining hysteresis in composite x Li₂MnO₃·(1-x)LiMO₂ cathode structures*. *Journal of Physical Chemistry C*, 2013. 117(13): p. 6525-6536.
58. Arunkumar, T.A., Y. Wu, and A. Manthiram, *Factors influencing the irreversible oxygen loss and reversible capacity in layered Li[Li_{1/3}Mn_{2/3}]O₂-Li[M]O₂ (M = Mn_{0.5-y}Ni_{0.5-y}Co_{2y} and Ni_{1-y}CO_y) solid solutions*. *Chemistry of Materials*, 2007. 19(12): p. 3067-3073.
59. Thackeray, M.M., et al., *Li₂MnO₃-stabilized LiMO₂ (M = Mn, Ni, Co) electrodes for lithium-ion batteries*. *Journal of Materials Chemistry*, 2007. 17(30): p. 3112-3125.
60. Lanz, P., et al., *Oxygen release from high-energy x Li₂MnO₃·(1-x)LiMO₂ (M=Mn, Ni, Co): Electrochemical, differential electrochemical mass spectrometric, in situ pressure, and in situ temperature characterization*. *Electrochimica Acta*, 2013. 93(0): p. 114-119.
61. Baddour-Hadjean, R. and J.P. Pereira-Ramos, *Raman microspectrometry applied to the study of electrode materials for lithium batteries*. *Chemical Reviews*, 2010. 110(3): p. 1278-1319.
62. Baddour-Hadjean, R., et al., *A Raman study of the lithium insertion process in vanadium pentoxide thin films deposited by atomic layer deposition*. *Journal of Raman Spectroscopy*, 2002. 33(8): p. 631-638.
63. Striebel, K.A., et al., *Lithium and Lithium-Ion Batteries: Proceedings of the International Symposium 2004*: Electrochemical Society.
64. Park, J.K., *Principles and Applications of Lithium Secondary Batteries 2012*: Wiley.
65. Peng, C., et al., *Investigation of the anodic behavior of Al current collector in room temperature ionic liquid electrolytes*. *Electrochimica Acta*, 2008. 53(14): p. 4764-4772.
66. Suresh, P., et al., *Electrochemical behaviour of aluminium in non-aqueous electrolytes over a wide potential range*. *Journal of Power Sources*, 2002. 110(1): p. 11-18.
67. Jayaprakash, N., S.K. Das, and L.A. Archer, *The rechargeable aluminum-ion battery*. *Chemical Communications*, 2011. 47(47): p. 12610-12612.
68. Scholz, F. and A.A.M. Bond, *Electroanalytical Methods: Guide to Experiments and Applications 2010*: Springer.
69. Compton, R.G. and C.E. Banks, *Understanding Voltammetry 2011*: Imperial College Press.
70. Ozawa, K., *Lithium Ion Rechargeable Batteries: Materials, Technology, and New Applications 2012*: Wiley.
71. Novák, P., et al., *Advanced in situ methods for the characterization of practical electrodes in lithium-ion batteries*. *Journal of Power Sources*, 2000. 90(1): p. 52-58.
72. Miranda, P.B. and Y.R. Shen, *Liquid interfaces: A study by sum-frequency vibrational spectroscopy*. *Journal of Physical Chemistry B*, 1999. 103(17): p. 3292-3307.

73. Baddour-Hadjean, R., C. Navone, and J.P. Pereira-Ramos, *In situ Raman microspectrometry investigation of electrochemical lithium intercalation into sputtered crystalline V2O5 thin films*. *Electrochimica Acta*, 2009. 54(26): p. 6674-6679.
74. Ferraro, J.R., *Introductory Raman Spectroscopy*2003: Elsevier Science.
75. Turrell, G. and J. Corset, *Raman Microscopy: Developments and Applications*1996: Elsevier Science.
76. Klinowski, J., *New Techniques in Solid-State NMR*2005: Springer.
77. Chan, J.C.C., *Solid State NMR*2011: Springer.
78. Bakhmutov, V.I., *Solid-State NMR in Materials Science: Principles and Applications*2012: Taylor & Francis Group.
79. Reimer, L., *Scanning Electron Microscopy: Physics of Image Formation and Microanalysis*1998: Springer.
80. Amelinckx, S., et al., *Electron Microscopy*2008: Wiley.
81. Reimer, L. and H. Kohl, *Transmission Electron Microscopy: Physics of Image Formation*2008: Springer.
82. Bubert, H. and H. Jenett, *Surface and Thin Film Analysis*2011: Wiley.
83. Spieß, L., et al., *Moderne Röntgenbeugung: Röntgendiffraktometrie Für Materialwissenschaftler, Physiker und Chemiker*2009: Vieweg Verlag, Friedr, & Sohn Verlagsgesellschaft mbH.
84. Als-Nielsen, J. and D. McMorrow, *Elements of Modern X-ray Physics*2011: Wiley.
85. Otto, M., *Analytische Chemie*2006: Wiley.
86. Giacovazzo, C., *Fundamentals of Crystallography*2002: Oxford University Press.
87. Hahn, M. *Products of ELL-CELL - Electrochemical Test Equipment*. 2013 [cited 2013 29. March]; Available from: <http://el-cell.com/products>.
88. Hardwick, L.J., et al., *An in situ Raman study of the intercalation of supercapacitor-type electrolyte into microcrystalline graphite*. *Electrochimica Acta*, 2006. 52(2): p. 675-680.
89. *etotal21*. 2013 [cited 2013 02.05.]; Available from: http://www.etotal21.com/v2/shop/prod_view.asp?prod_grp=punch&prod_id=0004.
90. MacKenzie, K.J.D. and E. Smith, *Multinuclear Solid-State Nuclear Magnetic Resonance of Inorganic Materials*2002: Elsevier Science.
91. Zhai, T., et al., *Centimeter-long v 2O 5 nanowires: From synthesis to field-emission, electrochemical, electrical transport, and photoconductive properties*. *Advanced Materials*, 2010. 22(23): p. 2547-2552.
92. Fernandez, C., P. Bodart, and J.P. Amoureux, *Determination of 51V quadrupole and chemical shift tensor orientations in V2O5 by analysis of magic-angle spinning nuclear magnetic resonance spectra*. *Solid State Nuclear Magnetic Resonance*, 1994. 3(2): p. 79-91.
93. Liu, S., et al., *Aluminum storage behavior of anatase TiO2 nanotube arrays in aqueous solution for aluminum ion batteries*. *Energy & Environmental Science*, 2012. 5(12): p. 9743-9746.

94. Flanagan, R.J., D. Perrett, and R. Whelpton, *Electrochemical Detection in Hplc: Analysis of Drugs And Poisons* 2005: ROYAL SOC OF CHEMISTRY.
95. Wen, S.J., et al., *FTIR spectroscopy of metal oxide insertion electrodes: A new diagnostic tool for analysis of capacity fading in secondary Li/LiMn₂O₄ cells.* Journal of the Electrochemical Society, 1996. 143(6): p. L136-L138.
96. Lunell, S., et al., *Li and Na diffusion in TiO₂ from quantum chemical theory versus electrochemical experiment.* Journal of the American Chemical Society, 1997. 119(31): p. 7374-7380.
97. Park, J.H., et al., *Effect of conductive additives on the structural and electrochemical properties of Li₄Ti₅O₁₂ spinel.* Bulletin of the Korean Chemical Society, 2012. 33(12): p. 4059-4062.
98. Shu, J., et al., *Design and comparison of ex situ and in situ devices for Raman characterization of lithium titanate anode material.* Ionics, 2011. 17(6): p. 503-509.
99. Zhang, Z., et al., *Cycle performance improvement of LiFePO₄ cathode with polyacrylic acid as binder.* Electrochimica Acta, 2012. 80(0): p. 440-444.
100. Constantino, C.J.L., et al., *Phase transition in poly(vinylidene fluoride) investigated with micro-Raman spectroscopy.* Applied Spectroscopy, 2005. 59(3): p. 275-279.
101. Kawashima, Y. and G. Katagiri, *Fundamentals, overtones, and combinations in the Raman spectrum of graphite.* Physical Review B, 1995. 52(14): p. 10053-10059.
102. Ferrari, A.C. and J. Robertson, *Interpretation of Raman spectra of disordered and amorphous carbon.* Physical Review B - Condensed Matter and Materials Physics, 2000. 61(20): p. 14095-14107.
103. Ohsaka, T., F. Izumi, and Y. Fujiki, *Raman spectrum of anatase, TiO₂.* Journal of Raman Spectroscopy, 1978. 7(6): p. 321-324.
104. Huang, W. and R. Frech, *In situ Raman studies of graphite surface structures during lithium electrochemical intercalation.* Journal of the Electrochemical Society, 1998. 145(3): p. 765-770.